REPORT NO. NADC-79056-60

FRACTURE MECHANICS OF DELAMINATION

-INITIATION AND GROWTH-

A.S.D. Wang and M. Slomiana

Drexel University
Philadelphia, Pa. 19104

January 1982

FINAL CONTRACT REPORT

October 1, 1979 - September 30, 1981

CONTRACT NO. N62269-79-C-0270

Prepared for

Aircraft and Crew Systems Technology Directorate

NAVAL AIR DEVELOPMENT CENTER

Warminster, Pa. 18974

DTIC
ELECTE
JUN 18 1982

S   D

B

82 06 13 013

NADC-79056-60

N O T I C E S

REPORT NUMBERING SYSTEM - The numbering of technical project reports issued by the
Naval Air Development Center is arranged for specific identification purposes. Each
number consists of the Center acronym, the calendar year in which the number was
assigned, the sequence number of the report within the specific calendar year, and
the official 2-digit correspondence code of the Command Office or the Functional
Directorate responsible for the report. For example: Report No. NADC-78015-20
indicates the fifteenth Center report for the year 1978, and prepared by the Systems
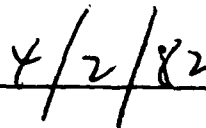Directorate. The numerical codes are as follows:

CODE	OFFICE OR DIRECTORATE
00	Commander, Naval Air Development Center
01	Technical Director, Naval Air Development Center
02	Comptroller
10	Directorate Command Projects
20	Systems Directorate
30	Sensors & Avionics Technology Directorate
40	Communication & Navigation Technology Directorate
50	Software Computer Directorate
60	Aircraft & Crew Systems Technology Directorate
70	Planning Assessment Resources
80	Engineering Support Group

PRODUCT ENDORSEMENT - The discussion or instructions concerning commercial products
herein do not constitute an endorsement by the Government nor do they convey or
imply the license or right to use such products.

APPROVED BY: _____ DATE: __4/2/82__

J. R. WOODS
CDR, USN

REPORT DOCUMENTATION PAGE		READ INSTRUCTIONS BEFORE COMPLETING FORM
1. REPORT NUMBER NADC-79056-60	2. GOVT ACCESSION NO. AD-A115 928	3. RECIPIENT'S CATALOG NUMBER
4. TITLE (and Subtitle) FRACTURE MECHANICS OF DELAMINATION -INITIATION AND GROWTH-		5. TYPE OF REPORT & PERIOD COVERED Final Contract Report Oct. 1, 1979 - Sept. 30, 1981
		6. PERFORMING ORG. REPORT NUMBER
7. AUTHOR(s) A.S.D. Wang and M. Slomiana		8. CONTRACT OR GRANT NUMBER(s) N62269-79-C-0270
9. PERFORMING ORGANIZATION NAME AND ADDRESS Drexel University Philadelphia, Pa. 19104		10. PROGRAM ELEMENT, PROJECT, TASK AREA & WORK UNIT NUMBERS
11. CONTROLLING OFFICE NAME AND ADDRESS Aircraft and Crew Systems Technology Directorate Naval Air Development Center Warminster, Pa. 18974		12. REPORT DATE January, 1982
		13. NUMBER OF PAGES 154
14. MONITORING AGENCY NAME & ADDRESS(If different from Controlling Office)		15. SECURITY CLASS. (of this report) UNCLASSIFIED
		15a. DECLASSIFICATION/DOWNGRADING SCHEDULE

16. DISTRIBUTION STATEMENT (of this Report)

Approved for Public Release: Distribution Unlimited.

17. DISTRIBUTION STATEMENT (of the abstract entered in Block 20, If different from Report)

18. SUPPLEMENTARY NOTES

19. KEY WORDS (Continue on reverse side if necessary and identify by block number)

Composite materials, graphite epoxy laminates, transverse cracking, delamination, x-radiography, fracture mechanics, strain energy release rate, finite element, initiation and growth criteria, tension, compression, fatigue, fatigue growth model, cumulative damage model.

20. ABSTRACT (Continue on reverse side if necessary and identify by block number)

This report describes the results from an experimental and analytical study on the fracture mechanics of delamination. Experiments have been conducted using the AS-3501-06 graphite-epoxy laminates in order to observe delamination growth of various geometrical and loading conditions. Static and fatigue crack growth under both tension and compressive loads are studied. The experiments helped to identify and isolate the most important loading, geometry and material parameters which influence the delamination processes. Predictive models are then developed to model these processes, based on the linear elastic fracture mechanics concept of energy release rate. The models are executed by a finite

Block 20   Continued:

element routine which simulates the crack growth process.

Extension of the energy method to the growth process under constant amplitude fatigue loads leads to the concept of constant damage states. This concept is readily applied in a cumulative damage model for fatigue under spectrum loading.

NADC-79056-60

TABLE OF CONTENTS

Page

Foreword

Foreword

LIST OF TABLES

LIST OF FIGURES

I.   INTRODUCTION

In the failure analysis of composite laminates, one of the most serious problems has been the propagation of interlaminar cracking, commonly known as delamination. This mode of failure is a major cause for the deterioration of laminate structural properties, including its strength, stiffness, reliability and durability. Although delamination occurs initially as a local damage, it can propagate rapidly to cause catastrophic laminate failure, especially under compressive and/or fatigue loads.

The exact formation and growth mechanisms of interlaminar cracking in laminates are not well understood. The general belief is that a certain distribution of small interface flaws* exists in laminates prior to loading. These are thought to be caused by factors such as poor fabrication, improper handling, residual curing stresses, external impact damage, environmental degradation, etc. Under a certain critical loading condition, some interface flaws would grow and coalesce with each other, forming a single crack of macroscopic proportion.** At this dimensional level, such an event would constitute the onset, or the initiation of the macro-crack, the delamination.

Experimental evidence indicates that upon the initiation of a delamination, the growth process may remain stationary in some laminates; while

---

*   The size of the interface flaws is of the order of the fiber diameter. For graphite-epoxy composite systems, for instance, this dimension is about $4 \sim 5$ μm.

** Observable interfacial cracks are in the realm of the ply thickness, which is two orders of magnitude larger than the size of fiber diameter in most commercially available graphite-epoxy systems.

in others the process may be unstable and lead to catastrophic growth. Clearly, the factors that influence the nature of delamination initiation and growth are complicated. The exact cracking mechanisms may ultimately involve intricate material, geometrical and loading interactions.

Early investigators focused mainly on experimental studies of free edge induced delamination in laboratory test specimens [1-6]. The emphasis was to determine the effect of laminate stacking sequence on tensile strength and fatigue life. It was found that the laminates of particular stacking sequences in which free-edge delamination occurred, always had a reduced strength.

The major cause of free edge delamination is the tensile component (normal to lamina interface) of the interlaminar stresses that concentrate near the laminate edge boundaries. The sign and magnitude of the interlaminar stresses vary considerably with the stacking sequence of the laminate.

A considerable amount of effort in the past decade has been expended to calculate analytically the free edge stresses in multilayered laminates [7-19]. While these edge stress solutions tend to explain qualitatively the observed edge effects, they are still inadequate to provide a quantitative description of the delamination failure process, including initiation and growth behavior.

Since the delamination cracking mechanism is essentially a fracture problem, a description of the cracking process requires a fracture mechanics analysis. In a recent series of papers [20-23], Wang, Crossman, et al. reported on a fracture mechanics study of the free edge delamination problem

2

in graphite-epoxy laminates under simple tension.   The analytical

approach employed is based on the classical fracture mechanics concept of

strain energy release rate [24].   A numerical (finite element) routine incor-

porating the technique of crack-closure [25] is developed to simulate the

delamination cracking process.*   The method proved to be viable in describing

the delamination process, correlating with an experimental verification effort

which was conducted concurrently by Wang, et al. [23].

The main results obtained in the Wang/Crossman study are briefly dicussed

below:

a)   One of the basic assumptions in the Wang/Crossman approach is that pre-

existing interfacial micro-flaws propagate and coalesce into a macroscopic

crack whenever a certain condition is reached due to the applied load.   In

order to bring the microscopic effect to the macroscopic level, the concept

of "equivalent edge flaw" is introduced.   Namely, the effect of the preexist-

ing micro-flaw distribution near the free edge on the initiation mechanisms

of delamination, is macroscopically equivalent to that of a single, large

crack of size a_c. a_c is thus an inherent material property of a given laminate

system.

b)   As is postulated in the classical fracture mechanics [24], it is assumed

that strain energy is released, and is converted into surface energy whenever

delamination cracking is induced by the applied load.   The rate of the avail-

able energy release per newly created cracking surface area, G, is the driving

force which extends the crack further.   Of course, the capability of the

---

* The numerical technique was first used by Rybicki and Kanninen [26] to
calculate the stress intensity factor by the crack-closure procedure.
Rybicki, et al. [27] applied the method to calculate the energy release
rate in a stable delamination cracking problem.

3

material to convert the strain energy into surface energy represents the resistance (toughness) against further crack extension. The latter is the well known critical energy release rate, denoted as G_c. The quantities G_c and a_c are the only two material parameters appearing in the predictive delamination growth model suggested by Wang and Crossman [20].

c) The behavior of the computed energy release rate, G, depends not only on the applied load, but also on the interface location of the delamination and other geometrical parameters. In particular, the amount of strain energy available for release is controlled largely by the laminate stacking sequence, the lamina geometry (thickness of lamina) and the overall laminate thickness relative to the size of the delamination. In short, G is strongly influenced by the lamination structural dimensions at the ply level.

To summarize the above development, the simple case of free edge delamination in laminates subjected to static tension has been experimentally studied and analytically simulated. The latter was based on the method of the classical fracture mechanics. Material, geometrical and loading parameters are identified explicitly in a suggested delamination growth model. It is therefore tempting to see whether or not this approach remains applicable to other types of delamination processes under different sets of material, geometrical and loading conditions. For instance, it is desirable to extend the approach to problems involving compressive and/or fatigue loading. Also, the growth behavior of an internal delamination rather than free edge delamination is another practical laminate failure problem frequently encountered in design.

Thus, it is the purpose of the present study to expand the fracture

mechanics method to describe the mechanisms of delamination in graphite-epoxy

laminates, especially under compressive static and fatigue loads. In this

effort, four categories of delamination are studied. The first problem is

the simple case of free edge delamination under static tension, case a, Fig. 1.

The selection of this problem provides a ready check of the Wang/Crossman model,

and helps to define the necessary material constants, such as G_c and a_c. The

second problem is the free edge delamination under static compressive loading.

In this case, the material and geometrical conditions remain the same as in

the first problem; only the loading direction is reversed, case b. The third

problem is the delamination emanating from an implanted interlaminar defect. The

implanted defect is a thin teflon film strip (~ 50 micron thickness) imbedded

at the intended interface of the laminate, see case c, Fig. 1. The fourth

problem is similar except that the imbedded interlaminar deflect is in a

circular shape (~ 6 mm diameter), see case d, Fig. 7.

In addition to studying the delamination mechanisms under static loading,

all four problems are also studied under constant amplitude fatigue loadings.

An understanding of the fatigue failure modes and the delamination growth

mechanisms is essential to the development of a deterministic cumulative damage

model which is necessary for the reliability analysis of laminated composites.

As far as delamination mechanisms are concerned, one of the central questions

is whether or not the mechanisms of damage are the same under static and

fatigue loadings. Recent experiments by Reifsnider, et al. [28] on damages

in laminates indicate that, given a type of laminate, there seems to exist

a damage state that is characteristic to the particular laminate, whether it be under static or fatigue loading. In addition, a certain load threshold, or a fatigue life threshold can be determined, for which the characteristic damage state occurs. These observations suggest that a law of deterministic mechanics may be found, which relates the applied load to the fatigue life for a given state of sub-laminate damage.

In view of this background, the present study also aims to use the physical parameters identified in the static delamination problems in an attempt to formulate a predictive deterministic model for delamination growth under fatigue loads.

Needless to say, such an attempt, though ambitious, is only exploratory at this stage. Gains as well as open questions encountered in this effort will be discussed in the ensuing sections.

Section II discusses the experiment and the experimental results. Whenever possible, factors influencing the mechanisms of delamination are identified and investigated in light of the experimental data.

Section III presents the analytical model and the associated numerical technique. Problems studied in the experiment are then simulated numerically. Here, the limitations of the present numerical method for treating the general types of delamination crack are discussed. Future development of more suitable methods have also been suggested in this section.

Finally, a deterministic cumulative fatigue damage model is formulated in Section IV. The model is based on the results of both analysis and experiment. A concluding discussion is given in Section V.

II. EXPERIMENT AND DISCUSSIONS

1. Description of Experiments

In this study program, the experimental plan was designed to include three major types of tests: (a) base-line laminate property tests, (b) static load-delamination growth tests; and (c) fatigue load-delamination growth tests.

The basic material system chosen for the experimental plan was the Hercules Magnamite AS-3501-06 graphite-epoxy system. The material came in prepreg form, and laminates were fabricated in accordance with NADC requirements.* All test specimens were cut using a diamond saw, and end-tabbed with fiber-glass laminates. Fig. 2 illustrates the general dimensions of the tensile specimens, while Fig. 3 shows the general dimensions of the compressive specimens. In each case, there are three types: one plain (without implanted defects) and two with implanted defects, as indicated in Fig. 2 and Fig. 3.

All tests were performed on a closed-loop Instron hydraulic testing machine. A specially designed test fixture was used for all the compression tests. Fig. 4 displays the schematics of the compression test fixture. This fixture is similar to that used in the Celanese compression test. No special fixture was required for the tension tests.

The test environment for all tests was maintained at a room temperature (25°C) and ambient humidity (~ 60% R.H.) condition. Other details of the individual tests are given in the following:

---

* All laminates were layed up at Drexel University and cured at NADC facilities.

(a) <u>Base-line Property Tests</u> - The purposes of the base-line tests were to
qualify the material system and the laminate fabrication processes, and to
determine the material constants that are necessary in the analysis models.

For purpose of determining the basic lamina properties, uniaxial stress-
strain diagrams* for the $[0_{12}]$, $[90_{12}]$, $[\pm45]_{2s}$ laminates were obtained under
tension loading, and for the $[0_{12}]$, $[\pm45]_{2s}$ under compressive loading.

Included in the basic lamina properties were also test findings of $[0_{12}]$
fiber contents and specific gravity. Specific gravity was determined by
weighing and measuring a volume of the material. Fiber content was deter-
mined from photomicrographs of the untested unidirectional material.

Static stress-strain diagrams were also obtained for the following
laminates; for static tension,

$$[0_2/90_2/45_2/-45_2]_s$$
$$[90_2/0_2/-45_2/45_2]_s$$
$$[0/90/0/90/45/-45/45/-45]_s$$
$$[90/0/90/0/-45/45/-45/45]_s$$
$$[45/-45/0/90_2]_s$$
$$[-45/45/90/0_2]_s$$

and for static compression,

$$[0_2/90_2/45_2/-45_2]_s$$
$$[90_2/0_2/-45_2/45_2]_s$$
$$[0/90/0/90/45/-45/45/-45]_s$$
$$[45/-45/0/90_2]_s$$

---

* A 90°-strain gage rosette was used to measure the longitudinal and
  transverse strains for both tension and compression tests.

In all these static tests, tension or compression, the loading was maintained at a constant cross-head displacement rate of 0.012 cm/min.

Table 1 summarizes the individual tests and the number of specimens used in each test.

(b) Static Load-Delamination Growth Tests - The purpose of this series of tests is to develop an understanding of the load-delamination growth relationship for the various laminates under both static tension and static compression loadings. In order to reliably determine the load at onset of delamination, and to document the load-growth relation, a step-loading scheme was employed. Briefly, each specimen is subjected to step-loading with small increments. After each step-load, the specimen is removed from the tester and inspected by x-radiographing for any damages that may occur during the step-load. The specimen is then reloaded for the next step-loading, x-ray inspection, and so on.

The following laminates were step-loaded in tension:

$[0_2/90_2/45_2/-45_2]_s$

$[90_2/0_2/-45_2/45_2]_s$

$[0/90/0/90/45/-45/45/-45]_s$

$[90/0/90/0/-45/45/-45/45]_s$

$[45/-45/0/90_2]_s$

$[-45/45/90/0_2]_s$

$[45/-45/0/90_2]_s$ - type A

$[45/-45/0/90_2]_s$ - type B

and the following laminates were step-loaded in compression:

9

$$[0_{12}]$$

$$[0_2/90_2/45_2/-45_2]_s$$

$$[90_2/0_2/-45_2/45_2]_s$$

$$[0_2/90_2/45_2/-45_2]_s - \text{type A}$$

$$[0_2/90_2/45_2/-45_2]_s - \text{type C}$$

$$[0/90/0/90/45/-45/45/-45]_s$$

$$[0/90/0/90/45/-45/45/-45]_s - \text{type A}$$

$$[0/90/0/90/45/-45/45/-45]_s - \text{type C}$$

$$[45/-45/0/90_2]_s$$

In the above, those laminates designated as type A have an implanted interface defect consisting of a 0.25 in. (6.35 mm) Teflon strip; type B laminates have a 0.5 in. (12.7 mm) Teflon strip, and type C laminates have a circular Teflon disk of 0.25 in. (6.35 mm) in diameter. All defects are located at the mid-plane of the laminates; see Fig. 2 and Fig. 3.

Table 2 summarizes these tests and the number of specimens used in each test.

(c) <u>Fatigue Life - Delamination Growth Tests</u> - The purpose of this series of tests is to establish the fatigue load-life-damage interrelationships of the laminates under either tension-tension or compression-compression fatigue loadings. All tests were conducted under constant amplitude load cycling with a minimum to maximum load ratio, $R = 0.1$, at a frequency of 5 Hertz. Again, in order to determine the life (number of cycles) at onset of delamination, and to document the life-damage-growth history, specimens are periodically removed from the tester and inspected by x-radiography. In each type of laminate, at least three fatigue load levels were selected for the

fatigue tests. In general, all the selected fatigue load levels are below the static load for which onset of delamination occurs.

The following laminates were studied in tension-tension fatigue:

$[45/-45/0/90_2]_s$

$[45/-45/0/90_2]_s$ - type A

$[45/-45/0/90_2]_s$ - type B

and the following laminates were studied in compression-compression fatigue:

$[45/-45/0/90_2]_s$

$[0_2/90_2/45_2/-45_2]_s$

$[0_2/90_2/45_2/-45_2]_s$ - type A

$[0_2/90_2/45_2/-45_2]_s$ - type C

$[90_2/0_2/-45_2/45_2]_s$

$[0/90/0/90/45/-45/45/-45]_s$

$[0/90/0/90/45/-45/45/-45]_s$ - type A

$[0/90/0/90/45/-45/45/-45]_s$ - type C

Table 3 summarizes these tests, the number of fatigue load levels and the number of specimens used in each test.

2. **Discussion of Experimental Results**

(a) **Base-line Property Tests** - Results from all the static property characterization tests were within the normal range of values for this material. Average properties for each of the laminates are summarized in Table 4. In particular, the basic properties obtained from the unidirectional laminates are:

11

	Tension	Compression
E_L	140 GPa	137 GPa
E_T	11.1 GPa	-
ν_{LT}	0.29	0.28
ν_{TL}	0.027	-
G_{LT}	5.6 GPa	5.4 GPa
Fiber volume, %	66.5	
Sp. gravity	1.55	

It is noted that the longitudinal Young modulus E_L and Poisson ratio ν_{LT} from both the tension test and the compression test are essentially the same. Also, in obtaining the in-plane shear modulus G_{LT} for the unidirectional laminate, data from $[\pm45]_{2s}$ were used. Specifically, the average values for E_x and ν_{xy} found from $[\pm45]_{2s}$ are used in computing G_{LT} approximately by the formula:

$$G_{LT} \sim E_x/2(1 + \nu_{xy}).$$

The values of G_{LT} calculated using tension test results and using compression test results are also very close; see Table 4.

However, the values for the compressive strength from Table 4 should be viewed with caution. They are uniformly lower than the tensile strengths, especially for $0°$-ply dominant laminates. It is suspected that the ultimate compressive laminate failures may have involved some degree of structural buckling.

(b) <u>Static Load-Delamination Growth Tests</u> - In this series of tests, eight different laminates were tested under step-tension loading, and nine different laminates were tested under step-compression loading. In each case, the various parameters effecting delamination have been investigated.

12

Delamination Growth by Tension

The first group of laminates examined were the quasi-isotropic laminates, $[0_2/90_2/45_2/-45_2]_s$ and $[90_2/0_2/-45_2/-45]_s$. In each case, three specimens were tested. The difference between the two types of laminates is basically the stacking sequence of the 0°-ply and the 90°-ply. Under uniaxial tension, both laminates suffered transverse cracking in the 90°-ply during the early stage of loading. As the applied load increased, cracks were observed in the $\pm 45°$ plies at about 80% ultimate load. Edge delamination in the $\pm 45°$ interface was first observable at about 90% ultimate load. Both laminates failed at essentially the same ultimate load of 540 MPa (68.4 ksi).

Fig. 5 displays the load-sequence x-radiographs of a $[0_2/90_2/45_2/-45_2]_s$ laminate under tensile loading. It is seen that transverse cracks in the 90°-direction are visible from about 255 MPa load. The crack density increases with the applied load until $\pm 45°$ cracks appear at about 426 MPa. These $\pm 45°$ cracks increased rapidly with load, causing edge delamination which initiated at about 520 MPa. The delamination propagated unstably, resulting in laminate failure at 540 MPa.

A set of similar load-sequence x-radiographs for the $[90_2/0_2/-45_2/45_2]_s$ laminate is shown in Fig. 6. Here, it is observed that onset of 90° transverse cracks occurred at about 234 MPa, onset of $\pm 45°$ cracks occurred at about 380 MPa, and onset of edge delamination at 442 MPa. The final laminate failure occurred at 540 MPa; this is the same load as in the $[0_2/90_2/45_2/-45_2]_s$ laminate shown in Fig. 5. A comparison between these two sets of results is given in the following:

laminate	Onset stress, MPa			
	90°-crack	+45°-crack	edge delam.	final failure
$[0_2/90_2/45_2/-45_2]_s$	255	426	520	540
$[90_2/0_2/-45_2/45_2]_s$	234	380	442	540

Clearly, the onset stresses for the different cracking events are uniformly lower in the second laminate than in the first. Also, it seems that growth of edge delamination is the cause of final failure for both laminates. The difference exhibited by these two sets of results are explained by the energy analysis, which is to be discussed in Section III.

The second group of laminates examined were $[0/90/0/90/45/-45/45/-45]_s$ and $[90/0/90/0/-45/45/-45/45]_s$. These are simply the same two quasi-isotropic laminates examined previously with their stacking plies dispersed, so that no two plies of the same fiber orientation are stacked together. By dispersing the stacking plies, the laminate stiffness properties do not change, see Table 4. However, the behavior of the sub-laminate cracking events is changed by ply-dispersion. In the step-tension tests, both laminates showed 90°-cracking at the applied load of 434 MPa; neither $\pm$45°-cracking nor edge delamination was observed before the laminate final failure. Furthermore, the final laminate failure load for both laminates was over 620 MPa, or 15% higher than the undispersed laminates.

These results show clearly the influence of ply thickness on the sub-laminate cracking behavior as well as the final strength of the laminate. Energy analysis on this subject is also included in Section III.

The next group of laminates tested were the $[\pm45/0/90_2]_s$ series. Three types were examined: the plain (without implant), the type A (with 1/4" Teflon strip implanted) and the type B (with 1/2" Teflon strip implanted); see dimensions given in Fig. 2.

When loaded in tension, tensile edge stress σ_z is induced throughout the 90°-plies. This σ_z stress is thus responsible for edge delamination in the 90°-plies. Test results show the following cracking activities:

90°-crackings occurred at about 131 MPa in the plain laminates,
and occurred at about 103 MPa in both type A and type B laminates. Edge
delamination became observable at about 223 MPa in the plain laminates, and
about 180 MPa in type A and type B laminates. All three types had the same
average failure stress of about 438 MPa. These results are summarized in the
following

type of laminate	onset stress, MPa		
	90°-cracking	edge delam.	final failure
[±45/0/90]$_s$	131	223	443
type A	103	179	436
type B	103	172	435

Clearly, the presence of interlaminar defects in the type A and type B
laminates has some measurable adverse effect on the initiation of transverse
cracking and edge delamination. But the final failure load of the laminates
is not affected. This suggests that the growth behavior of the sub-laminate
cracking events is probably quite stable, and that the extent of sub-laminate
damage prior to final failure is also the same in all three types of laminates.
Indeed, from the load-sequence x-radiographs shown in Figs. 7, 8 and 9, it is
seen that in all cases, free edge delamination growth is extremely stable.
The influence of the implanted defect becomes insignificant as the applied
load approaches its ultimate.

Fig. 10 illustrates graphically the 90°-cracking and edge delamination
growth as a function of the applied load. It is seen that the planted inter-
laminar flaws had little effect on the growth behavior. It is essentially
negligible as the applied load reaches the ultimate.

Again, energy analysis of the cracking events for this series of
laminates is included in Section III.

Finally, several specimens of $[\overline{\mp45/90/0_2}]_s$ configuration were also tested. An interlaminar edge stress analysis would show that the edge normal stress σ_z is compressive. Thus, no delamination is expected in such a laminate configuration. In the step-loading experiment, some 90°-cracking was observed from about 820 MPa which is 88% the ultimate strength of the laminate (σ_{ult} = 935 MPa). Even prior to final failure, there was no noticeable $\pm45°$-cracking or free edge delamination observed.

Table 5 summarizes all the test results obtained for the eight types of laminates. Major findings from this series of tests may be briefly stated as follows:

(1) Between the laminates $[0_2/90_2/45_2/-45_2]_s$ and $[90_2/0_2/-45_2/45_2]_s$, very little difference exists in terms of laminate behavior, including their stiffnesses and the stress states. Initiation of 90°-cracking occurred early in the loading for the second laminate. This sub-laminate damage event influenced, in turn, an early onset of $\pm45°$-cracking and edge delamination in the $\pm45°$ interface. Although the ultimate load for both laminates was the same, the process of damage development before final failure is not.

(2) Between the laminates $[0_2/90_2/45_2/-45_2]_s$ and $[0/90/0/90/45/-45/45/-45]_s$, the difference exhibited in sub-laminate damage development is significant. The following comparison shows their strikingly different behavior

laminate	Onset stress, MPa			
	90°-cracking	$\pm45°$ cracking	Edge Delam.	Final failure
$[0_2/90_2/45_2/-45_2]_s$	255	426	520	540
$[0/90/0/90 \cdots]_s$	434	–	–	607

The effect of ply thickness on both crack initiation and growth behavior is clearly demonstrated here. It is an important parameter in the fracture mechanisms associated with these cracking events.

(3) For the $[\pm45/0/90_2]_s$ series, the effect of implanted interlaminar defect is relatively unimportant if the laminates are under tension (static loading). The defects do cause early initiation of damage growth, emanating from the defect. This could be a factor in situations where unstable damage growth is dominant, however.

Delamination Growth by Compression

Two major groups of laminates were tested by static step-compression. The first group consisted of the $[0_2/90_2/45_2/-45_2]_s$ laminates, and included those with a Teflon strip implant (type A), and those with a Teflon circular disk (type C) implanted in the mid-plane. The purpose of testing this grouped-ply laminates was simply to see the effect of the implanted defects on delamination under compressive loading.

The second group of laminates were the "dispersed" laminates; namely, the $[0/90/0/90/45/-45/45/-45]_s$ and included both type A and type C implants. Thus, between the two groups, the ply-grouping effect on delamination can be evaluated for the compression loading cases.

In addition, some $[0_{12}]$, $[90_2/0_2/-45_2/45_2]_s$ and $[\pm45/0/90_2]_s$ laminates were also tested by step-compression. For $[0_{12}]$, it was hoped to detect any fiber splitting during the step-loading, or any other matrix-dominated cracking prior to final failure. As for the $[90_2/0_2/-45_2/45_2]_s$, its behavior should be identical with the $[0_2/90_2/45_2/-45_2]_s$ under compression. And, of course, the $[\pm45/0/90_2]_s$ should exhibit no delamination under such loading, as well.

17

Figs. 11, 12 and 13 show, respectively, the load-sequence x-radiographs of the $[0_2/90_2/45_2/-45_2]_s$, type A and type C laminates. Free edge delamination was observed at various loading levels, depending on the type of laminates. The following shows the onset loads at delamination and failure:

laminate	Onset stress, MPa	
	Edge delam.	final failure
$[0_2/90_2/45_2/-45_2]_s$	339.2	369.5
$[0_2/90_2/45_2/-45_2]_s$ - A	131.0	286.0
$[0_2/90_2/45_2/-45_2]_s$ - C	252.0	331.0
$[90_2/0_2/45_2/-45_2]_s$	316.0	320.0

From the above, it is seen that in the plain $[0_2/90_2/45_2/-45_2]_s$ and $[90_2/0_2/45_2/-45_2]_s$ laminates, onset of edge delamination led immediately to final laminate failure; the growth of delamination was unstable.

In the type A laminates, the implanted teflon strip is exposed at the free edges. This defect caused an early but stable edge delamination growth, as is seen in the x-ray pictures depicted in Fig. 12. This growth also pre-cipitated a lowered final failure stress for the laminates (about 25% lower).

The implant in the type C laminate is in the interior; it has no effect on the free edges of the laminates. Initially, there are two independent delam-ination initiators, the implant and the free edges. Apparently, the implanted circular disk had less effect on delamination than the free edge. As is seen in the load-sequence x-ray pictures in Fig. 13, edge delamination was the first event to occur. Once edge delamination started, however, the internal circular patch affected the growth behavior, resulting in a lowered final failure load for the laminates.

The delamination growth behavior of these three types of laminates is illustrated in Fig. 14 where the amount of delamination growth (in % of delaminated area) is plotted against the applied load. It is seen that delamination growth in the $[0_2/90_2/45_2/-45_2]_s$ laminates is almost catastropic following the initiation. Type C laminates had a relatively stable growth, while type A laminates had the most stable growth. The effect of the interlaminar defect on delamination was significant. This is in contrast with the results from tensile step-loading, where the effect of interlaminar defects on delamination was relatively insignificant; see Fig. 10.

Figs. 15, 16 and 17 display the load-sequence x-radiographs for the three types of laminates in the second group. Recall that in this group, the ply stacking sequence of the previous laminate is dispersed. The following table shows the comparisons of the onset loads of delamination and final failure for these laminates:

laminates	Onset stress, MPa	
	edge delam.	final failure
$[0/90/0/90/45/-45/45/-45]_s$	379.2	425.4
$[0/90/0/90/45/-45/45/-45]_s$ - A	138.0	382.6
$[0/90/0/90/45/-45/45/-45]_s$ - C	265.4	365.4

Again, it is seen that edge delamination was the initial damage event precipitating failure in all the laminates. The effect of an interlaminar defect on the initiation of delamination remains as significant as in the previous undispersed laminates. Fig. 18 illustrates the various delamination growth developments as functions of the applied load.

Between the two groups of laminates, the undispersed and the dispersed, the important difference is again caused by the parameter of ply thickness. Fig. 19 shows the delamination growth behavior between the undispersed and the dispersed laminates.

Table 6 summarizes all the results obtained in this series of
tests. It is clear that interlaminar defects have a significant adverse
effect on delamination when the laminates are subjected to compression. In
addition, the ply thickness parameter continues to play an important role
in the delamination growth processes.

(c) Fatigue Life - Delamination Growth Tests - In this series of tests, both
tension-tension fatigue and compression-compression fatigue tests were
conducted. Details of test results are discussed in the following.

Tension-Tension Fatigue Tests

In the tension-tension fatigue experiment, only the $[\pm45/0/90_2]_s$ and
the associated type A and type B laminates were tested. For the $[\pm45/0/90_2]_s$
laminates, five fatigue load levels were selected. These were one load level
below, three load levels above, and one load level at about the static
onset load of transverse cracking in the 90°-plies. The purpose of these
tests was to establish some quantitative damage growth rates in terms of the
fatigue load and the fatigue life. A typical life-sequence of x-radiographs
for the $[\pm45/0/90_2]_s$ laminate tested under σ_f = 189 MPa is shown in Fig. 20.
Since the maximum fatigue load is higher than the static onset load for
transverse cracking (at 131 MPa), it is seen from the x-radiographs that
multiple 90°-cracks occur very early during the fatigue loading. As the
fatigue cycling increases, the crack density also increases. At about
1000 cycles, free-edge delamination becomes identifiable. The delamination
then grows with increasing fatigue cycles.

Fig. 21 shows the growth of the 90°-cracks as a function of fatigue
cycles, while Fig. 22 displays the delamination growth. It is seen from these
figures that free edge delamination at all fatigue load levels occurs whenever

the transverse crack density reaches 8 ~10 cracks per cm. From there on, edge delamination becomes the dominant damage mode, which leads steadily to final laminate failure.   Both Fig. 21 and Fig. 22 suggest a certain damage growth rate dependent upon the maximum fatigue load, σ_f, and the cyclic loading history, N. The exact form for such a growth model will be discussed in Section IV.

The effect of interlaminar defects on this laminate series under tension fatigue may be determined from the x-radiographs taken for a $[\pm 45/0/90_2]$ - A laminate and a $[\pm 45/0/90_2]$ - B laminate, shown respectively by Fig. 23 and Fig. 24. Both laminates were cycled under a maximum fatigue load of 189 MPa. It is observed from both cases that 90°-cracking occurs early in the fatigue life, followed promptly by edge delamination eminating from the inter-laminar flaw. Thus, the presence of different interlaminar flaws had only a small effect on the growth of 90°-cracking, but precipitated early delamination initiation. Fig. 25 shows the delamination growth under the same fatigue load (189 MPa) for the three types of laminates. Clearly, the effect of implanted flaws is significant enough that it should not be disregarded, although its effect on static tension strength was found to be minimal.

Results obtained from tests at other fatigue load levels are summarized in Table 7.

Compression-Compression Fatigue Tests

As in the case of the static compression tests, two major laminate series were also tested under compression-compression fatigue loads. These two series were (a) the $[0_2/90_2/45_2/-45_2]_s$ and the associated type A and type C laminates, and (b) the dispersed $[0/90/0/90/45/-45/45/-45]_s$ and the

associated type A and type C laminates. In addition, laminates of $[\pm45/0/90_2]_s$ and $[90_2/0_2/-45_2/45_2]_s$ were also tested. In each case, two or three fatigue load levels were selected; see Table 8.

For the $[0_2/90_2/45_2/-45_2]_s$, type A and type C series, typical x-radiographs are displayed, respectively, in Figs. 26, 27 and 28. These were all under a 222 MPa maximum fatigue load. This load is much higher than the static onset load for delamination for type A laminate (131 MPa), but is lower than that for the plain and the type C laminates (339 MPa and 252 MPa, respectively). Thus, in the case of type A laminate, edge delamination was found during the first cycle of loading. Growth of delamination was rather stable until fatigue life exceeds 10^4 cycles. For the plain and the type C laminate, delamination occurred later in the fatigue life but with a faster growth rate.

Fig. 29 shows the delamination growth curves obtained from three fatigue load levels for the plain laminates. The growth rates in these curves are higher compared with those found under tension fatigue. The same growth behavior is observed also for the type A and type C laminates, see Fig. 30 and Fig. 31, respectively. Both show an accelerated growth rate under compression fatigue. This result is thought to be due to the buckling action of the test specimen under compression. This behavior must be considered in any growth model formulation.

The effect of implanted interlaminar flaws is illustrated in Fig. 32. Under a 221 MPa fatigue load, it is seen that edge delamination initiates at different lives depending on the type of flaw implanted. For instance, type A laminate suffers delamination at the first cycle, type C begins to show delamination at about 200 cycles, while the plain laminate shows delamination at a life exceeding 2000 cycles. The rate of growth in all three cases takes

22

a sharp increase at about 25% delamination, and the fatigue lives of all three cases remain within one decade of variation of each other.

The purpose of testing the $[0/90/0/90/45/-45/45/-45]_s$ and the associated type A and type C laminates was again to assess the effect of ply-grouping when the loading condition is compression-compression fatigue. In the experiments on this series of laminates, the same general behavior was found as in the previous series. In all cases, edge delamination was induced under the fatigue loads, and while the effect of the implanted flaw was noticeable, it was not significant.

Figs. 33, 34, and 35 illustrate respectively, the growth of delamination by a life-sequence of x-radiographs for the plain (under 276 MPa), type A and type C (both under 219 MPa) laminates. From these x-radiographs, delamination growth curves can be obtained. Fig. 36 shows a typical set of delamination growth curves for the type A laminate under three different fatigue load levels. It is noted that these curves are similar with those found earlier for the $[0_2/90_2/45_2/-45_2]_s$ series, except that delamination growth is suppressed by the dispersion of the plies.

In order to see the ply-grouping effect more quantitatively, examine the comparative growth curves shown in Figs. 37, 38, and 39. In all cases, the dispersed laminates, whether they contain implanted flaws or not, display a much "stronger" behavior against delamination than their undispersed counterparts. The dispersed laminates show more than 2 decade longer life than the undispersed. This significant simple geometrical parameter is seen to have a dominant effect on the failure mechanisms of the laminates.

Finally, test results for the $[\pm 45/0/90_2]_s$ and $[90_2/0_2/-45_2/45_2]_s$ laminates were as expected. The $[\pm 45/0/90_2]_s$ failed in fatigue without any edge delamination, and the $[90_2/0_2/-45_2/45_2]_s$ behaved similarly to $[0_2/90_2/45_2/-45_2]_s$

All these results are summarized in Table 8.

III. AN ENERGY METHOD FOR SUB-LAMINATE CRACK GROWTH

In this section, the approach being taken in the development of a crack growth model will be described. To this end, a brief review is presented describing the major sub-laminate crack mode and the classical fracture concept of strain energy release rate. Finally, the cracking events documented from experiments will be analyzed using the energy model presented in this section.

1. Physical Processes of Transverse Cracking and Edge Delamination

Examination of the earlier test results show that matrix and/or matrix-fiber interface damage almost always precedes the laminate failure. Particularly, 90°-cracking (transverse cracks) and free-edge delamination have been identified as the two major damage modes which precede the final failure in the laminates studied in this report. In order to properly model each of these cracking processes, a closer analysis of the mechanisms of these events becomes essential.

(a) Transverse Cracking Process Transverse cracks form in plies when a sufficiently large tensile stress exists transverse to the fibers. Consider, for example, a cross-ply $(0/90)_s$ laminate which is subjected to tension in the 0°-direction; at some critical stress level, the 90°-ply begins to suffer transverse cracks. Laboratory experience indicates the following characteristics of the transverse cracking process:

Reproducible Onset Load   In a given population of identical specimens subjected to identical test conditions, the critical load at initiation of transverse cracking is surprisingly reproducible, especially in view of the large scatter experienced in material properties (such as the transverse strength of a 90°-laminate). This suggests that the transverse crack initiation mechanisms are predominantly influenced by the geometrical conditions surrounding the crack, rather than by the material property variations.

25

<u>Thickness Effect and Shear Lag</u> X-radiographs in earlier experiments showed
that transverse cracks in the 90°-ply generally follow the matrix-fiber inter-
face; in a trans-thickness view, such as sketched in Fig. 40, the crack is
believed to form inside the 90°-ply, and extend vertically across the 90°-ply,
eventually terminating at the 0°-90° interface. Clearly, the outside 0°-plies
must have a restraining and arresting effect as the transverse crack approaches
this interface.

If strain energy is released as the transverse crack propagates, it is
easy to see that the farther a transverse crack is allowed to propagate (i.e.,
the thickness of 90°-ply is larger) the greater the strain energy released
by the propagating crack. Thus, from the energy point of view, a thin
90°-ply layer can provide only a small amount of energy release. Consequently,
a higher applied load is required to propagate a crack in the thin 90°-ply
layer. This, of course, is consistent with the experimentally observed
thickness effect, discussed extensively in Section II.

After the transverse crack is arrested at the 0°/90° interface, the load
normally carried by the 90°-ply before the crack must now be transmitted
through the 0°/90° interface, creating a local region of interlaminar shear
stress distribution, called the shear lag. Obviously, the size of the shear
lag depends again on the thickness of the 90°-ply layer. Generally, it is
about 4-times the thickness of the 90°-layer.

Theoretically, if the material properties of the 90°-layer are perfectly
uniform, then any two adjacent transverse cracks must maintain a minimum dis-
tance equal to the shear lag. Thus, at the onset of transverse cracking, one
would actually see multiple cracks that are separated by the shear-lag spacing.
This has been referred to as the "characteristic spacing" by Reifsnider,
<u>et al</u>. [28].

In actuality,however, the variability of the material properties distortes the so-called "characteristic spacing." The growth of the transverse cracking is a continuous function of the applied load, as observed in the earlier experiments. The lack of a "characteristic spacing" complicates the definition of cracking initiation; and necessitates a statistical approach to address the random nature of the material variability.

Effect of Transverse Cracking on Edge Delamination   The aforementioned shear-lag region may suffer local damage in the form of delamination, due to the concentration of interface shear stress near the transverse crack-tip. Since the size of the shear-lag is proportional to the 90°-ply layer thickness, the likelihood of transverse cracking induced delamination also increases with the 90°-layer thickness. Thus, a laminate which is already delamination prone due to edge effects will suffer a compounded delamination growth if it under-goes simultaneously transverse cracking. Such an interacting effect is 3-dimensional in nature, and requires 3-dimensional crack-modeling.

(b) Edge Delamination Process   As has been discussed earlier in Section I, edge delamination stems from the boundary edge stresses which exist along ply interfaces near the laminate free edges.   These interlaminar stresses can be computed accurately by a stress analysis based on ply elasticity. Again, consider as an example the $(0°/90°)_s$ laminate subjected to uniaxial tension. An edge stress analysis will show (see e.g., Ref. 14) that a tensile σ_z stress exists throughout the 90°-ply layer, and a combination of tensile σ_z and shearing τ_{xz} exists along the 0°/90° interface. Under these stresses, a mode-I crack along the mid-plane (90°/90° interface), or a mixed-mode crack along the 0°/90° interface are both possible, depending on which of the two possible sites meet the cracking conditions.

Furthermore, the edge stresses exist only within a small boundary edge region. The size of the boundary region is again found to depend on the thickness of the layers along whose interface the edge stresses are distributed. Hence, the thicker the material layers, the larger the size of the boundary region. If an interlaminar crack is to form in this region, it may be inferred again that the available strain energy released during the formation of the crack is limited by the layer thickness. Or, alternatively, the critical load at onset of edge delamination depends on the material layer thickness. This is also clearly consistent with the experimental results.

Once the free edge crack is formed, the boundary region propagates inward to the interior of the laminate. If the width of laminate is large compared to the size of crack, stable growth will follow. Otherwise, the growth may become unstable.

The foregoing physical analyses are based primarily on experimental observations. With this understanding, the development of a descriptive model will be presented next, on the basis of the energy release rate concept.

2. The Strain-Energy Release Rate Concept

The concept of the strain energy release rate as a fracture growth criterion for brittle cracks in elastic solids is of long standing. In his first paper published in 1920, Griffith [29] attributed the ultimate tensile strength of glass to the propagation of crack-like surface flaws; stress concentration surrounding the worst (largest) flaw cause unstable propagation. He postulated that a change (increase) in the crack size causes a decrease in the stored strain energy near the crack-tip; at the same time, the solid body increases its surface area so that the total surface energy is also increased.

28

Let U be the strain energy and S the surface energy; then for an initial flaw
of size a, a crack growth is induced if

$$\frac{\partial U}{\partial a} \geq \frac{\partial S}{\partial a} \qquad (3-1)$$

The quantity $\partial U/\partial a$ depends on the stress field near the crack-tip which
in turn depends on the geometry of the crack and the magnitude of the applied
load. This quantity represents the driving force, and is commonly referred to
as the available energy release rate, $G(a)$. The quantity $\partial S/\partial a$ depends on
the microstructure of the material and the magnitude of the molecular bond;
it is thus considered a material property, representing the resistance of
the material against crack growth. It is also commonly called the critical
energy release rate, G_c. For most materials, G_c is a constant, independent
of the crack size or the applied load (but may depend on the crack direction).

The Griffith crack growth criterion, (3-1) may be rewritten in the form

$$G \geq G_c. \qquad (3-2)$$

(a) <u>The Crack-Closure Representation</u> From an elastic energy balance con-
sideration, Irwin [25] showed that the strain energy released in an incre-
mental crack extension can be equated to the amount of work done required to
close it again. Let Δa represent an infinitesimal crack extension from the
initial crack of size a, as shown in Fig. 41. Let $\Delta \tilde{u}$ be the relative dis-
placements between the mating surfaces along Δa when the crack extension is
open, as in Fig. 41(b); let $\tilde{\sigma}$ be the surface stresses along Δa when the crack
extension is closed, as in Fig. 41(c)

Then, the work done in closing the crack extension Δa can be expressed as

$$\Delta W = \frac{1}{2} \int_0^{\Delta a} \tilde{\sigma} \cdot \Delta \tilde{u} \; da \qquad (3-3)$$

By Irwin's elastic energy balance, the strain energy release rate corresponding to the crack of initial size a is given by

$$G = \lim_{\Delta a \to 0} \frac{1}{2\Delta a} \int_0^{\Delta a} \tilde{\sigma} \cdot \tilde{\Delta u} \, da \tag{3-4}$$

Substituting the normal and shearing stress components of the surface stress $\tilde{\sigma}$, and the relative displacement $\tilde{\Delta u}$ into (3-4), the modal components of G are obtained as

$$G_I = \lim_{\Delta a \to 0} \frac{1}{2\Delta a} \int_0^{\Delta a} \sigma_y \, \Delta v \, da$$

$$G_{II} = \lim_{\Delta a \to 0} \frac{1}{2\Delta a} \int_0^{\Delta a} \tau_{xy} \, \Delta u \, da \tag{3-5}$$

$$G_{III} = \lim_{\Delta a \to 0} \frac{1}{2\Delta a} \int_0^{\Delta a} \tau_{yz} \, \Delta w \, da$$

where G_I, G_{II} and G_{III} are, respectively, the energy release rates corresponding to the mode-I, mode-II and mode-III crack opening, such as illustrated in Fig. 42. The total energy release rate of the generally mixed-mode crack extension is given by

$$G = G_I + G_{II} + G_{III} \tag{3-6}$$

(b) <u>The Finite-Element Scheme</u> In order to evaluate the integrals in (3-4) or (3-5), the exact stress field near the crack-tip must be determined. But, the stress field surrounding a sharp crack is singular in nature; and in a generally anisotropic solid, the mode-I, mode-II and mode-III cracking actions are mutually coupled. Thus, the crack-closure representation of Irwin's must be adapted by applying a finite element approximation for problems involving complicated layering structures. A technique of

nodal-release-and-close has been implemented recently by Wang and Crossman [20] to approximate the Irwin integrals of (3-5). Fig. 43 illustrates the finite element representation of the crack-tip region shown in Fig. 41(a). Here, the crack of size a is shown with the crack-tip at node C. Under a given far field loading condition, the displacements of node C, $\breve{u}_c$, can be determined by the finite element solution. Then, a small incremental crack extension (self-similar, for instance) Δa is introduced by opening up node C, with node C becoming two separate nodes f and g, as shown in Fig. 43(b). A new round of finite element solutions is obtained, given the new crack geometry (the far field loading condition remains unchanged). This provides the nodal displacements of node f and node g, denoted respectively by $\hat{u}_f$ and $\tilde{u}_g$. The last step is to force-close node f and g to return to the original position of node C by prescribing the common displacement $\breve{u}_c$ for both node f and node g. The finite element solution of the last step gives the necessary nodal force $\tilde{F}_c$ required for the closure. The work done in the process of a finite crack-closure is given by

$$\Delta W = \frac{1}{2} [F_x(u_f-u_g) + F_y(v_f-v_g) + F_z(w_f-w_g)] \qquad (3-7)$$

Thus, for approximation, the strain energy release rate G may be expressed as *

$$G = \Delta W/\Delta a. \qquad (3-8)$$

•

---

* The adequacy of this kind of approximation has been a source of great concern. A more detailed assessment of such approximation is found in Ref. [20].

Consequently, the modal components of G corresponding to the initial crack
of size a are represented by

$$G_I = F_y(v_y - v_g)/2\Delta a$$

$$G_{II} = F_x(u_f - u_g)/2\Delta a \qquad (3-9)$$

$$G_{III} = F_z(w_f - w_g)/2\Delta a$$

By successively opening and closing the nodes along a prescribed crack
path, the energy release rate G can be computed as a function of the extend-
ing crack's size, i.e., $G = G(a)$ under a given far-field loading condition.

(c) Sub-laminate Crack Initiation and Growth Criteria   In this study, the
only sub-laminate cracks investigated are the 90°-cracking and the free-edge
delamination. In order to set up a crack initiation and growth criterion for
each of the two types of cracking, it is assumed that micro-flaws exist
along the fiber-matrix interface, and also along the ply-to-ply interface.
These flaws are generally of a size in the order of the fiber diameter. This
dimension is in the realm of micro-mechanics, whose crack propagation mech-
anisms will not be dealt with here. Instead, it is postulated only that these
micro-flaws would propagate and coalesce into a macroscopic proportion under
a certain critical far field loading condition. The resulting crack is
recognizable only at the macro-scale, where the basic axioms of ply-elasticity
are valid*. The minimum crack size first formed at the macro-scale depends on
the micro-structure of the material (perhaps also on a host of other material
processing factors, such as the curing process, post-cure handling, etc).

---

* One of the basic axioms in ply-elasticity is that within each layer the
  material is represented by a homogeneous, anisotropic medium. Material dis-
  continuity exists only across the interface of two different material layers.

This minimum macro-crack size is also called the critical flaw size, denoted by a_c. The value of a_c is generally unknown and can be random in nature. It is then regarded as a material property at the macroscopic level.

The Griffith criterion of (3-2), when applied to predict the initiation of a sub-laminate cracking, is replaced by

$$G(a_c) \geq G_c. \tag{3-10}$$

And, the stability of growth following initiation is governed by the conditions:

$$G(a + \Delta a) < G_c; \quad \text{stable growth} \tag{3-11}$$

$$G(a + \Delta a) > G_c; \quad \text{unstable growth} \tag{3-12}$$

and

$$G(a + \Delta a) \sim G_c; \quad \text{neutral growth} \tag{3-13}$$

where $a(> a_c)$ is the instantaneous crack size for which the growth stability is to be determined.

3. Finite Element Models

In the foregoing discussions, the available energy release rate function $G(a)$ was left in general terms. For the specific modeling of the transverse cracking and free edge delamination, $G(a)$ must be appropriately calculated by the finite-element crack-closure procedures discussed earlier. Details of the specific models are discussed in the following.

(a) Transverse Cracking Model   The finite element representation for the transverse cracking is illustrated in Fig. 44. Under the idealized cracking geometry as shown in Fig. 44(a), the growth path of the crack is represented by Fig. 44(b). The solution domain is in the 2-dimensional x-z plane,

although the plane may undergo warping in the y-direction. Thus, a generalized

plane strain formulation (see, e.g., Ref. [14]) was adapted in the finite

element routine.

Fig. 45 shows a typical finite element mesh for the growth of transverse

cracking. As has been postulated previously that an initial macro-flaw of

size a_c exists in the 90°-plies, and this crack can be propagated to reach the

interface of the face-plies as shown in the figure. Hence, if the laminate is

subjected to a uniaxial tension represented by a far field uniform displace-

ment δ, the energy release rate function $G(a)$ may be calculated and expressed

by

$$G(a) = [C_e(a)\bar{e}_x^2]t, \quad a > a_c \tag{3-14}$$

where t is a characteristic length (e.g., thickness of a ply) and $\bar{e}_x$ is the

far field laminate strain induced by δ. The coefficient function $C_e(a)$ is

calculated by imposing $\bar{e}_x = 1$.

Fig. 46 shows the general behavior of $C_e(a)$ for the crack in the lami-

nate shown. Note that the crack size a is limited by the thickness of the

90°-layer, b. The strain energy available increases initially with the in-

crease of cracking size; as the crack approaches the ply interface, the

available energy begins to decrease; the rate of decrease depends on the rel-

ative rigidity of the outside layer. Generally, a maximum is located at about

$a = 0.9b$.

Similarly, if the laminate is subjected to a uniform temperature drop

of Δt, and if tensile stress in the 90°-layer is also induced, then the calcu-

lated energy release rate function for the transverse crack is expressed by

$$G(a) = [C_T(a)\Delta T^2]t, \quad a > a_c. \tag{3-15}$$

Typical behavior of $C_T(a)$ for a transverse crack is similar to that of $C_e(a)$, as shown in Fig. 46. Again, $C_T(a)$ is generated by imposing $\Delta T = 1$.

In practice, all laminates are subjected to thermal residual stresses before test; and its effects on sub-laminate cracks are not insignificant. The effect of such residual stresses may be simply included in the form of a uniform thermal load, such that

$$\Delta T = T_c - T_0 \qquad\qquad (3\text{-}16)$$

where T_c is the curing temperature and T_0 the ambient testing temperature. Thus, when the laminate is loaded by uniaxial tension, a combined loading condition must be considered. The calculated energy release rate function takes the form

$$G(a) = [C_e(a)\bar{e}_x^{\,2} + C_{eT}(a)\bar{e}_x(\Delta T) + C_T(a)(\Delta T)^2]t \qquad (3\text{-}17)$$

where $C_{eT}(a)$ is generated by results for $\bar{e}_x = 1$, and $\Delta T = 1$.

Note that the cracking action of the transverse cracks is primarily of mode-I, the opening mode.

Accordingly, for a given laminate geometry, say $(\pm 45/0/90_2)_s$, onset of 90°-cracking in the 90°-layer can be determined if the coefficient functions $C_e(a)$, $C_{eT}(a)$ and $C_T(a)$ are calculated. Then by setting ΔT and a_c to known values and by letting $G(a_c) = G_c$, Eq. (3-17) determines the far-field strain $\bar{e}_x$ at the onset of cracking. From $\bar{e}_x$, the far-field applied load is then obtained; $\sigma_x = E_x \bar{e}_x$.

(b) <u>Free Edge Delamination Model</u> The finite element representation for the free edge delamination is illustrated in Fig. 47 and Fig. 48. For symmetrically stacked laminates, edge delamination may occur along the mid-plane (y-axis), or the off-mid-plane interfaces. The mid-plane cracking is illustrated in

Fig. 47, while the off-mid-plane cracking is illustrated in Fig. 48. In both cases, the solution domain is the 2-dimensional y-z plane, with the applied load in the x-direction. Again, a generalized plane strain condition is assumed, if the edge cracking is idealized as illustrated. Fig. 49 depicts a typical finite element mesh for an edge delamination that occurs along a chosen ply interface.

The edge crack begins with the assumed macroscopic interface flaw of size a_c, and it is propagated self-similarly away from the edge boundary. If the applied far field load is represented by the laminate strain $\bar{e}_x$, the calculated energy release rate function again takes the form of Eq. (3-14). And, if a combined thermal and mechanical loading condition is considered, the $G(a)$ function takes the form of Eq. (3-17).

A typical $G(a)$ function for an edge delamination growth is displayed in Fig. 50. Its behavior is slightly different from that for the transverse cracking. It is seen from Fig. 50 that the available energy release function $G(a)$ increases initially with the crack growth to reach a maximum value at $a \sim$ the thickness of the layers containing the interface crack; beyond this point, $G(a)$ remains at a constant value.

Hence, for a given laminate geometry and at a chosen interface cracking site, the coefficient functions $C_e(a)$, $C_{eT}(a)$ and $C_T(a)$ must first be generated numerically. Then by given ΔT and a_c values, the applied far-field strain $\bar{e}_x$ is determined from (3-17) by letting $G(a_c) \rightarrow G_c$.

Note that a mid-plane cracking is primarily mode-I action, while an off-mid-plane cracking is generally a mixed-mode action. In the latter case, $G(a)$ is the total energy release rate, consisting of all three modal components, as stated by Eq. (3-6).

36

4. Numerical Correlation with Experimental Results

The AS-3501-06 graphite-epoxy material ply is assumed as a homogeneous medium having elastic orthotropic property in the principal material coordinates. The effective (or macroscopic) moduli of material have been determined in the basic material characterization experiments, see Table 4. Specifically, these are given as

$$E_L = 140 \text{ GPa}; \quad E_T = E_z = 11.1 \text{ GPa}$$
$$G_{LT} = G_{Tz} = G_{Lz} = 5.5 \text{ GPa}$$
$$\nu_{LT} = \nu_{Lz} = 0.29 \tag{3-18}$$
$$\alpha_L = 0.36 \times 10^{-6}/°C; \quad \alpha_T = \alpha_z = 28.8 \times 10^{-6}/°C$$

In addition, the average thickness of a single ply is $t = 0.0136$ cm.

Since the laminates were fabricated under a curing temperature of 177°C, and were tested under the average ambient temperature of 22°C, the equivalent thermal load in the laminates is approximately

$$\Delta T = -155°C \tag{3-19}$$

The critical strain energy release rate G_c appropriate with the kinds of cracks discussed here must be determined by independent experiments. Generally speaking, 90°-cracking and ply delamination are fractures of the matrix, or the fiber-matrix interface. Data obtained for bulk epoxy and epoxy adhesive [30] under mode-I action range from 90 to 210 J/m^2 for G_{Ic}; and somewhat higher value for $G_{(I,II)c}$ under mixed-mode actions. In a comprehensive experimental correlation using a T300/934 graphite-epoxy system, Law [31] found $G_{Ic} \sim 230$ J/m^2, and a somewhat lower value for mixed-mode $G_{(I,II)c}$. Recent experiments by Wilkins, et al. [32] and Schapery, et al. [33], have reported that G_{Ic} value can vary depending on the microscopic crack path. For example, Fig. 51 illustrates two situations where the crack opening is in mode-I, but the

microscopic crack-path in the two cases is different. For a graphite-epoxy

system, G_{Ic} value found for cracking path parallel to the fiber direction,

such as shown in Fig. 51(a) ranged from 80~140 J/m^2, while for cracking path

normal to the fibers, shown in Fig. 51(b) ranged from 210~260 J/m^2.

For the cases considered in this report, the 90°-cracking action is

similar to that illustrated by Fig. 51(b); while, the delamination action de-

pends on the specific interface where the crack occurs. In general, a mixed-

mode cracking occurs on off-mid-plane interface, and a mode-I cracking occurs

on the mid-plane interface for symmetric laminates. Lacking the specific data

for specific action, it is assumed, for purpose of illustrating the method

developed herein, that G_c value for all the different modal actions are the

same.* Namely

$$G_c = G_{Ic} = G_{mixed} = 210 \text{ J/m}^2 \qquad (3-20)$$

Finally, the proper value for the (macroscopic) critical flaw size, a_c

must be determined. This value is probably the most ill-defined quantity,

and is difficult to determine physically. In the experimental correlation by

Law [31], a_c for 90°-cracking was found at about 0.25 mm. For delamination,

the value is slightly lower. Thus, in the present study, it is assumed that

a_c is the same for both types of cracking, and its value is given by

$$a_c \sim 0.25 \text{ mm} \qquad (3.21)$$

With the basic material values defined, the numerical correlations with

the experimental results are presented in the next two sub-sections.

---

* Mixed-mode cracking between $\pm 45°$ interface have shown higher values than
  this. But, carefully designed experiments are necessary to accurately
  determine these basic material values.

(a) <u>Laminates under Static Tension</u> Consider the experimental results for the $[\pm 45/0/90_2]_s$ laminates tested under uniaxial tension. Onset of transverse cracking occurred at 131 MPa, and onset of free-edge delamination occurred at 262 MPa. Using the basic material properties for the material ply given in (3-18), the finite element routine calculation for the energy release rate coefficient functions are first obtained for the 90°-cracking simulation. These coefficient functions are displayed in Fig. 52. It is seen that the three coefficient functions are all similar in form; all have a maximum at about $a_m = 1.7\,t$, which is about 85% of the 90_2-layer.

It was assumed earlier that the macroscopic critical flaw size is about $a_c \sim 0.25$ mm, or $a_c \sim 2t$. But the physical constraint (the thickness of the 90_2 layer) limits the value of a_c. Thus, in order to apply the cracking onset criteria of Eq. (3-17), a_c is replaced by a_m. Hence, the equation governing the onset of 90°-cracking is,

$$[C_e(a_m)\bar{e}_x^{\,2} + C_{eT}(a_m)\bar{e}_x(\Delta T) + C_T(a_m)(\Delta T)^2]t = G_c \qquad (3-22)$$

Using the values of C's from Fig. 52, the value for ΔT from (3-19), the value for G_c from (3-20) and $t = 0.136$ mm, Eq. (3-22) yields the far-field laminate strain at onset of cracking,

$$\bar{e}_x = 3.15 \times 10^{-3}.$$

Using E_x from experiment, $E_x = 43.2$ GPa, the far-field laminate stress at onset of cracking is given by

$$\sigma_x = 136 \text{ MPa}$$

which compares with the average value of 131 MPa obtained from experiment.

As the load increases, more 90°-cracks are induced according to the damage event sequence. Then, at some critical load, onset of delamination occurs. By an edge stress analysis, it is inferred that the most probable delamination sites are the mid-plane interface (90°/90°) and the off-mid-plane interface (0°/90°). Numerical results for the energy release rate coefficients have been generated for both cracking sites. Fig. 53 displays the coefficient functions for the mid-plane delamination (mode-I predominant), while Fig. 54 shows the coefficient functions for the off-mid-plane delamination (mixed mode I and mode III predominant). By comparing these two sets of curves, it is determined that the mid-plane delamination is more energetically dominant. Thus, using the values of the coefficient functions at $a = a_c = 0.25$ mm, and $\Delta T = -155°C$, $G_c = 210$ J/m^2 in Eq. (3-22), the onset of free edge delamination along the mid-plane is obtained at the far-field laminate strain,

$$\bar{e}_x = 7.25 \times 10^{-3}.$$

Then, using the value of E_x of the laminate $E_x \cong 39.6$ GPa, the far field stress at onset of delamination is predicted as,

$$\sigma_x = 289 \text{ MPa}.$$

The predicted value is about 10% higher than the experimental value (262 MPa). The reason for the discrepancy is probably due to the effect of the transverse cracking on delamination. The interaction of the transverse cracking and delamination is not accounted for in the predictive model.

In the experiment, laminates $[0_2/90_2/45_2/-45_2]_s$ and $[90_2/0_2/-45_2/45_2]_s$ both showed transverse cracking before delamination. A numerical simulation of transverse cracking for both laminates has been conducted.

40

Fig. 55 shows the computed energy release rate coefficient functions for the $[0_2/90_2/45_2/-45_2]_s$ laminates, while Fig. 56 shows the same for the $[90_2/0_2/-45_2/45_2]_s$ laminates. It is seen that the available energy release rate for the latter is much larger than the former, because in the former, the 90°-layer is constrained on both sides. This added constraint delays the onset and the growth of the transverse cracking. Using the same model as before, the calculated onset stress for $[0_2/90_2/45_2/-45_2]_s$ is

$$\sigma_x = 407 \text{ MPa}.$$

This value, however, is much higher than the measured onset stress of 255 MPa at the first transverse crack. A closer examination of the x-radiograph taken for this series of laminates (3 replicas) shows that significant number of transverse cracks occurred after the load reached 344 MPa. On the other hand, the predicted onset stress for the $[90_2/0_2/-45_2/45_2]_s$ laminate is

$$\sigma_x = 288 \text{ MPa}$$

which is about 20% higher than the measured onset stress of 234 MPa.

Finally, the predicted delamination for $[0_2/90_2/45_2/-45_2]$ occurs at the 45/-45 interface, and for $[90_2/0_2/-45_2/45_2]_s$ occurs at the 0/90 interface; the predicted onset stresses falls within 10% of the measured values.

(b) <u>Laminates under Static Compression</u>   Consider the laminates $[0_2/90_2/45_2-45_2]_s$ and $[90_2/0_2/-45_2/45_2]_s$ for which experimental results on delamination under compression are available, see Table 6. Onset stress is found to be 339.2 MPa, for the former and 316 MPa for the latter. Calculations using the finite element routine yielded the energy release rate coefficient functions for these laminates.   In both cases, the most energetically probable

delamination site is along the +45/-45 interface, resulting in mixed mode cracking. The coefficient functions corresponding to the predicted delamination sites are displayed in Figs. 57 and 58 respectively. Using the values of $a = a_c = 0.25$ mm and $\Delta T = -155°C$, $G_c = 210$ J/m^2 and $t = 2x$ (ply thickness), the predicted far field strains for $[0_2/90_2/45_2/-45_2]_s$ at onset of delamination is

$$\bar{e}_x = 5.01 \times 10^{-3}$$

and for $[90_2/0_2/45_2/-45_2]_s$ is

$$\bar{e}_x = 4.65 \times 10^{-3}.$$

These values translate to $\sigma_x = 272$ MPa and $\sigma_x = 240$ MPa respectively. It is noted that the experimental values for the former is 339 MPa, and for the latter 316 MPa. Thus, the predicted onset of edge delamination under compression is about 20% too low. The reason for the rather poor correlation is thought to be that the compression specimen had a clear test section length of less than 2 cm, so the relatively rigid end-tabs exert a constraining force normal to the specimen, which in turn may suppress the onset and the growth of delamination.

In the case of the dispersed laminates $[0/90/0/90/45/-45/45/-45]_s$, a 45°/-45° interface delamination simulation would yield the energy release rate coefficient functions identical to those shown in Fig. 57, except that $t =$ one ply thickness, instead of 2 ply thickness as indicated in the figure. In this case, the maximum available energy release rate occurs at $a_m = t$, which is less than the critical flaw size a_c. Hence, in predicting the onset of delamination, the values of the coefficient functions are taken at a_m, not a_c. The predicted onset strain is then,

$$\bar{e}_x = 8.18 \times 10^{-3}$$

or, the onset stress,

$$\sigma_x = 410 \text{ MPa}.$$

The corresponding experimental value was 380 MPa, and the final failure was at 425 MPa. Note that at the onset of delamination the specimen is already near total failure. It is not clear whether delamination or buckling action is the cause of final failure.

In view of the foregoing comparisons between the predicted and the experimental loads for the various cracking events, it is clear that the energy method as outlined here appears to be an acceptable analytical tool for describing these cracking events. There are, clearly, some uncertainties with respect to the variable material properties. The other limitation in the method remains the computer routine itself. The finite element formulation is essentially two-dimensional, but most of the cracking events observed in the tests have been three-dimensional in nature, except a few simple cases, such as 90°-cracks and mid-plane delamination in long specimens under uniaxial tension. This limitation precludes a prediction for those specimens with implanted defects. However, this limitation is a numerical short-coming; it does not pertain to the physical method of the energy release rate. It is conceivable that a three-dimensional, or some quasi-3-dimensional finite element routine may readily be developed to handle those cracks which are three-dimensional in nature.

IV. FATIGUE GROWTH MODEL BASED ON ENERGY

The fracture strain energy release rate models developed in the preceding section were shown to be capable of predicting reasonably well the initiation loads for multiple transverse cracking and free edge delamination. Owing to the 2-dimensional nature of the finite element crack growth representation, a satisfactory correlation between experiment and prediction for any 3-dimensional delamination cracking still remains unavailable. However, the energy model does provide a qualitative means for identifying the dominant cracking modes, and their dependence on the fracture energy release rate during the course of the 3-dimensional crack growth.

In this section, an effort is made to extend the concept of fracture energy release rate to describe the crack growth process for laminates under fatigue loads. Special emphasis will be placed on delamination growth under constant amplitude fatigue. An empirical delamination growth model is developed from the experimental data that was generated in early tests. The model is shown to apply well for the tension/tension fatigue case. For the compression/compression fatigue case, the cracking is 3-dimensional; and the model gives only a qualitative description.

A concept of constant damage state is introduced; and by an extension of this concept, a tentative cumulative damage model is presented. Details in these developments are described in the following sub-sections.

1. A Fatigue Growth Model Based on Energy Release Rate

For laminates undergoing free edge delamination under statically applied load, a typical (calculated) energy release rate curve, G(a), is shown in Fig. 50. When the laminate is subjected to a constant amplitude fatigue load,

say σ_f, the maximum available instantaneous energy release rate $G_f(a,\sigma_f)$ is shown in Fig. 59. Assume that σ_f is generally lower than the static onset load for delamination; then the laminate will not suffer any delamination during the first cycle of fatigue life. It is said that the laminate possesses a "reserved" toughness against delamination; and this "reserved" toughness will diminish with increased fatigue load σ_f, or increased fatigue cycles N.

Let G_c be the material critical strain energy release rate against delamination, as has been defined in the static fracture case. Then, the quantity

$$\Delta G = G_c - G_f(a,\sigma_f) \qquad (4.1)$$

represents the "reserved" energy release rate of the laminate against delamination under the fatigue load σ_f.

It is further postulated that growth of delamination under σ_f is described by

$$a = F(\Delta G, N). \qquad (4.2)$$

Or, the increment of delamination Δa per increment of fatigue cycle is described by the relation,

$$\frac{\Delta a}{\Delta N} \sim (\Delta G)^{-N} \qquad (4.3)$$

The choice of (4.3) is based on the observation that, under a small fatigue load σ_f, growth of delamination is slow. From (4.1) it is seen that for small σ_f, $\Delta G \sim G_c$; hence the left-hand of (4.3) decreases rapidly with N. On the other hand, when σ_f is large, or σ_f approaches the static onset load of delamination then $\Delta G \sim 0$; and the growth of delamination increases rapidly with N.

The exact form of (4.3) must be determined from experimental data.

Consider the case of free edge delamination growth in the $[\pm 45/0/90_2]_s$ laminates under tension fatigue. The averaged experimental measurements of delamination are plotted against log N in Fig. 22, for various fatigue load levels. Using the data in this figure, a plot of $\log(\Delta \bar{a}/\Delta N)$ versus $\log(N)$ is obtained for each of the fatigue loads. These plots are shown in Fig. 60. Here

$$\bar{a} = (a/b) \, 100\% \qquad (4.4)$$

where b is the width of the specimen. Note that $\bar{a}$ also represents the "percentage delamination."

It is seen from Fig. 60 that for all fatigue load levels $\log(\Delta \bar{a}/\Delta N)$ maintains a linear relation with $\log(N)$. Then, the following empirical form is suggested:

$$\frac{\Delta \bar{a}}{\Delta N} = \alpha [k \, \Delta \bar{G}]^{-\beta} \, \log N \qquad (4.5)$$

where $\Delta \bar{G}$ is defined as the "percentage energy reserve,"

$$\Delta \bar{G} = (G_c - G_f)/G_c. \qquad (4.6)$$

With (4.5) and (4.6), one obtains the delamination growth relation

$$a(N) = b \int_{N_0=1}^{N} \alpha [k \, \Delta \bar{G}]^{-\beta} \, \log N \, dN \qquad (4.7)$$

Strictly speaking, $\Delta \bar{G}$ is a complicated function; $\Delta \bar{G} = \Delta \bar{G}(G_c, a, \sigma_f)$ for $0 < a < b$. Thus, (4.7) is also a complex integral. Onset of delamination is defined when $a(N_c) \rightarrow a_c$.

For approximation, one may consider $a \gg a_c$ and define

$$G_f = G_f(a_m, \sigma_f) \qquad (4.8)$$

where a_m is the size of a at which G_f attains the maximum value, see Fig. 59.

Then $\Delta \bar{G}$ becomes a constant and an integration of (4.7) from N_m to N yields

$$a(N) = b \ \alpha [N(k \ \Delta\bar{G})^{-\beta \ \log N} - \gamma]/[1 - \beta \log(k \ \Delta\bar{G})] \qquad (4.9)$$

The constants α, β, and k are determined from experimental data, while γ is determined by $a(N_m) \rightarrow a_m$. It is noted that the applied load σ_f and the structural geometry and their interaction with the ply stacking sequence are implicit in $\Delta\bar{G}$. Hence, the constants α, β and k should be primarily material property dominated. From the data reduction plots in Fig. 60, these three constants are determined as

$$\alpha = 0.25; \quad \beta = 0.806; \quad k = 12.67.$$

and the value of γ is $\gamma = 2.35$.

Using these values in Eq. (4.9), and the G-curves generated for the delamination cracking in the $[\pm 45/0/90_2]_s$ laminates (see Fig. 53) growth curves under various σ_f loads can be calculated according to Eq. (4.9). These are shown along with the experimentally measured curves in Fig. 61. It is seen that the growth model (4.9) describes the experimental data quite well.

Note that it takes only fatigue growth curves at two load levels to determine the values for α, β and k and γ.

Next, consider the experimental data obtained from the compression fatigue tests of the $[0_2/90_2/45_2/-45_2]_s$ laminates. Fig. 29 shows the delamination growth curves for three levels of fatigue loads, at 179 MPa, 221 MPa and 276 MPa. Recall that this series of laminates had no edge delamination until a compressive load of 339 MPa was reached. But the predicted edge delamination onset was only 272 MPa. This discrepancy was attributed to the pinning effect of the

end-tabs of the test specimen, which resulted in 3-dimensional crack growth.

The finite element solution for the available energy release rate G(a) however

was about 50% too high, because of the 2-dimensional plane strain formulation.

Thus, if the calculated $G_f(a_m, \sigma_f)$ is reduced by 50%, and using $G_c = 210$ J/m^2,

Eq. (4.6) gives the values of $\Delta \bar{G}$ as 0.8, 0.572 and 0.451, respectively, for

$\sigma_f = 179$ MPa, 221 MPa and 276 MPa.

Assume that the delamination model under compression fatigue is also

given by Eq. (4.5). Data reduction for this case is displayed in Fig. 62. It

is seen that the test data generally follow a straight line in the log($\Delta \bar{a}/\Delta N$)

vs. log(N) plane. The constants in Eq. (4.9) are determined as

$$\alpha = 0.4; \quad \beta = 0.51; \quad k = 35.9; \quad \gamma = 4.$$

These values are slightly different from those obtained for tension fatigue;

under compression, the rate of growth is faster than that under tension. The

predicted delamination growth by Eq. (4.9) does not compare as well with the

experiment, although it does provide the general trend, see Fig. 63. The

discrepancy is believed due to the inaccuracy in the G(a) calculation by the

2-D finite element.

2.   The Concept of Constant Damage States

From the preceding discussions on delamination growth under both static

and fatigue loads, it appears that a generally deterministic relationship may

be found between the applied load and the state of damage. In the event of

fatigue cycling, this relationship varies smoothly with N. Fig. 64 illustrates

the concept of constant damage. The vertical coordinate of Fig. 64 represents

the static loading. When the applied load reaches σ_c, onset of delamination

occurs. This state of damage can be independently produced by a fatigue load,

say at $\sigma_1 < \sigma_c$. Then under σ_1, it takes N_1 cycles to induce onset of delamination. Similarly, the same state of damage can also be reached by a different fatigue load, say σ_2, by N_2 cycles. Points defining the same damage state in the σ_f-log(N) plane define a "constant" damage curve. In Fig. 64, a curve representing 20% delamination and a curve representing 100% delamination are depicted. Clearly, the 100%-curve corresponds to the final failure of the laminate; and it is the same curve as the commonly generated fatigue S-N curve.

The constant damage curves can be constructed using experimental data. For example, Fig. 65 displays the constant damage curves generated by tension fatigue for the $[\pm45/0/90_2]_s$ laminates. It is seen that the various damage states (transverse cracking, delamination, etc.) maintains a definite occurrence sequence under both static and fatigue loadings. The shape of the curves depicts the trend of fatigue degradation.

Figs. 66 and 67 show the constant damage curves in terms of % delamination for $[0_2/90_2/45_2/-45_2]_s$ and $[0/90/0/90/45/-45/45/-45]_s$-A laminates, respectively. These laminates were tested under compression fatigue; it is seen that the rate of fatigue degradation is much larger than that under tension (see Fig. 65).

From these constant damage curves, the growth of damage under some spectrum fatigue loads may be evaluated. As has been demonstrated in the preceding sub-section, a deterministic damage growth model based on energy release rate may be formulated, such as proposed by Eq. (4.9). If such a model correctly describes the damage growth processes in the laminate, it can calculate the constant damage curves in the load-life plane without the necessity of experiment. The constant damage curves provide the essential step in the formulation of a cumulative damage model under spectrum fatigue loading.

3. A Cumulative Fatigue Damage Model

Upon the construction of the constant damage curves in the load (σ_f)-life (N) plane, cumulative damage in the laminate under a given load spectrum may be evaluated in a manner similar to the well known Miner's rule. Consider, as an example, the load history shown in Fig. 68(a). When it is applied to a given laminate, the state of damage at the end of the period of constant amplitude loading σ_1 is represented by point A in the load-life plane. The constant damage curve passing point A is denoted as curve a_1 (say e.g., the onset of delamination). At the end of N_1-cycle, the fatigue load σ_f is raised to σ_2. Then the state of damage in the laminate at N_1 moves from point A to point B along curve a_1. Under σ_2 and for a period of $(N_2 - N_1)$ cycles, the damage state in the laminate is represented by point C; through C passes the constant damage curve a_2. Clearly, the damage state represented by curve a_2 is more extensive than the damage state represented by curve a_1. At the end of the N_2-cycle, the fatigue load is lowered to σ_1 again; and the corresponding damage state moves from point C to point D along the constant damage curve a_2. Finally, at the completion of the loading history at N_3, the damage state moves from D to E, where the damage is represented by curve a_3. Extension from E toward the failure envelop intersects the S-N curve at point F. $\overline{EF}$ gives the residual life of the laminate after it has been subjected to the prescribed spectrum loading shown by Fig. 68(a).

The foregoing cumulative damage representation depends on the ability to accurately construct the constant damage curves, either experimentally or

Numerically. In the case of delamination, both aspects have been discussed

in this study. The suggested cumulative model, however, remains to be tested

against experiments. In view of the understanding gained in this study, the

method appears quite promising.

V. CONCLUDING REMARKS

In this report, the fracture growth mechanisms of delamination in fiber
reinforced composite laminates have been studied. Experiments on various
types of delamination growth have been conducted in order to observe and
identify the dominant loading, geometry and material parameters which influ-
ence the growth processes of delamination. Predictive models based on the
linear elastic fracture mechanics concept of strain energy release rate are
then developed to describe the various delamination processes. The energy
method has been shown to apply, with varying degree of accuracy, to delamination
cracking in laminates made of a graphite-epoxy composite system.

From the numerous results obtained in the present study, an assessment of
our understanding and ability to model the complex process of delamination
is attempted here. The following remarks are in order:

1. Delamination stems from material property mismatch between two layers.

    Under load, each layer of the laminate would deform differently if

    allowed to delaminate. Bonds between layers prevent this from happening.

    The bonding strength is derived primarily from the matrix phase which

    is a material property inherent to the composite system. The driving force

    for delamination derives from the available strain energy release in the

    course of delamination growth. The available energy near a delamination

    crack, however, is a very complicated function of loading, layering

    structural geometry and the overall geometry of the laminate. The most

    striking factor in the available energy release is the actual thickness

    of the material layer adjacent to the delamination cracking. This is re-

    ferred to as the "thickness effect" discussed in this study. The thickness

    effect is significant both in static strength and in fatigue life of the

laminates. Accordingly, the effect must be considered in laminate design.

2. For all the delamination cases studied, except one, the delamination growth front is a 2-dimensional contour and the stress field near the contour cracking front is 3-dimensional. The exception is the long symmetric laminate under tension, whose straight free edge undergoes delamination because of interlaminar edge stresses. In this case, a 2-dimensional generalized plane strain approximation is quite appropriate. Consequently, the 2-dimensional finite element modeling of free edge delamination growth yielded exceptionally good results when compared to experiment. All other cases, however, require 3-dimensional modeling, which so far is not available. Nevertheless, qualitative analysis based on the same energy release method showed correct trend without contradiction. Thus, the growth of delamination with 2-dimensional contour front can be analyzed by the energy method, but the quantitative prediction must wait for the successful development of a 3-dimensional, or a quasi-3-dimensional numerical routine.

3. The energy release rate method provides a one-to-one load-damage (delamination) relationship. It is a deterministic relationship based on the mechanisms of crack growth. Extension of this model to the growth process under constant amplitude fatigue loading is made possible by the concept of constant damage curves. Although fatigue experiments conducted in this study have been limited in scope, the results obtained indicate the validity of the constant damage concept. Analytical construction of the constant damage curves in the load-life plane is also possible if the damage itself can be successfully modeled (e.g., 2-dimensional vs. 3-dimensional model at the present state of the art).

The concept of constant damage may be readily applicable in a
cumulative damage model for fatigue under spectrum loading. All
this points to a promising direction toward a deeper understanding of
failure in laminates.

It is noted that there are several other areas basic to the understand-
ing of the delamination mechanics, that are left unexplored. One of which
is the determination of the material critical energy release rate G_c. It is
conceivable that this property, when measured at the macroscopic scale, will
exhibit a considerable scatter. Compared to the extensive experiments on
the ultimate strength of composite, studies on the property G_c have been rela-
tively few.

Another area that needs more comprehensive examination is the fracture
growth criterion under a mixed-mode cracking action at the macro-scale. It
is apparent in the experiments that mode-I and mixed-mode fracture surfaces
exhibit different characteristics. Energy required to separate the two dif-
ferent surfaces may be also different, thus requiring a different set of crack
growth criteria.

Finally, a concentrated effort should be made in developing a 3-dimen-
sional numerical routine which is capable of modeling the delamination growth,
similar to the 2-dimensional model employed in this study. Such a 3-dimen-
sional routine is essential to describe most other delamination cracks which
are 3-dimensional in nature.

REFERENCES

[1] N.J. Pagano and R.B. Pipes, "The Influence of Stacking Sequence on Laminate Strength," J. Composite Materials, Vol. 5, (1971) p. 50.

[2] K.L. Reifsnider, E.G. Henneke and W.W. Stinchcomb, "Delamination of Quasi-isotropic Graphite-Epoxy Laminates," Composite Materials: Testing and Design. ASTM STP 617 (1977) p. 93.

[3] G.P. Sendeckyj and H.D. Stalnaker, "Effect of Time at Load on Fatigue Response of $[0/\pm45/90]_{2s}$ T300/5208 Graphite-Epoxy Laminate," Composite Materials: Testing and Design. ASTM STP 617 (1977) p. 39.

[4] J.G. Bjeletich, F.W. Crossman and W.J. Warren, "The Influence of Stacking Sequence on Failure Modes in Quasi-isotropic Graphite-Epoxy Laminates," Failure Modes in Composites - IV, AIME (1978).

[5] J.M. Whitney and R.Y. Kim, "Effect of Stacking Sequence on the Notched Strength of Laminated Composites," Composite Materials: Testing and Design. ASTM STP 617 (1977) p. 229.

[6] M.S. Rosenfeld and S.L. Huang, "Fatigue Characteristics of Graphite-Epoxy Laminates under Compressive Loading," J. Aircraft, Vol. 15 (1978) p. 264.

[7] A.H. Puppo and H.A. Evensen, "Interlaminar Shear in Laminated Composites under Generalized Stress," J. Composite Materials, Vol. 4, (1970) p. 204.

[8] R.B. Pipes and N.J. Pagano, "Interlaminar stresses in Composite Laminates under Uniform Axial Tension," J. Composite Materials, Vol. 4, 1970 p. 538.

[9] G. Isakson and A. Levy, "Finite Element Analysis of Interlaminar Shear in Fibrous Composites," J. Composite Materials, Vol. 5, (1971) p. 273.

[10] E.F. Rybicki, "Approximate Three-Dimensional Solutions for Symmetric Laminates under In-plane Loading," J. Composite Materials, Vol. 5, (1971) p. 354.

[11] N.J. Pagano, "On the Calculation of Interlaminar Normal Stress in Composite Laminates," J. Composite Materials, Vol. 8 (1974) p. 89.

[12] S. Tang, "Interlaminar Stresses of Uniformly Loaded Rectangular Composite Plate," J. Composite Materials, Vol. 10, (1976) p. 69.

[13] P.W. Hsu and C.T. Herakovich, "A Perturbation Solution for Interlaminar Stresses in Composite Laminates," Composite Materials: Testing and Design, ASTM STP 617 (1977) p. 296.

[14] A.S.D. Wang and F.W. Crossman, "Some New Results on Edge Effect in Symmetric Composite Laminates," J. Composite Materials, Vol. 11, (1977) p. 92.

[15] P.W. Hsu and C.T. Herakovich, "Edge Effects in Angle-ply Composite Laminates," J. Composite Materials, Vol. 11 (1977) p. 422.

[16] A.S.D. Wang and F.W. Crossman, "Edge Effects on Thermally Induced Stresses in Composite Laminates," J. Composite Materials, Vol. 11, (1977) p. 300.

[17] F.W. Crossman and A.S.D. Wang, "Stress Field Induced by Transient Moisture Sorption in Finite Width Composite Laminates," J. Composite Materials Vol. 12, (1978) p. 2.

[18] A.S.D. Wang and F.W. Crossman, "Calculation of Edge Stresses in Multi-layer Laminates by Sub-structuring," J. Composite Materials, Vol. 12, (1978) p. 76.

[19] R.L. Spilker and S.C. Chou, "Edge Effects in Summetric Composite Laminates: Importance of Satisfying the Traction-Free-Edge Condition," J. Composite Materials, Vol. 14, (1980) p. 2.

[20] A.S.D. Wang and F.W. Crossman, "Initiation and Growth of Transverse Cracks and Edge Delamination in Composite Laminates, Part 1, An Energy Method," J. Composite Materials, Vol. 14, (1980) pp. 71-87.

[21] F.W. Crossman, W.J. Warren, A.S.D. Wang and G.E. Law, "Initiation and Growth of Transverse Cracks and Edge Delamination in Composite Laminates, Part 2, Experimental Correlation," J. Composite Materials, Vol. 14, (1980) pp. 88-106.

[22] A.S.D. Wang, "Growth Mechanisms of Transverse Cracks and Ply Delamination in Composite Laminates," Advances in Composite Materials, ICCM-III, Paris (1980) pp. 170-182.

[23] F.W. Crossman and A.S.D. Wang, "The Dependence of Transverse Cracking and Delamination on Ply Thickness in Graphite-Epoxy Laminates," Damages in Composite Materials, ASTM STP (in press).

[24] A.S. Tetelman and A.J. McEvily, Jr., "Fracture of Structural Materials," John Wiley and Sons, New York (1967).

[25] G.R. Irwin, "Fracture" Handbuch der Physik, Vol. 6, (1958) p. 551.

[26] E.F. Rybicki, and M.E. Kanninen, "A Finite Element Calculation of Stress Intensity Factors by a Modified Crack Closure Integral," Engr. Fracture Mechanics, Vol. 9, (1977) p. 931.

[27] E.F. Rybicki, D.W. Schmueser and J. Fox, "An Energy Release Rate Approach for Stable Crack Growth in the Free Edge Delamination Problem," J. Composite Materials, Vol. 11, (1977) p. 470.

[28] K.L. Reifsnider, W.W. Stinchcomb and E.G. Henneke, "Defect-Property Relationships in Composite Materials," AFML-TR-76-81, Part 1 (1976), Part 2 (1977) and Part 3 (1979).

[29] A.S. Griffith, "The Phenomenon of Rupture and Flow in Solids," Phil. Trans. Roy. Society, London. Series A-221 (1920) p. 163.

[30] W.D. Bascom, R.L. Cottington and C.O. Timmons, "Fracture Design Criteria for Structural Adhesive Bonding - Promise and Problems," Naval Engr. Journal, Aug. (1976) p. 73.

[31] G. E. Law, Jr., "Fracture Analysis of $(\pm 25/90_n)_s$ Graphite-Epoxy Laminates," Ph.D. Thesis, Drexel University, (1981).

[32] D.J. Wilkins, J.R. Eisenmann, R.A. Carmin, W.S. Margolis and R.A. Benson, "Characterizing Delamination Growth in Graphite-Epoxy," Damages in Composite Materials, ASTM STP (1981) (to appear).

[33] R.A. Schapery, "Composite Materials for Structural Design," Mechanics of Composite Review, (1980) p. 4.

Table 1. Basic Property Characterization Tests

Type of test	Type of laminate	# of specimens
Static Tension	$[0_{12}]$	2
	$[90_{12}]$	3
	$[0_2/90_2/45_2/-45_2]_s$	2
	$[90_2/0_2/-45_2/45_2]_s$	1
	$[0/90/0/90/45/-45/45/-45]_s$	1
	$[90/0/90/0/-45/45/-45/45]_s$	1
	$[45/-45/0/90_2]_s$	3
	$[-45/45/90/0_2]_s$	1
	$[\pm45]_{2s}$	3
Static Compression	$[0_{12}]$	3
	$[0_2/90_2/45_2/-45_2]_s$	1
	$[90_2/0_2/-45_2/45_2]_s$	4
	$[0/90/0/90/45/-45/45/-45]_s$	2
	$[45/-45/0/90_2]_s$	1
	$[\pm45]_{2s}$	3

Table 2. <u>Damage Growth Tests under Static Step-Loading</u>

Type of test	Type of laminate	# of specimens
Tension step-load	$[0_2/90_2/45_2/-45_2]_s$	3
	$[90_2/0_2/-45_2/45_2]_s$	3
	$[0/90/0/90/45/-45/45/-45]_s$	3
	$[90/0/90/0/-45/45/-45/45]_s$	3
	$[45/-45/0/90_2]_s$	5
	$[-45/45/90/0_2]_s$	3
	$[45/-45/0/90_2]_s - A*$	2
	$[45/-45/0/90_2]_s - B*$	2
Compression step-load	$[0_{12}]$	1
	$[0_2/90_2/45_2/-45_2]_s$	3
	$[90_2/0_2/-45_2/45_2]_s$	3
	$[0_2/90_2/45_2/-45_2]_s - A*$	2
	$[0_2/90_2/45_2/-45_2]_s - C*$	2
	$[0/90/0/90/45/-45/45/-45]_s$	2
	$[0/90/0/90/45/-45/45/-45]_s - A*$	2
	$[0/90/0/90/45/-45/45/-45]_s - C*$	2
	$[45/-45/0/90_2]_s$	2

* A - Specimens with implanted 1/4" Teflon strip, see Fig. 2.

B - Specimens with implanted 1/2" Teflon strip, see Fig. 2

C - Specimens with implanted 1/4" diameter Teflon circle, see Fig.3.

Table 3. Damage Growth Tests under Fatigue Loading

Type of test	Type of laminate	# of specimens	# of load levels
Tension Fatigue	$[45/-45/0/90_2]_s$	9	5
	$[45/-45/0/90_2]_s - A*$	7	3
	$[45/-45/0/90_2]_s - B*$	7	3
Compression Fatigue	$[45/-45/0/90_2]_s$	2	2
	$[0_2/90_2/45_2/-45_2]_s$	6	3
	$[0_2/90_2/45_2/-45_2]_s - A*$	5	3
	$[0_2/90_2/45_2/-45_2]_s \quad C*$	4	2
	$[90_2/0_2/-45_2/45_2]_s$	5	3
	$[0/90/0/90/45/-45/45/-45]_s$	2	2
	$[0/90/0/90/45/-45/45/-45]_s - A*$	5	3
	$[0/90/0/90/45/-45/45/-45]_s - C*$	4	2

A - Specimens with implanted 1/4" Teflon strip

B - Specimens with implanted 1/2" Teflon strip

C - Specimens with implanted 1/4" diameter Teflon circle

Table 4.   Summary of Results from Basic Property Tests

Static Tension

laminate lay up	avg σ_{ult} [MPa]	E_x [GPa]	ν_{xy}	Remarks
$[0_{12}]$	1325.2*	139.83	0.291	*σ_{max} without failure
$[90_{12}]$	60.0	11.03	0.027	
$[0_2/90_2/45_2/-45_2]_s$	524.0	50.13	0.283	
$[90_2/0_2/-45_2/45_2]_s$	453.0	51.38	0.309	
$[0/90/0/90/45/-45/45/-45]_s$	659.2	51.99	0.325	
$[90/0/90/0/-45/45/-45/45]_s$	673.6	52.26	0.304	
$[45/-45/0/90_2]_s$	326.1	39.65	0.172	
$[45/-45/0/90_2]_s$*	430.9	43.23	-	* new batch
$[-45/45/90/0_2]_s$	930.1	73.71	0.317	
$[\pm 45]_{2s}$	156.5	19.10*	0.69	* initial modulus

Static Compression

laminate lay up	avg σ_{ult} [MPa]	E_x [GPa]	ν_{xy}	Remarks
$[0_{12}]$	932.2	136.93	0.277	
$[0_2/90_2/45_2/-45_2]_s$	388.2	60.33	0.248	
$[90_2/0_2/-45_2/45]_s$	346.1	51.23	0.292	
$[0/90/0/90/45/-45/45/-45]_s$	430.9	53.64	0.266	
$[45/-45/0/90_2]_s$	371.6	38.13	0.151	
$[\pm 45]_{2s}$	175.1	17.30*	0.60	* initial modulus

Table 5. Summary of Results from Damage Growth Tests

Static Tension

laminate lay-up	Onset stress, MPa		σ_{ult}, MPa	Remarks
	T.C.	E.D.		
$[0_2/90_2/45_2/-45_2]_s$	255.0	521.2	539.0	+45 cracks dominant from σ = 427 MPa
$[90_2/0_2/-45_2/45_2]_s$	234.4	442.6	541.0	+45 cracks from σ = 379 MPa
				E.D. and +45 cracks dominant from σ = 448
$[90/0/90/0/-45/45/-45/45]_s$	413.6	–	650.8	* not clear
$[0/90/0/90/45/-45/45/-45]_s$	434.3	–	606.7	* local
$[45/-45/0/90_2]_s$	131.0	262.0	393.0	E.D. dominant from σ = 351.6 MPa
$[45/-45/0/90_2]_s$*	131.0	236.5	443.3	* new batch
$[45/-45/0/90_2]_s$ – A*	103.4	179.2	435.7	* new batch implanted 1/4" teflon strip
$[45/-45/0/90_2]_s$ – B*	103.4	172.4	434.3	* new batch implanted 1/2" teflon strip
$[-45/45/90/0_2]_s$	820.4*	–	935.0	* local T.C. on edges

Table 6. <u>Summary of Results from Damage Growth Tests</u>

Static Compression

Laminate lay-up	Onset of E.D. MPa	σ_{ult}, MPa	Remarks
$[0_{12}]$	–	857	No damage before failure
$[0_2/90_2/45_2/-45_2]_s$	339.2	369.5	Local $\pm$45-cracking from $3\overline{4}1$ MPa
$[0_2/90_2/45_2/-45_2]_s$ - A*	131.0	286.0	Local $\pm$45-cracking from $2\overline{4}1.3$ MPa
$[0_2/90_2/45_2/-45_2]_s$ - C*	251.6	330.9	Delamination from edge first
$[90_2/0_2/-45_2/45_2]_s$	315.7	319.2	
$[0/90/0/90/45/-45/45/-45]_s$	379.2*	425.4	* Onset delam. not clear
$[0/90/0/90/45/-45/45/-45]_s$ A	138.0	382.6	$\pm$45-cracking from 310 MPa
$[0/90/0/90/45/-45/45/-45]_s$ C	265.4	365.4	$\pm$45-cracking around circular patch
$[\pm45/0/90_2]_s$	–	382.6	No delamination before failure

Table 7. Summary of Results from Damage Growth Tests

Tension-Tension Fatigue

laminate lay-up	max σ_F MPa	No. of specimens	No. of cycles at onset of		T.C. density at onset of E.D.	No. of cycles tested
			T.C.	E.D.		
$[45/-45/0/90_2]_s$	110.3	1	100		–	2,000,000
σ_{ult} = 443.3 MPa	138.0	1	10	500,000	8.2/cm	1,000,000
	171.0	2	–	7,500	8.4	"
	189.6	2	–	1,000	8.2	"
	205.5	1	–	500	8.2	"
$[45/-45/0/90_2]_s$-A	137.2	2	–	7,500	4.7	600,000
σ_{ult} = 435.8	171.0	3	–	1,000	5.7	500,000
	186.8	2	–	50	3.2	400,000
$[45/-45/0/90_2]_s$-B	138.6	2	–	100	4.4	300,000
σ_{ult} = 434.0	171.7	3	–	20	4.0	500,000
	189.6	2	–	–	2.5	100,000

Table 8. <u>Summary of Results from Damage Growth Tests</u>

Compression-Compression Fatigue

laminate lay-up	Max σ_F MPa	No. of specimens	No. of cycles at onset of E.D.	Max No. of cycles	Remarks
$[0_2/90_2/45_2/-45_2]_s$	182.0	2	150,000	1,000,000	suspended
$\sigma_{ult} = 369.5$	221.3	2	3,000	130,700	failed
	276.5	2	70	16,975	"
$[0_2/90_2/45_2/-45_2]_s$-A	182.7	1	–	257,260	"
$\sigma_{ult} = 286.0$	196.5	2	–	307,000	suspended
	220.6	2	–	73,430	failed
$[0_2/90_2/45_2/-45_2]_s$-C	194.4	2	10,000	500,000	suspended
$\sigma_{ult} = 330.9$	222.0	2	200	94,710	failed
$[0/90/0/90/45/-45/45/-45]_s$	276.5	1	10,000	748,320	"
$\sigma_{ult} = 425.4$	343.4	1	500	3,100	"
$[0/90/0/90/45/-45/45/-45]_s$-A	219.2	1	–	300,000	suspended
$\sigma_{ult} = 382.6$	248.9	2	–	143,870	failed
	276.5	2	–	42,650	"
$[0/90/0/90/45/-45/45/-45]_s$-C	193.7	2	5,000	500,000	suspended
$\sigma_{ult} = 365.4$	219.2	2	300	500,000	"
$[45/-45/0/90_2]_s$	241.3	1	–	100,000	failed
$\sigma_{ult} = 382.6$ MPa	304.7	1	–	860	"
$[90_2/0_2/-45_2/45_2]_s$	180.6	2	190,000	1,000,000	suspended
$\sigma_{ult} = 319.2$	220.6	2	7,000	77,890	failed
	274.4	1	200	10,000	"

Implanted
Interlaminar
Flaw
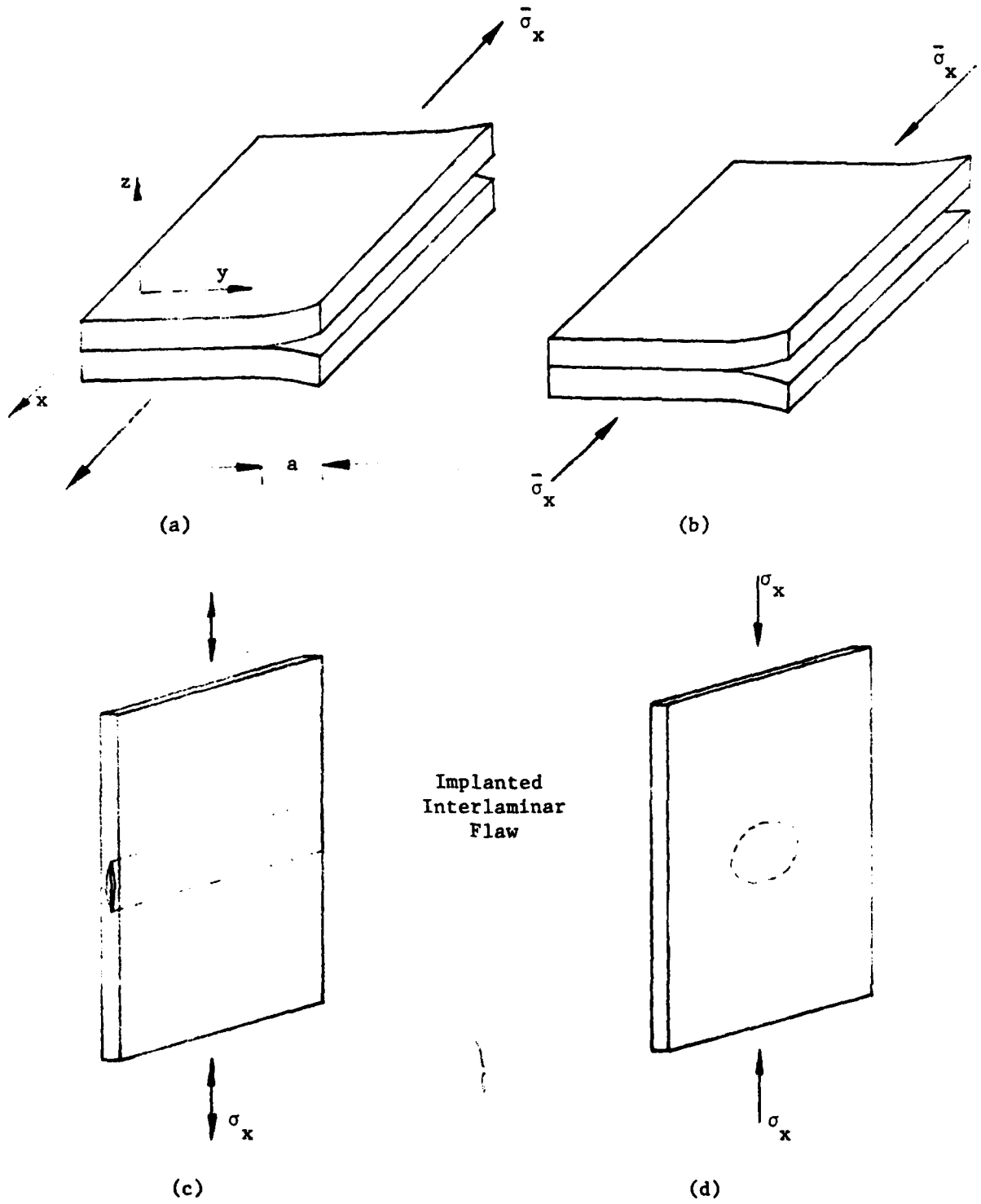
Figure 1. Schematics of Four Delamination Problems Studied

65

19.0 mm

Type "A" and "B" specimens

38.1 mm

6.3 mm Teflon strip (type A)

12.7 mm Teflon strip (type B)

63.5 mm

177.8 mm

38.1 mm

63.5 mm
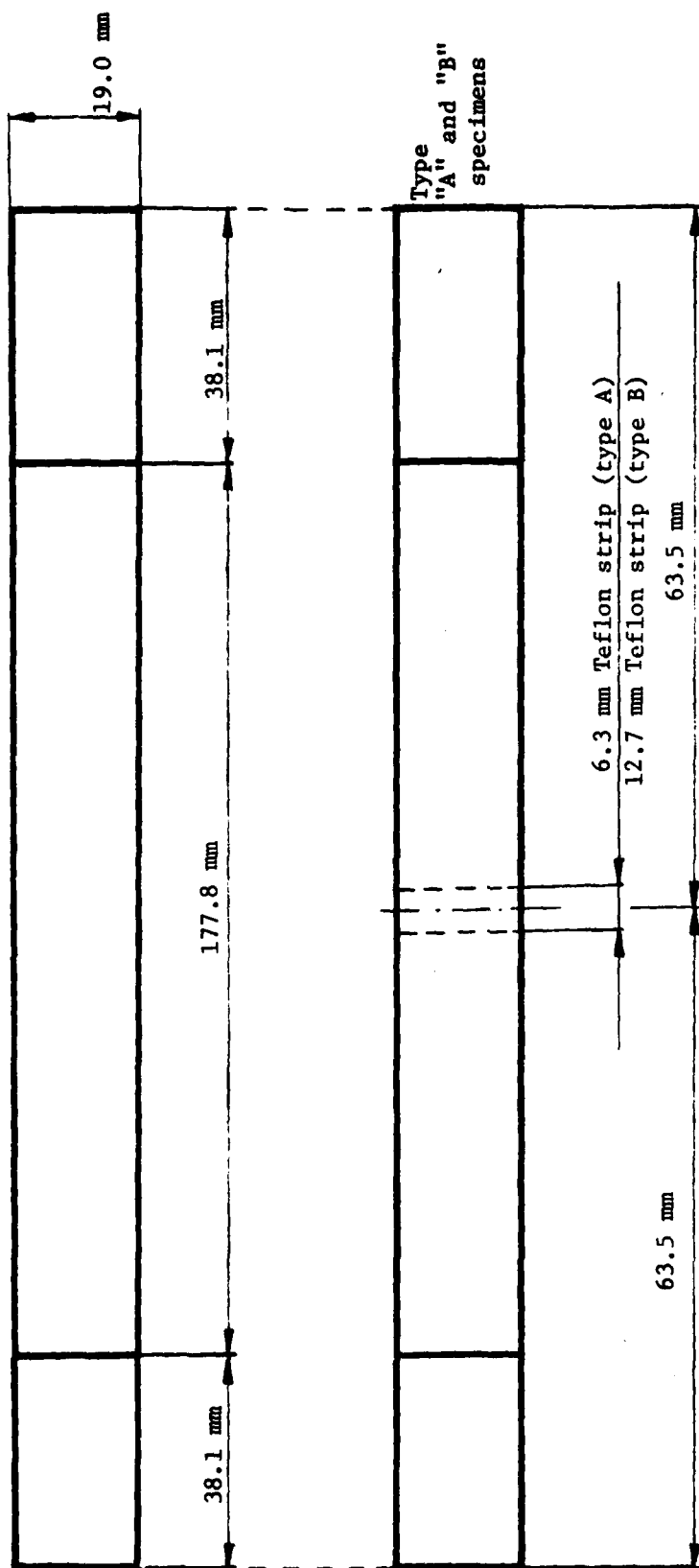
Figure 2. General Configuration of Tensile Test Specimens

25.4 mm

54 mm 19 mm 54 mm

Type "A"
specimens

6.3 mm Teflon strip

Type "C"
specimens

6.3 mm Teflon
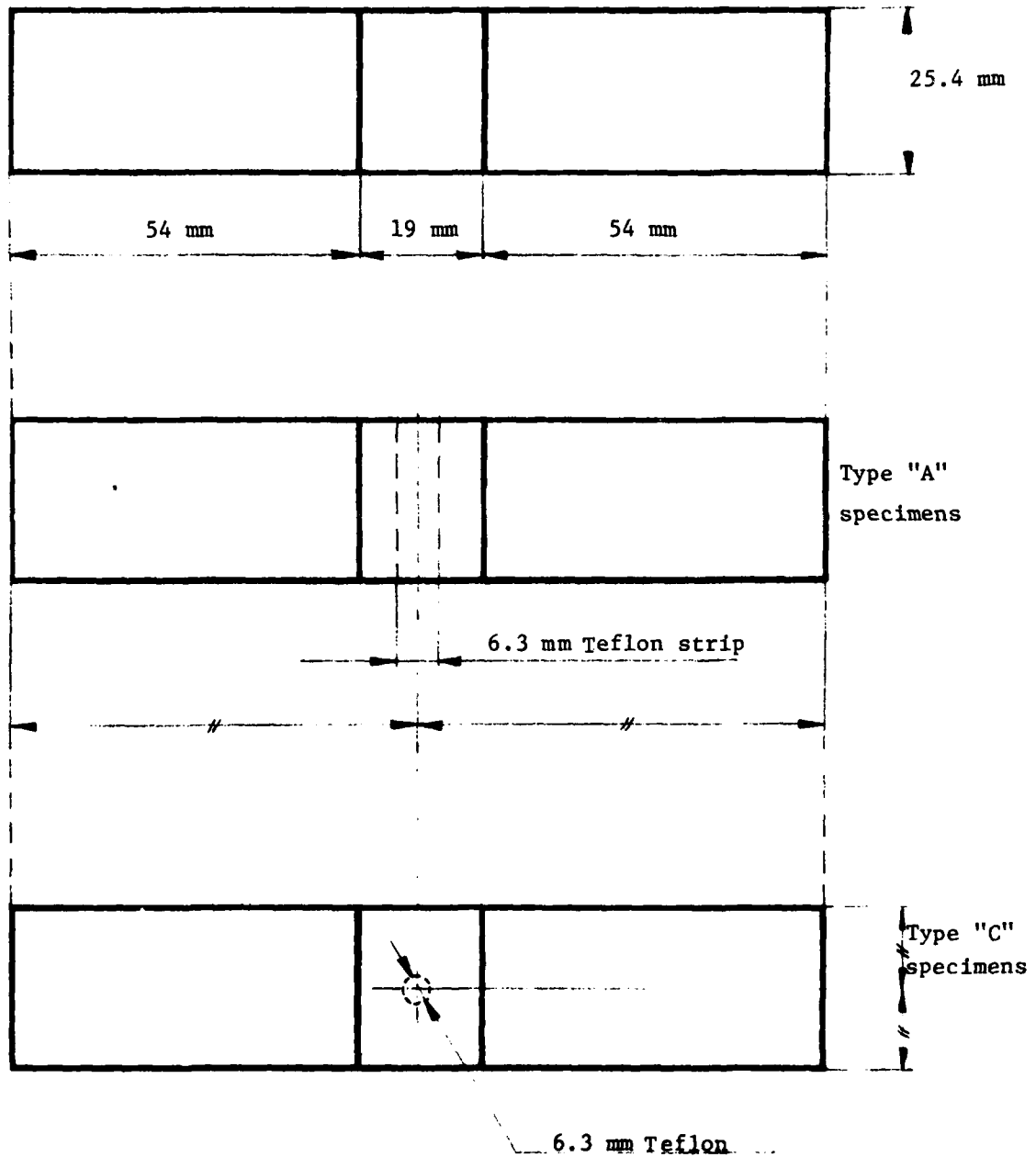
Figure 3. General Configuration of Compression Test Specimens
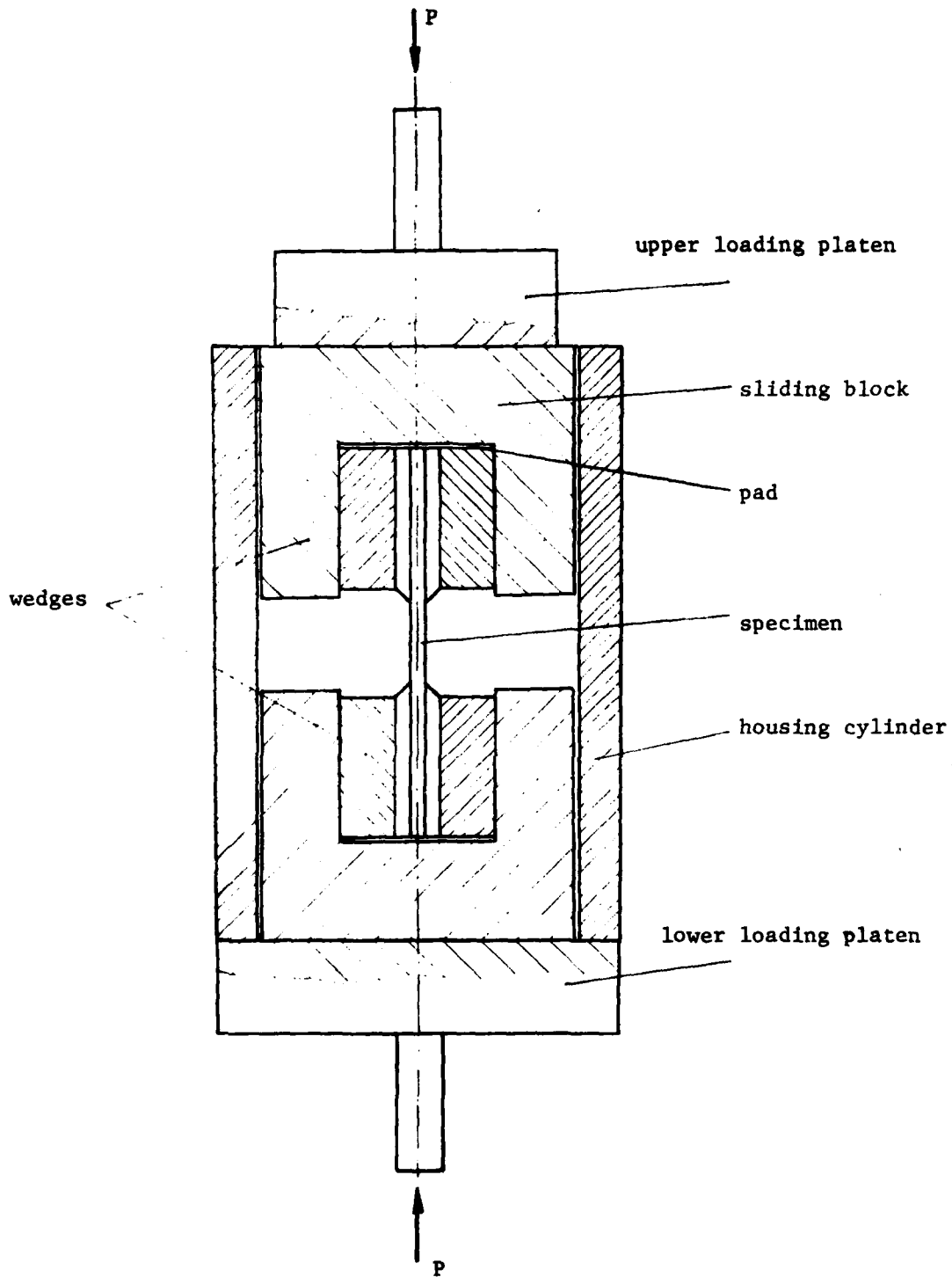
Figure 4. Schematics of the Compression Test Fixture
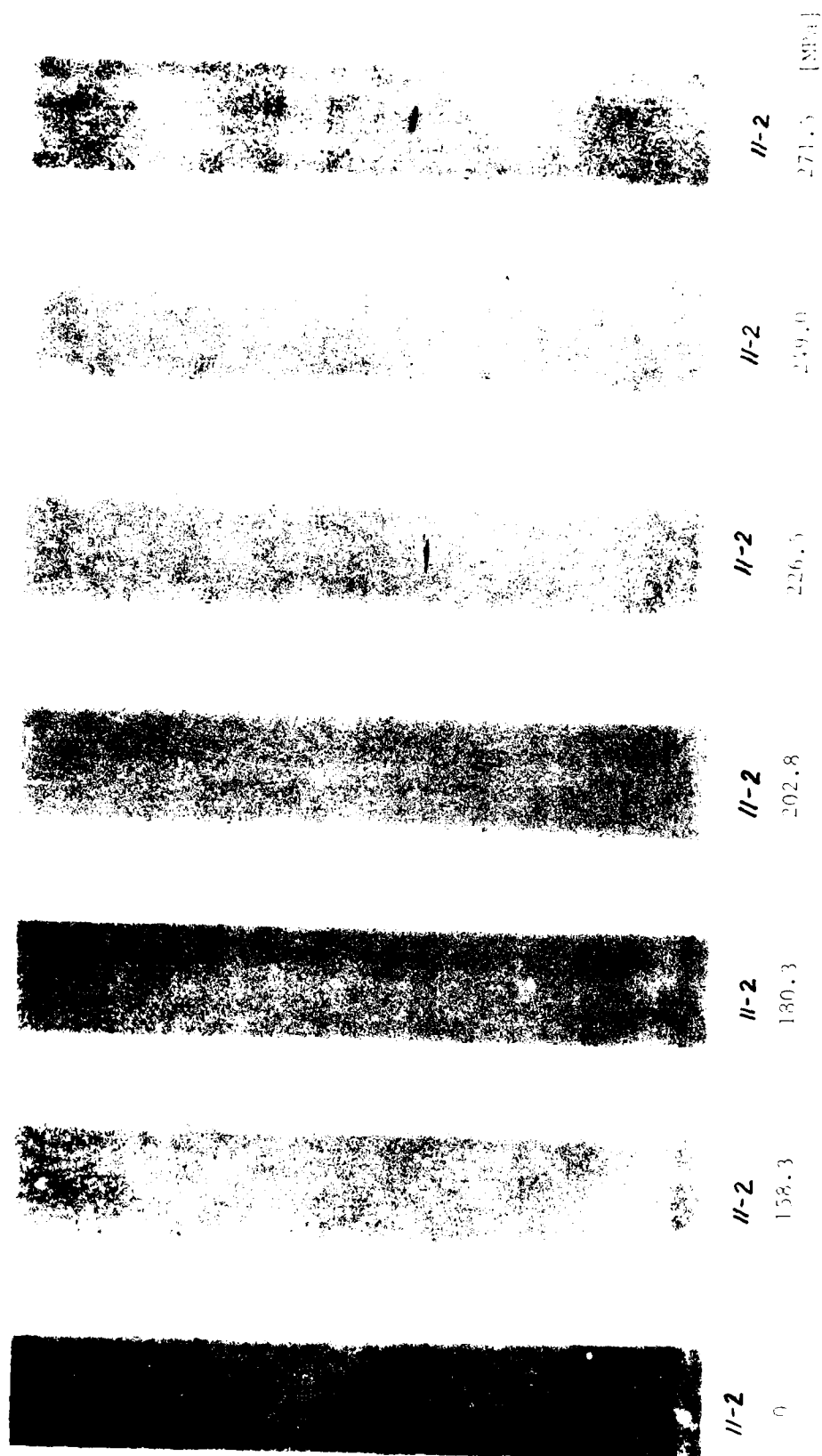
$[O_2/90_2/45_2/-45_2]_s$

Figure 5. Load-sequence x-radiographs for a $[0_2/90_2/+45_2/45_2]_s$ laminate under tension.
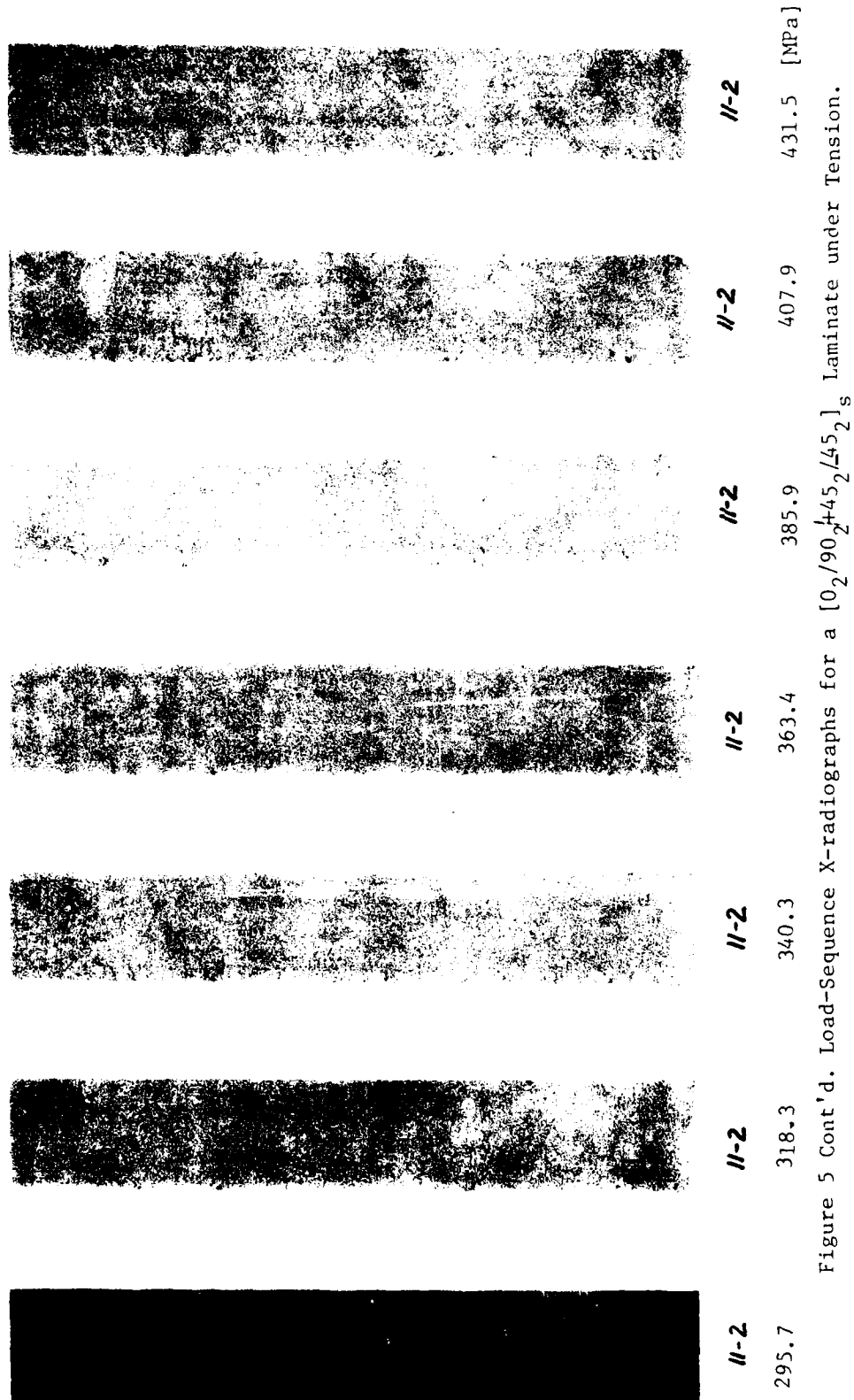
Figure 5 Cont'd. Load-Sequence X-radiographs for a $[0_2/90_2/+45_2/-45_2]_s$ Laminate under Tension.

Figure 5 Cont'd Load-Sequence X-radiographs for a $[0_2/90_2/+45_2/-45_2]_s$ Laminate under Tension.

II-2   *II-2*   *II-2*   *II-2*   *II-2*

454.1   476.6   505.9   521.7   553.3   [MPa]
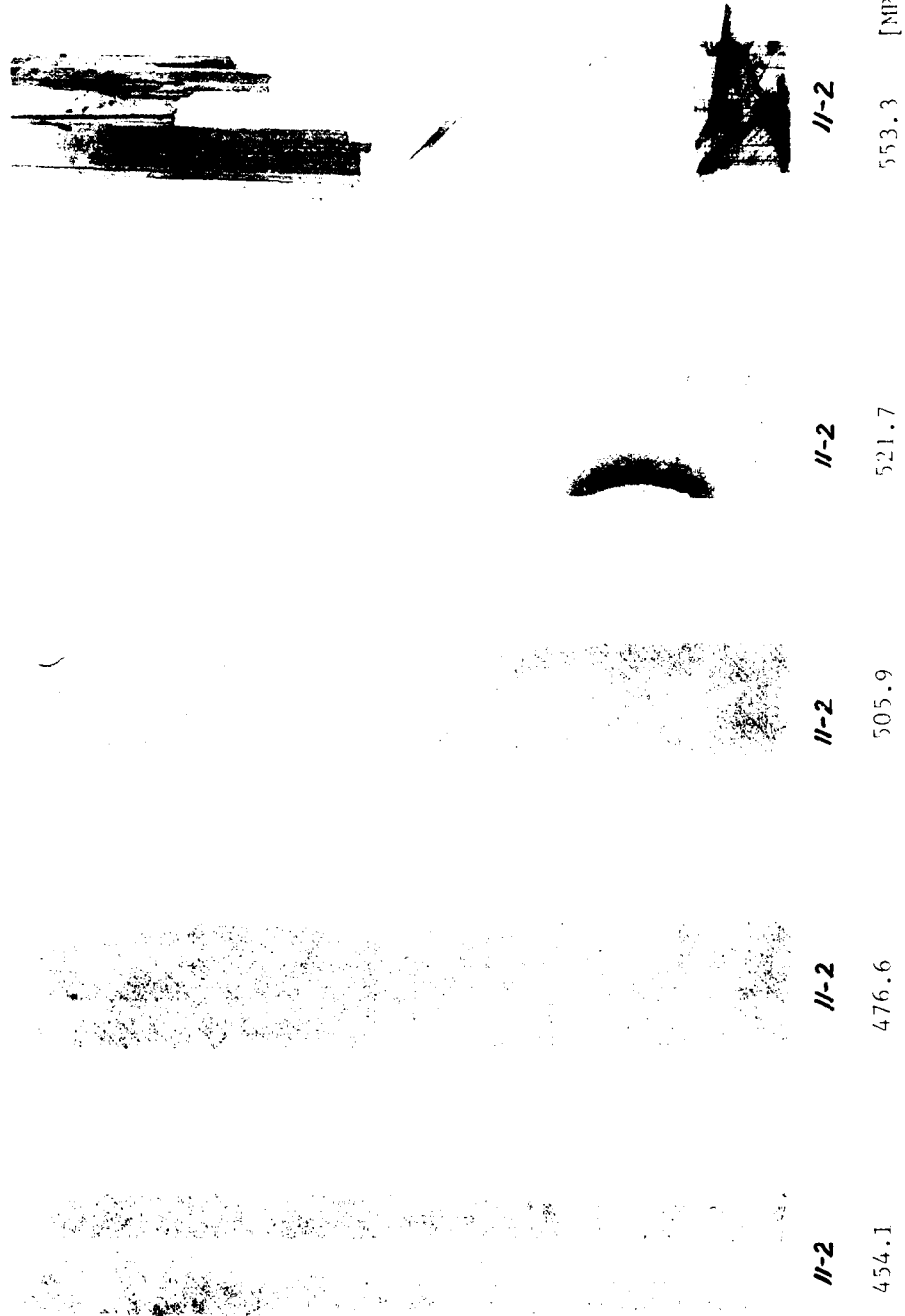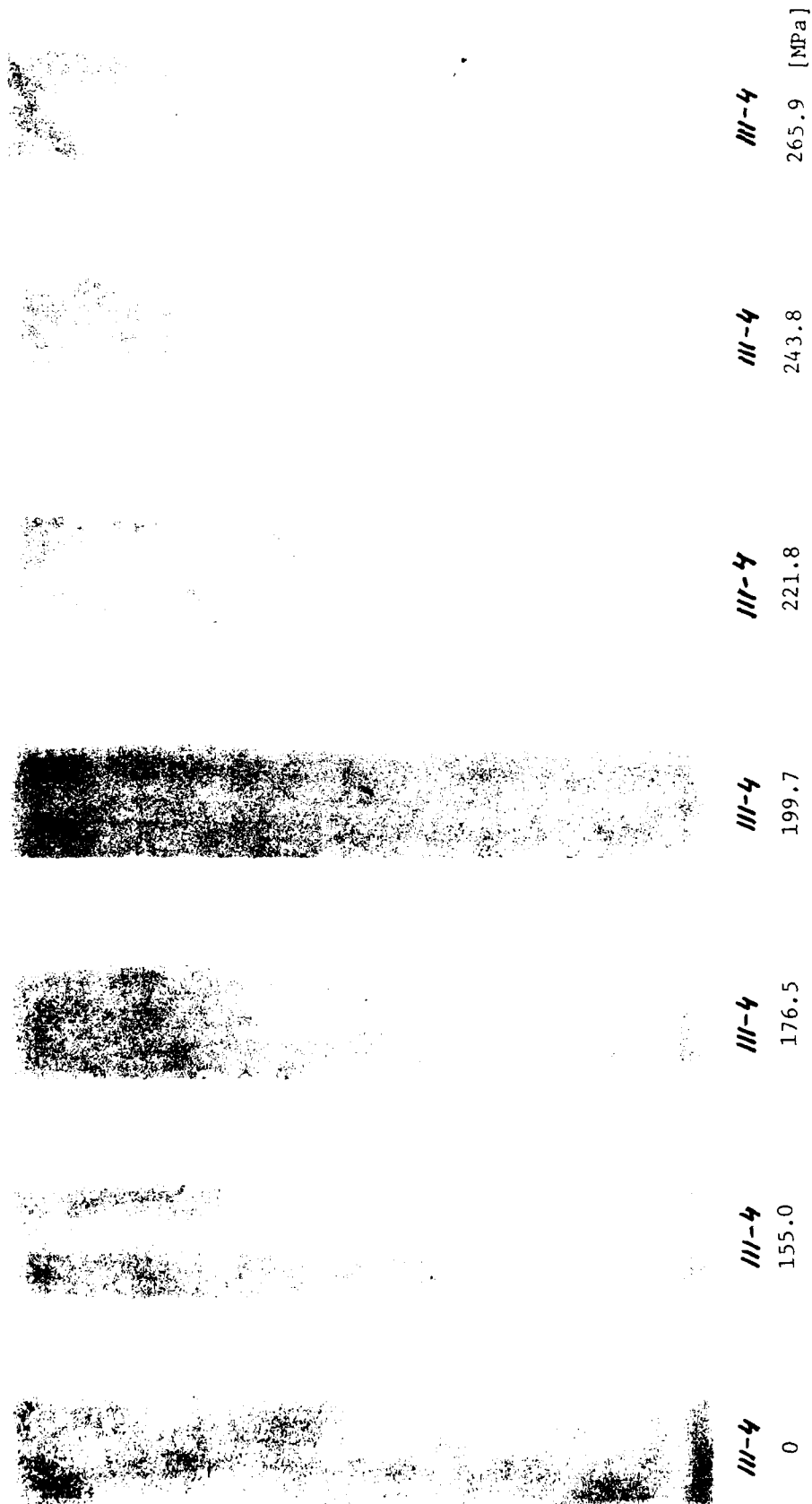
Figure 6. Load-Sequence X-radiographs for a $[90_2/0_2/-45_2/45_2]_s$ Laminate under Tension.

III-4
288.0

III-4
315.9

III-4
333.2

III-4
355.8

III-4
377.9

III-4
399.4

III-4
422.6   [MPa]

Figure 6 Cont'd: Load-Sequence X-radiographs for a $[90_2/0_2/-45_2/45_2]_s$ Laminate under Tension.
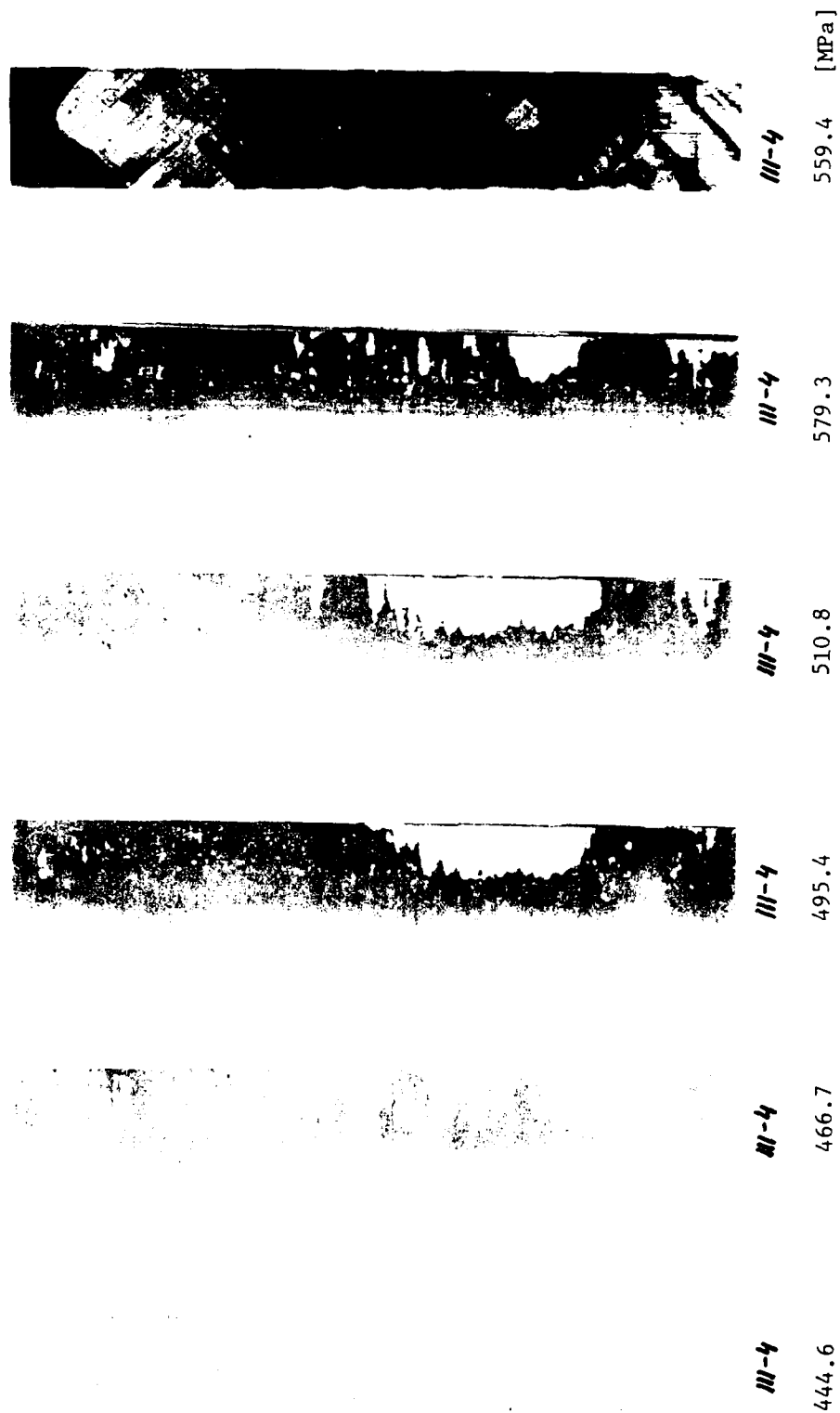
Figure 6 Cont'd: Load-Sequence X-radiographs for a $[90_2/0_2/-45_2/45_2]_s$ Laminate under Tension.

$[45/-45/0/90_2]_s$
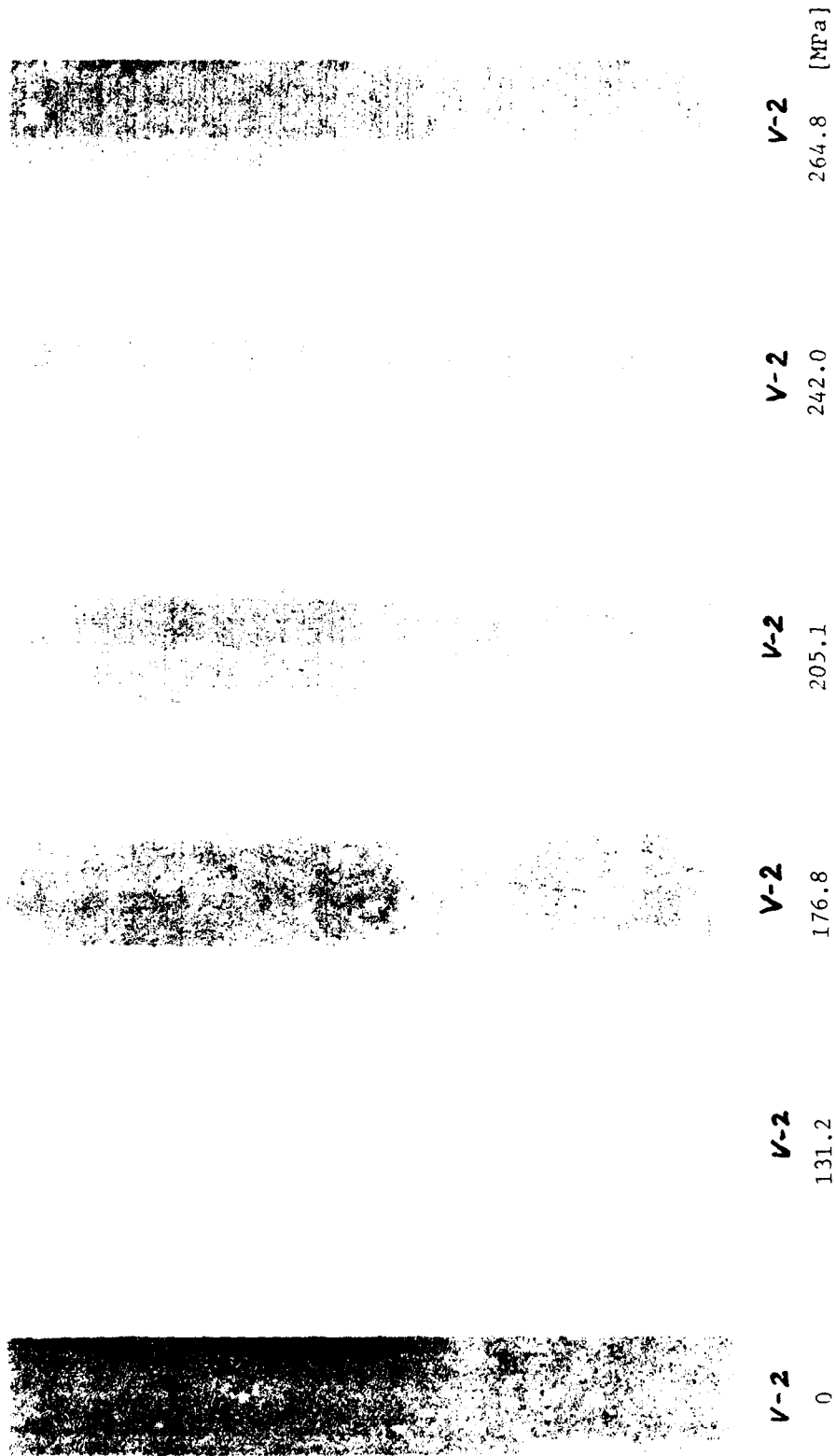
Figure 7. Load-Sequence X-radiographs for $[\pm45/0/90_2]_s$ Laminate under Tension

V-2	V-2	V-2	V-2	V-2	V-2
0	131.2	176.8	205.1	242.0	264.8 [MPa]
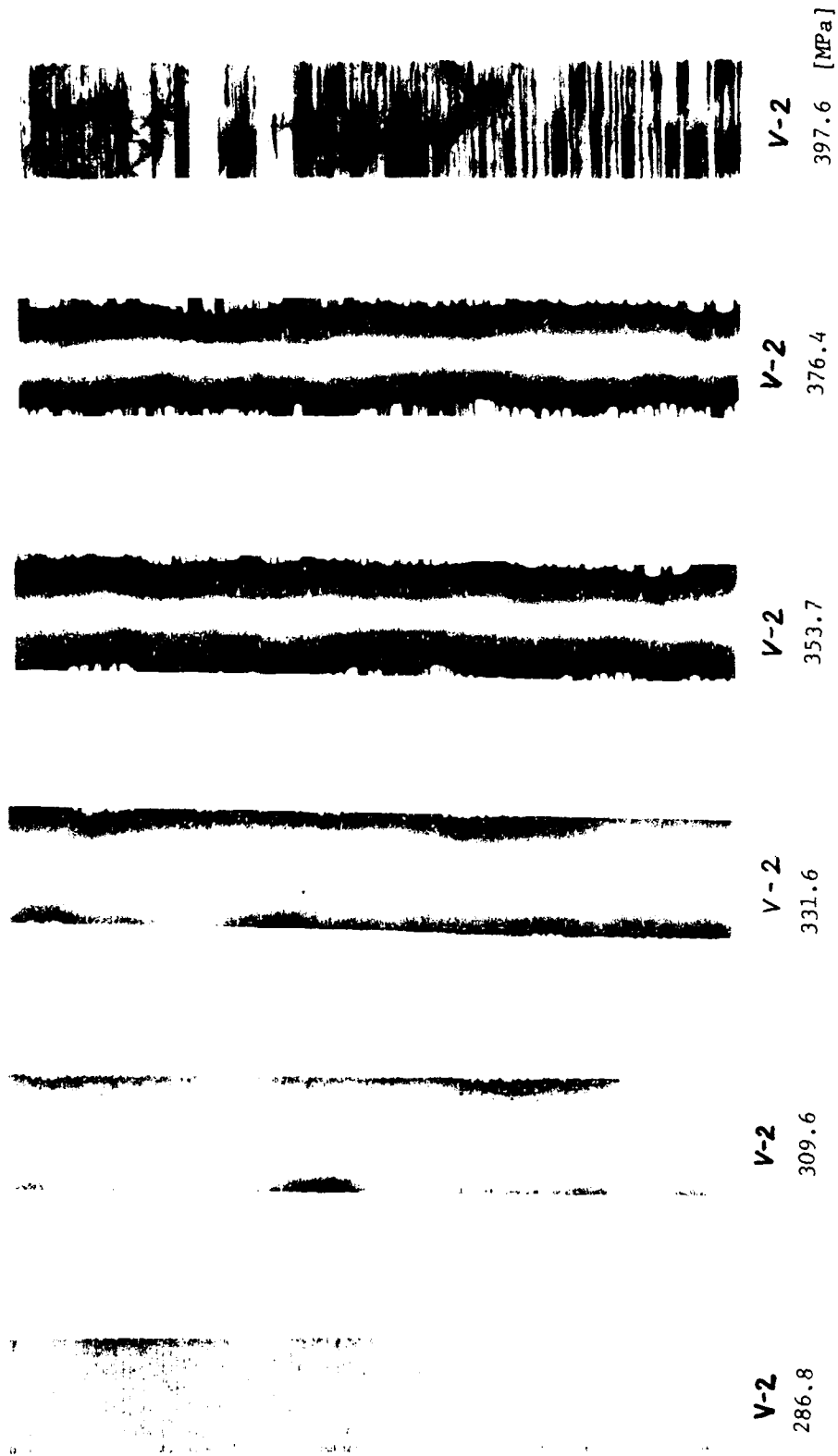
Figure 7 Cont'd: Load-Sequence X-radiographs for $[\pm 45/0/90_2]_s$ Laminate under Tension
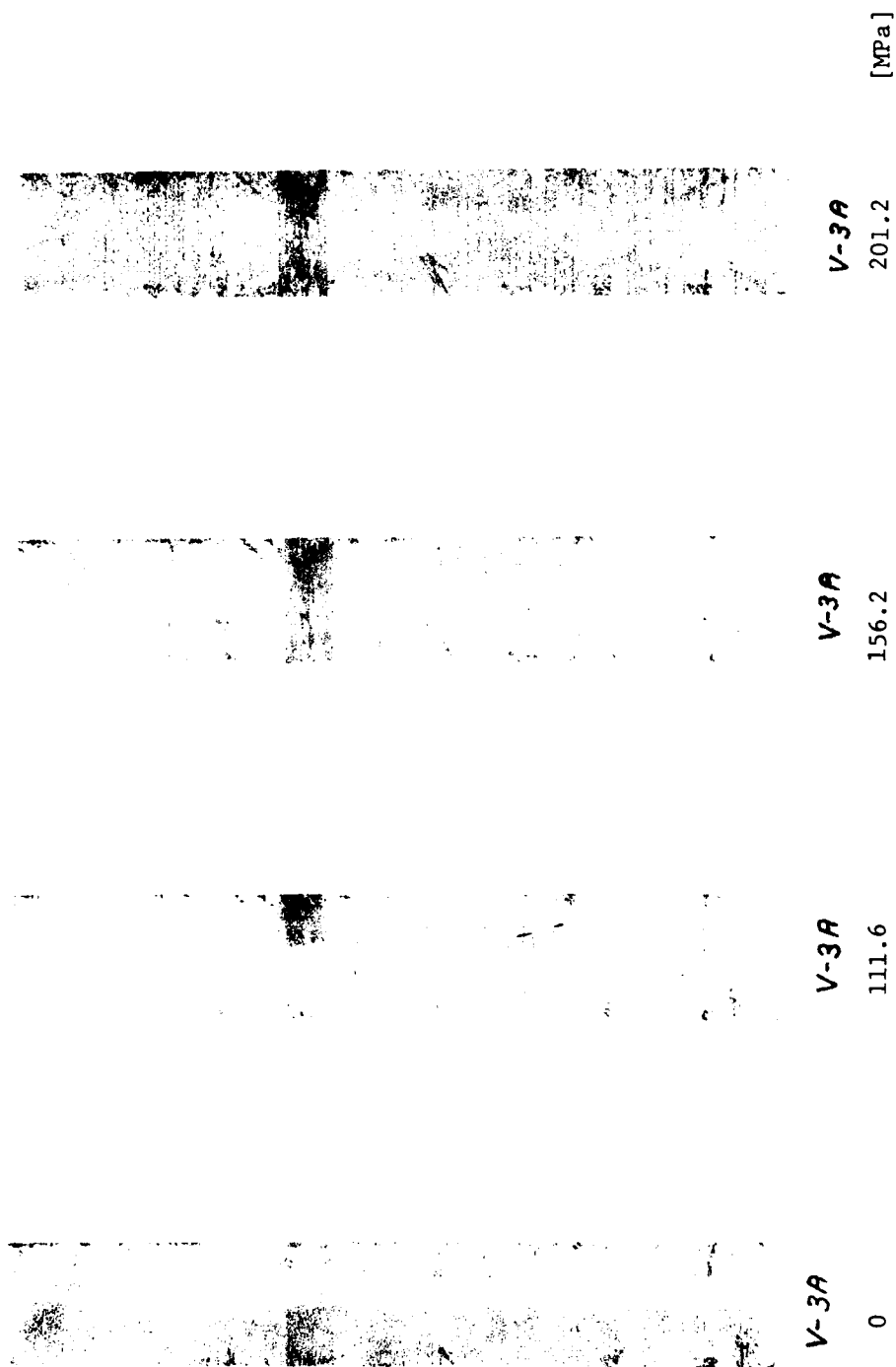
Figure 8. Load-Sequence X-radiographs for $[\pm 45/0/90_2]_s$-A Laminate under Tension
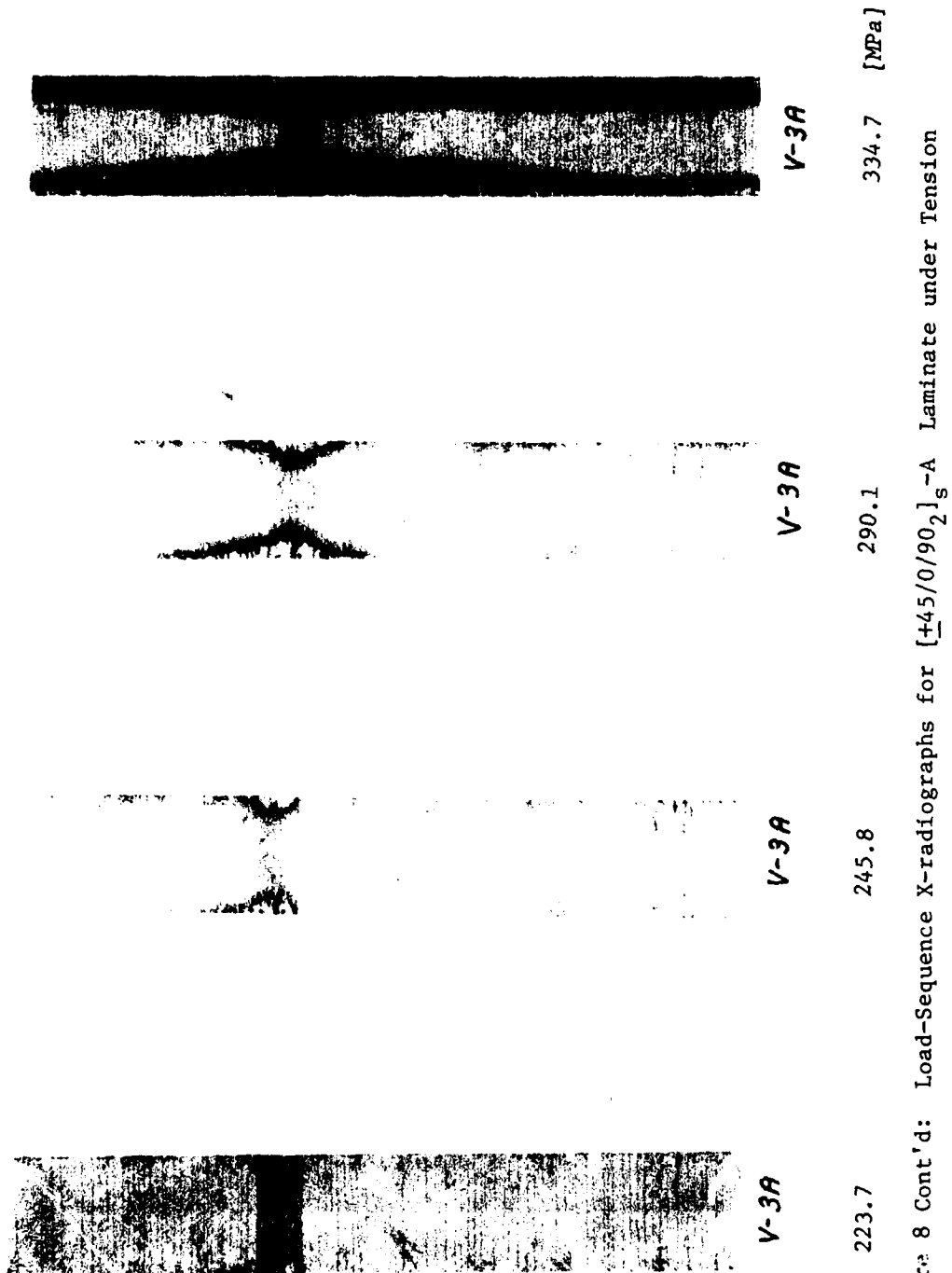
77

Figure 8 Cont'd: Load-Sequence X-radiographs for $[\pm 45/0/90_2]_s$ -A Laminate under Tension
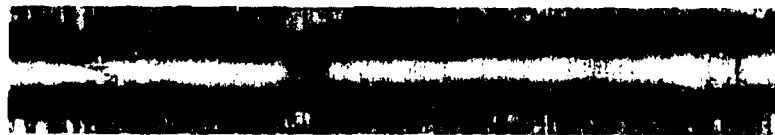
Figure 8 Cont'd: Load-Sequence X-radiographs for $[\pm 45/0/90_2]_s$ -A Laminate under Tension
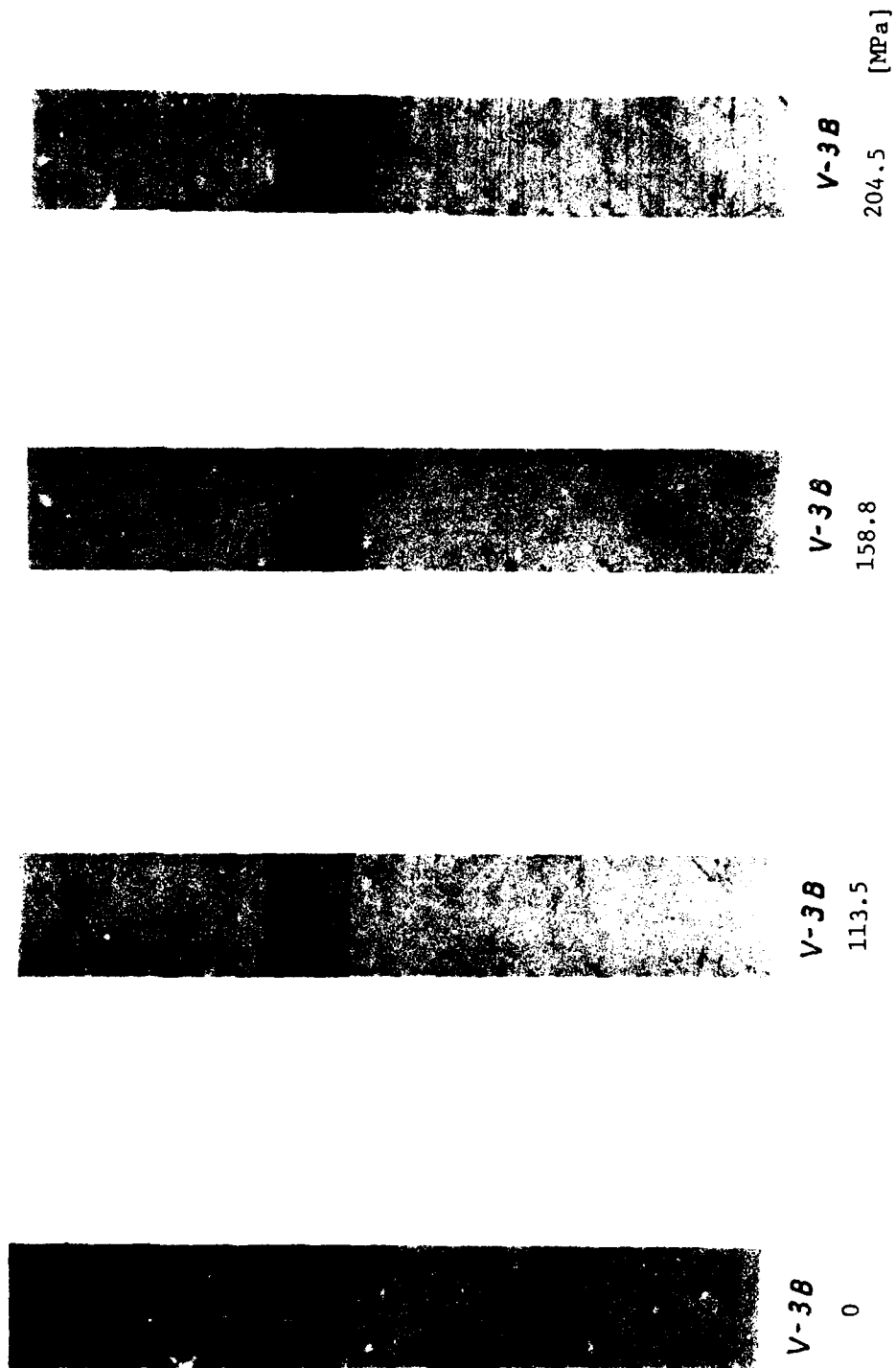
Figure 9. Load-Sequence X-radiographs for $[\pm 45/0/90_2]_s$-B Laminate under Tension
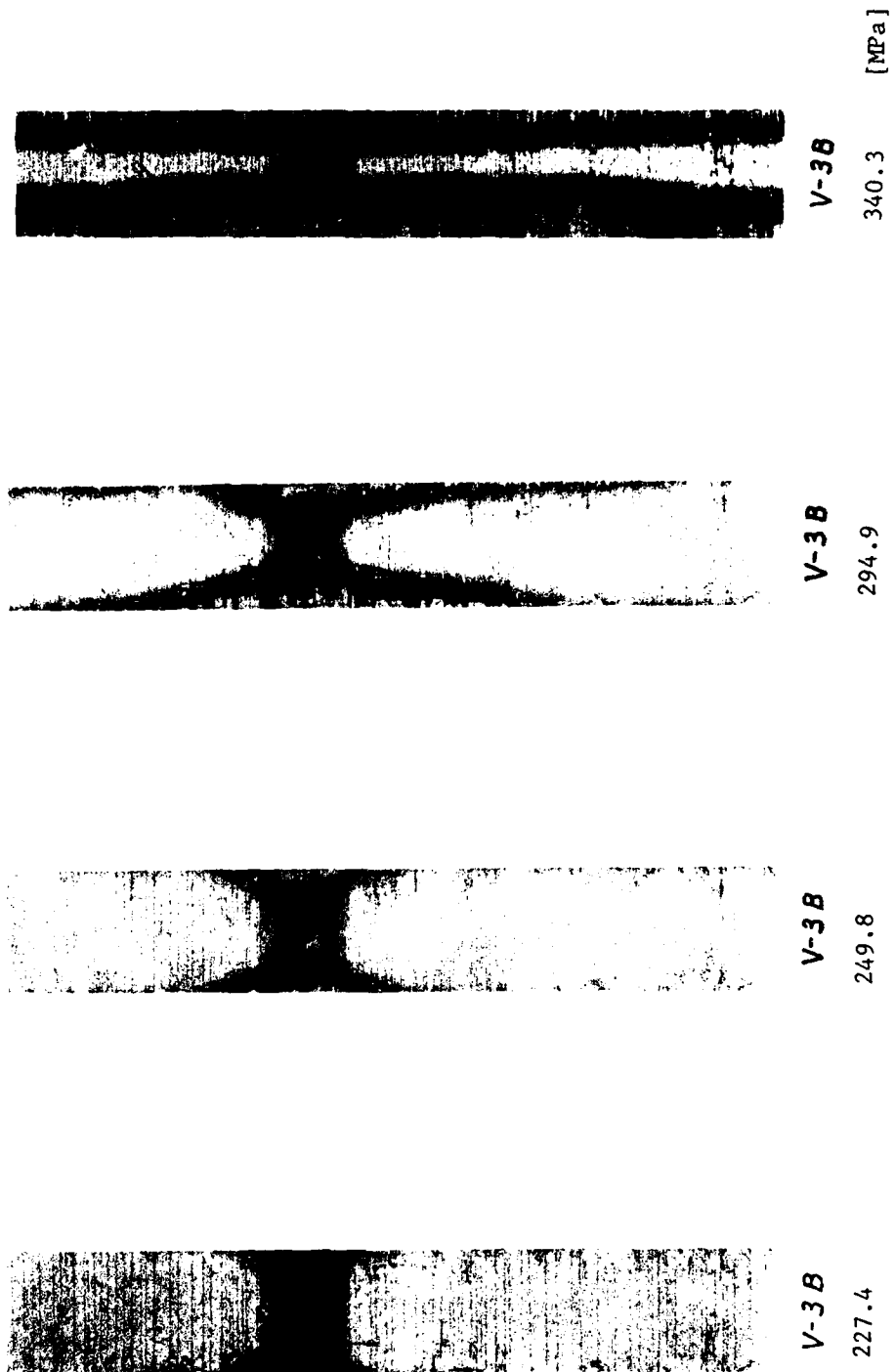
Figure 9 Cont'd: Load-Sequence X-radiographs for $[\pm 45/0/90_2]_s$ -B Laminate under Tension
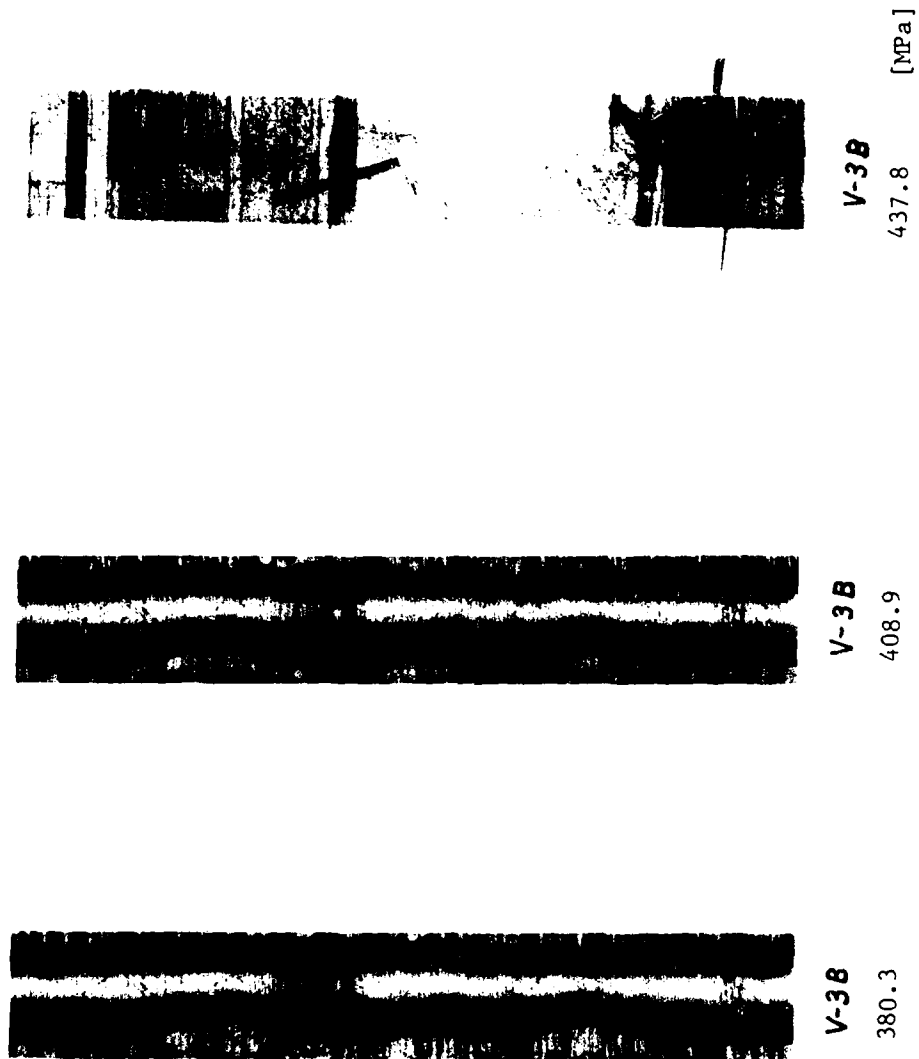
81

Figure 9 Cont'd: Load-Sequence X-radiographs for $[\pm 45/0/90_2]_s$-B Laminate under Tension

No implant
implanted 6.3 mm Teflon strip - "A"
implanted 12.7 mm Teflon strip - "B"

E. Delamination [%]

100
80
60
40
20

0   100   200   300   400   500   σ[MPa]

b) Edge delamination in [%] of width vs applied load

No implant
implanted 6.3 mm Teflon strip - "A"
implanted 12.7 mm Teflon strip - "B"
⊙ onset of edge delamination

T.C. Density

16
12
8
4

0   100   200   300   400   σ[MPa]

a) Transverse crack density vs applied load

Figure 10. 90°-Cracking and Edge Delamination Growth Behavior of
$[\pm 45/0/90_2]_s$ laminates under Tension

//-2 G

0

//-2 G

238.5

//-2 G

258.3

//-2 G

300.3   [MPa]

//-2 G

317.1

//-2 G

333.3

//-2 G

357.7

//-2 G

376.8   [MPa]
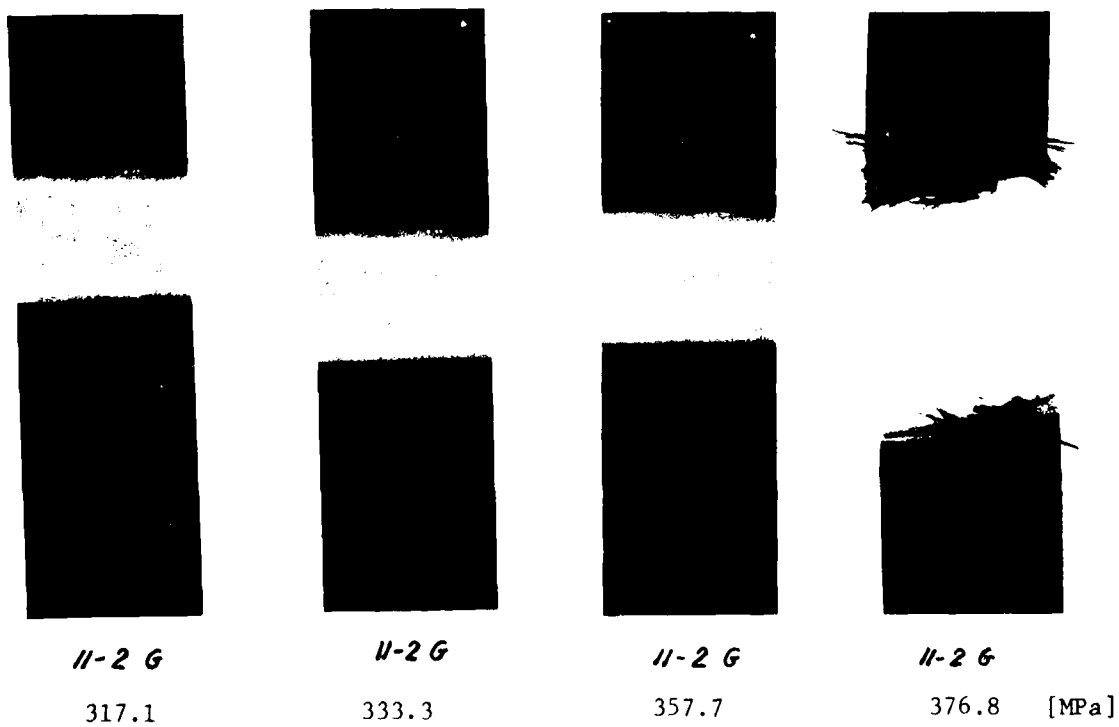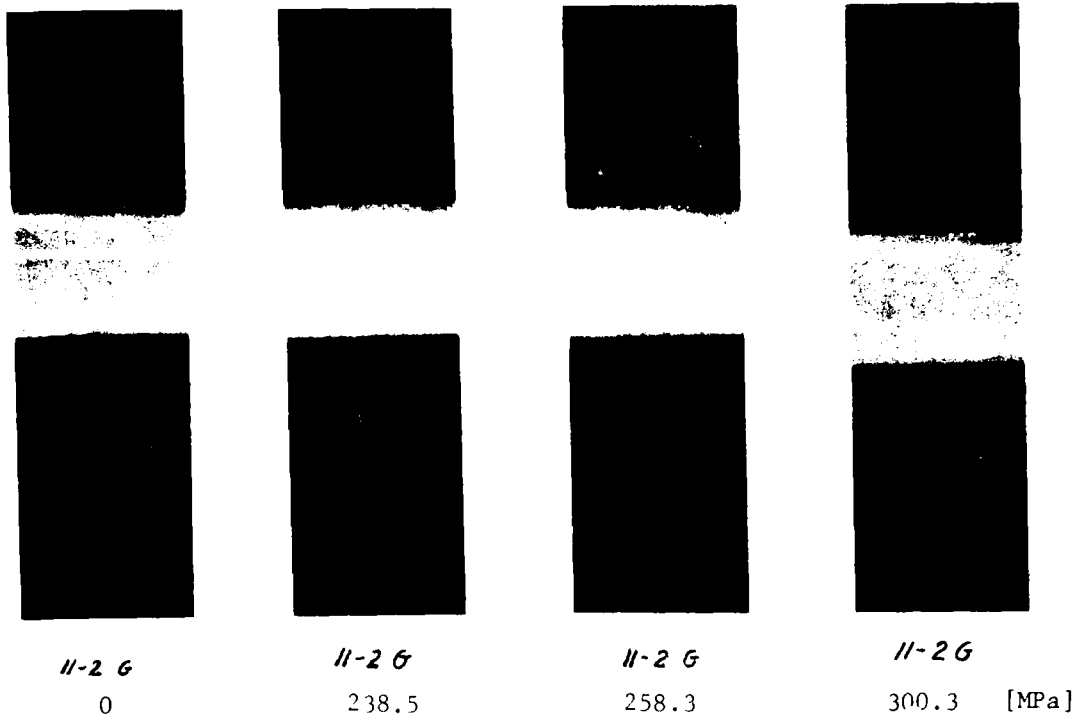
Figure 11.   Load-Sequence of X-radiographs for $[0_2/90_2/\pm45_2]_s$

Laminates under Step-Compression

11- 6 A

0

11 - 6 A

120.5

11 - 6A

146.1   [MPa]

11 - 6A

172.6

11 - 6A

206.8

11 - 6A

240.9
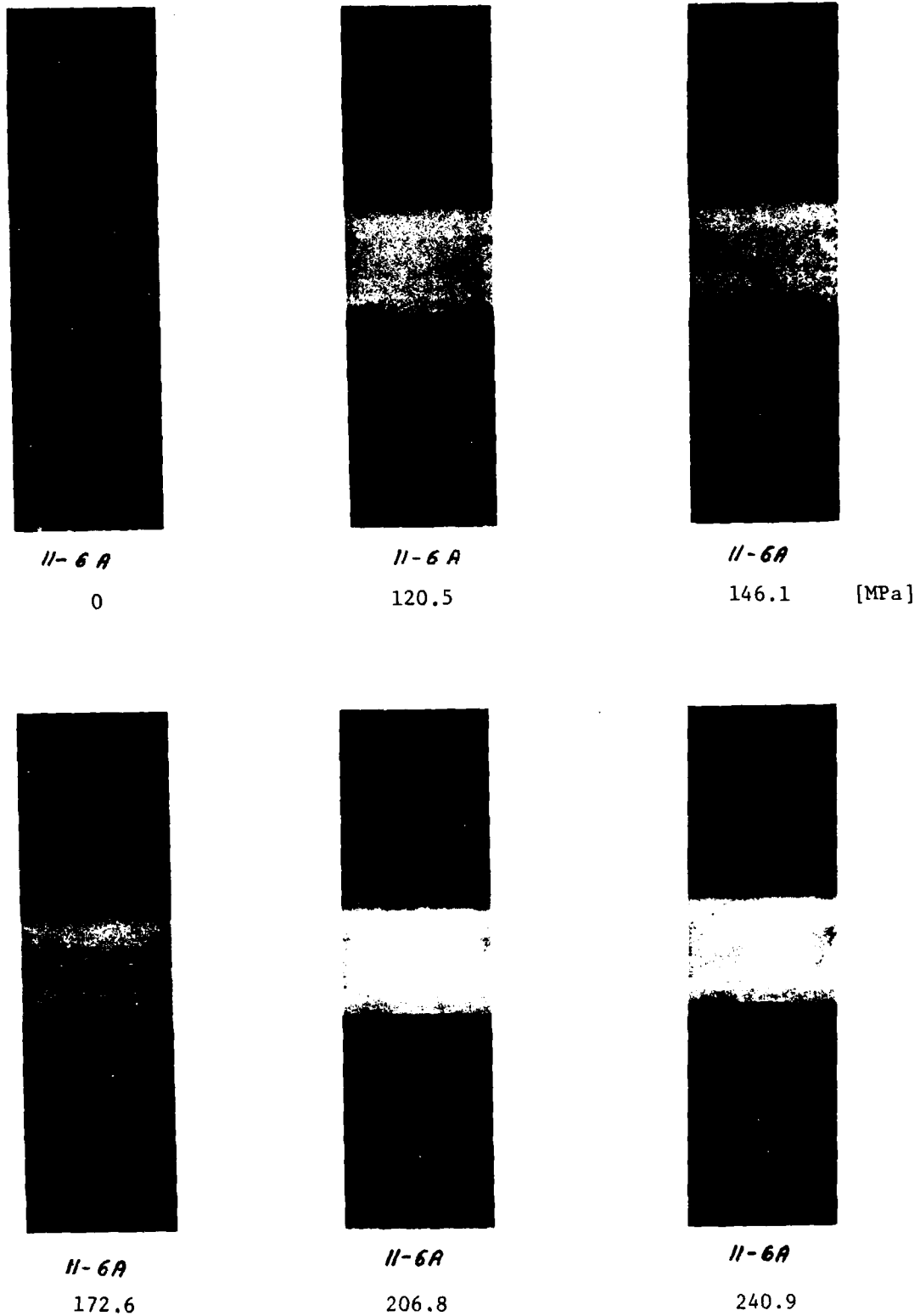
Figure 12.   Load-Sequence of X-radiographs for $[0_2/90_2/\pm45_2]_s$ type A
Laminates under Step-Compression.

85

II- 6 A   *II-6A*   *II - 6 A*
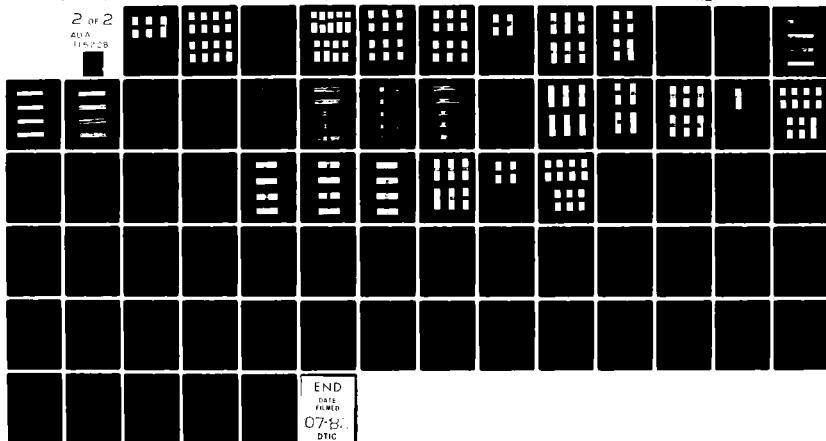
266.6   283.7   294.8   [MPa]

Figure 12 Cont'd: Load-Sequence of X-radiographs for $[0_2/90_2/\pm45_2]_s$
type A Laminates under Step-Compression
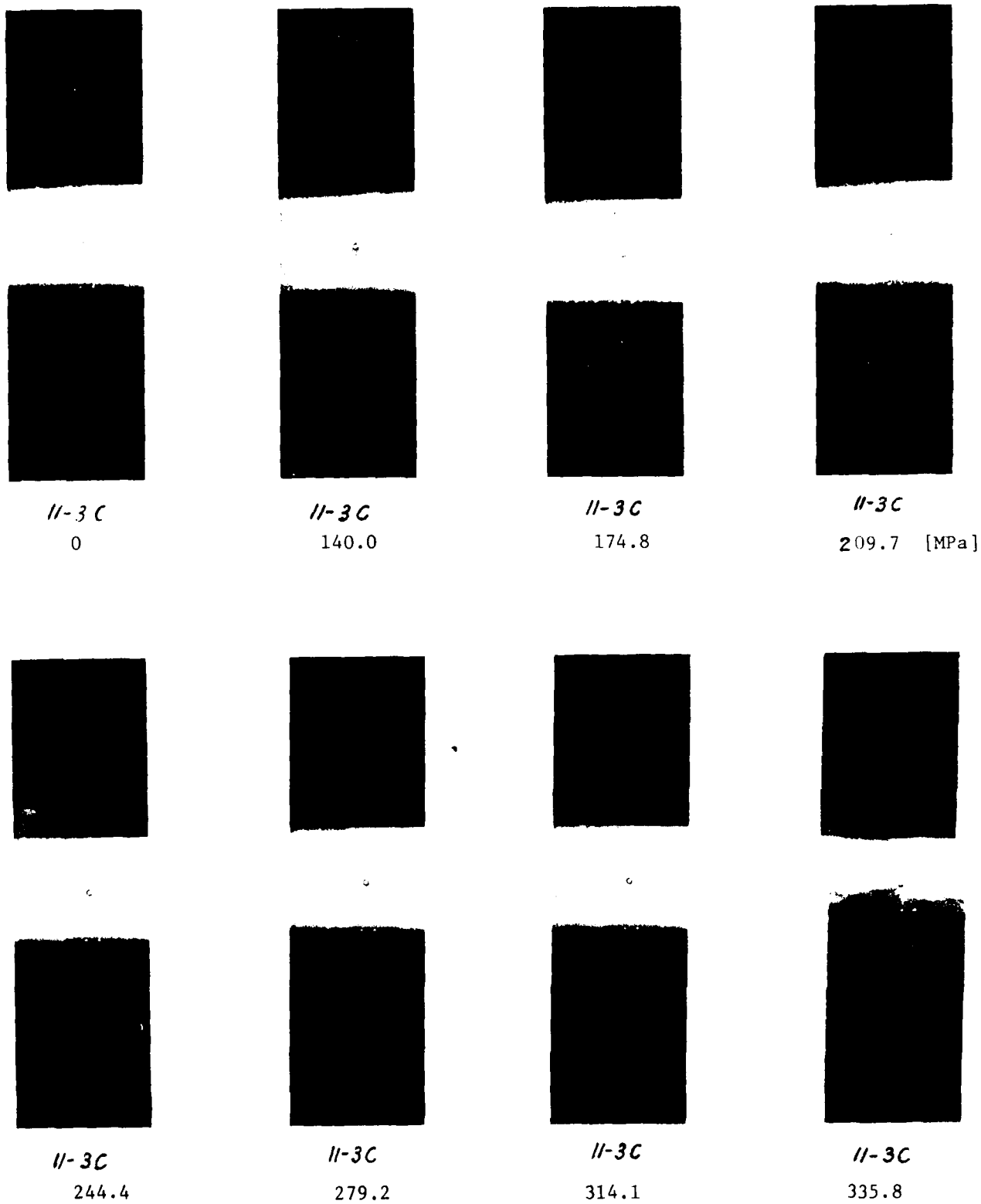
Figure 13. Load-Sequence of X-radiographs for $[0_2/90_2/\pm45_2]_s$ type C Laminates under Step-Compression.

87
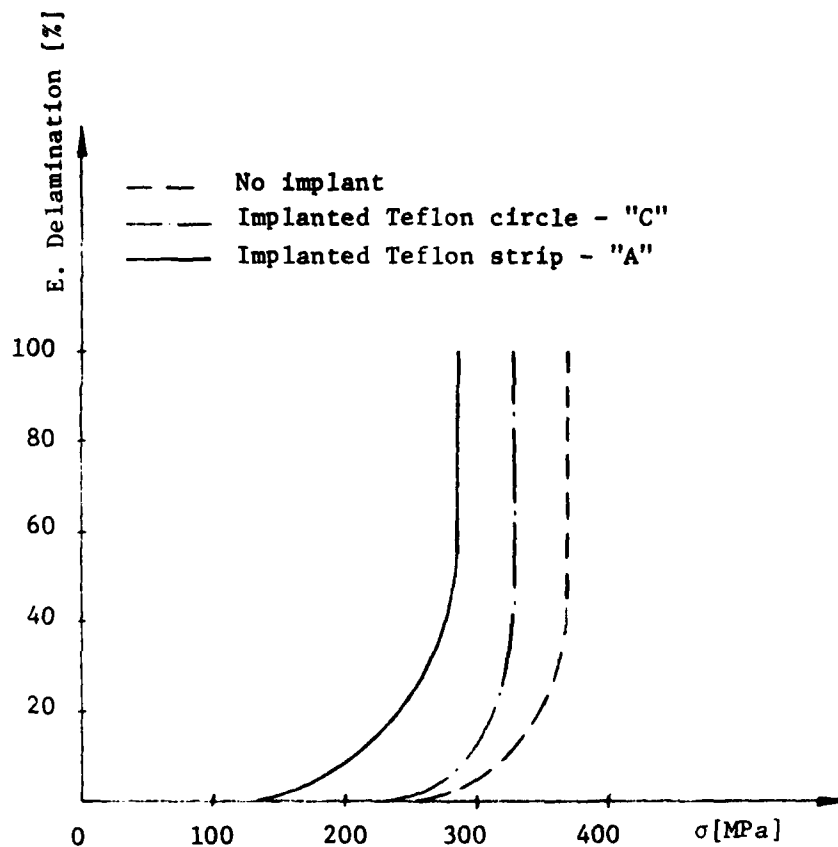
Figure 14. Delamination Growth vs Applied Load for
$[0_2/90_2/45_2/-45_2]_s$ Laminate Series under
Step-Compression
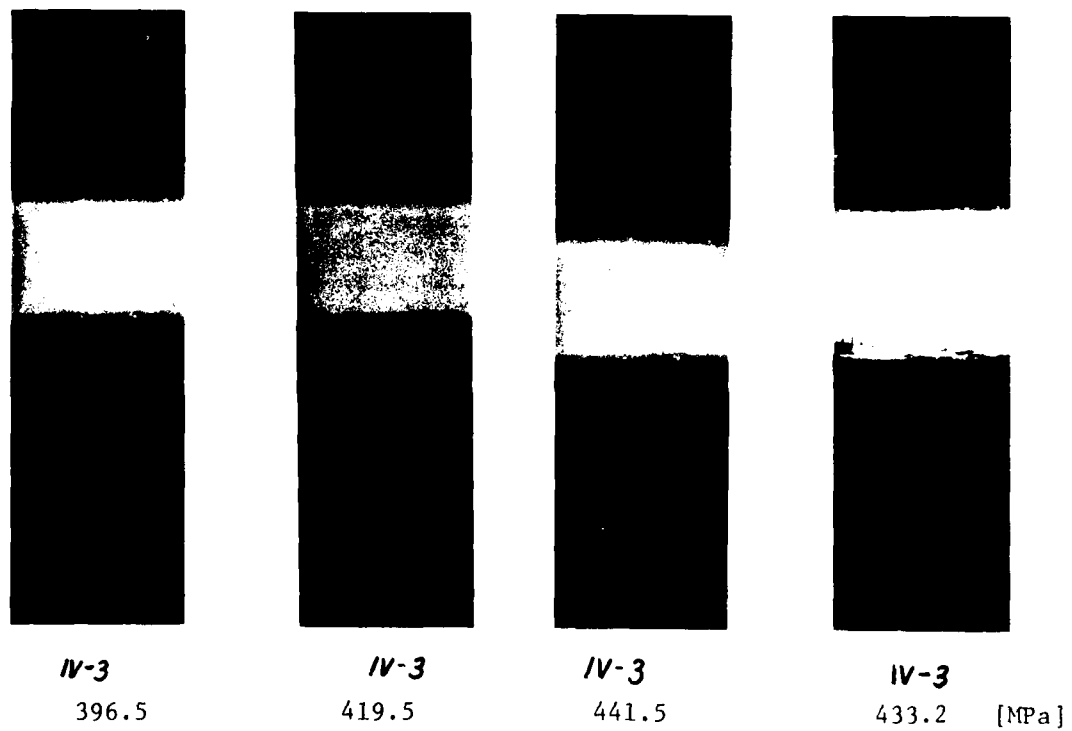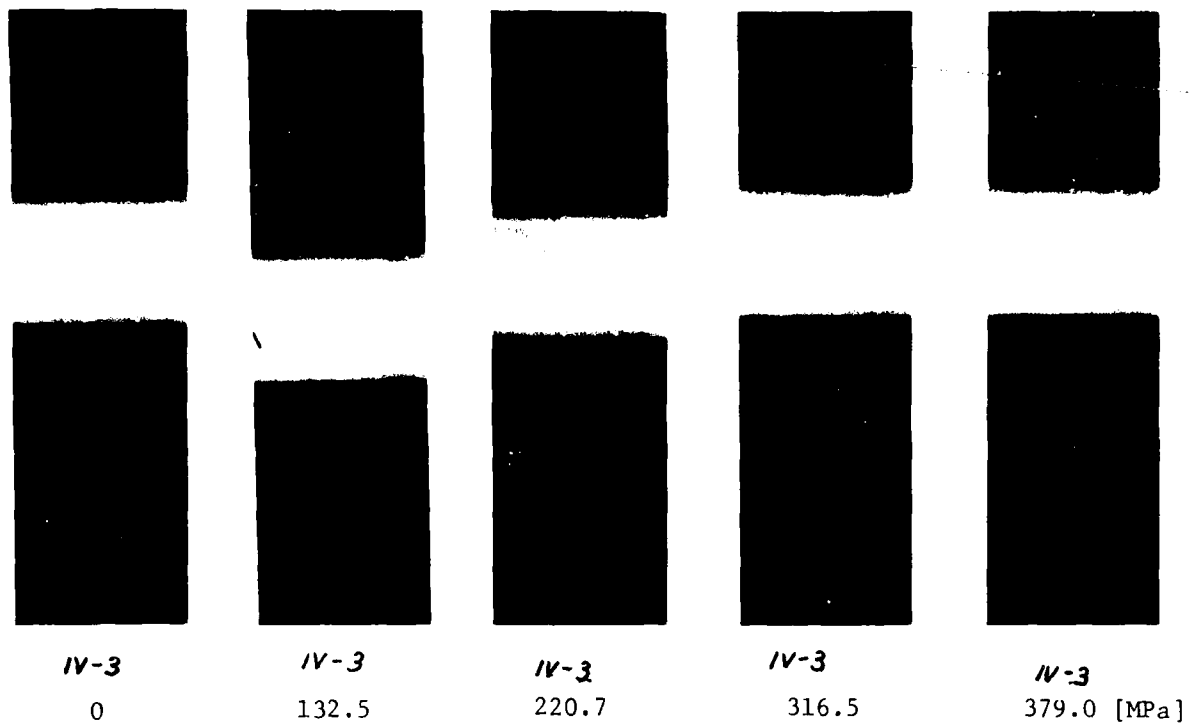
Figure 15. Load-Sequence X-radiographs for [0/90/0/90/45/-45/45/-45]$_s$ Laminates under Step-Compression.

IV-8 A

0

IV-8 A

119.3

IV-8 A

144.8   [MPa]

IV-8 A

171.0

IV-8 A

204.9

IV-8 A

238.8   [MPa]

Figure 16.   Load-Sequence X-radiographs for [0/90/0/90/45/-45/45/-45]$_s$

type A Laminates under Step-Compression

IV-8A

264.1

N-8A

281.9

IV-8 A

298.9   [MPa]

IV-8A

323.4

IV-8A

349.6

N-8A

375.1   [MPa]

Figure 16   Cont'd: Load-Sequence X-radiographs for $[0/90/0/90/45/-45/45/-45]_s$
type A   Laminates under Step-Compression.

91

IV-8A

392.9

IV-8A

376.7   [MPa]

Figure 16 Cont'd: Load-Sequence X-radiographs for $[0/90/0/90/45/-45/45/-45]_s$
type A   Laminates under Step-Compression

Figure 17. Load-Sequence X-radiographs for [0/90/0/90/45/-45/45/-45]$_s$ type C
Laminates under Step-Compression
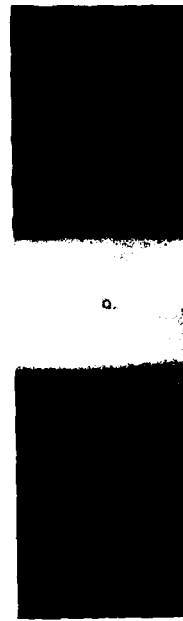
IV-2C
302.7

IV-2C
323.0   [MPa]

IV-2C
336.3

IV-2C
352.3   [MPa]

Figure 17   Cont'd: Load-Sequence X-radiographs for $[0/90/0/90/45/-45/45/-45]_s$
type C Laminates under Step-Compression.

94
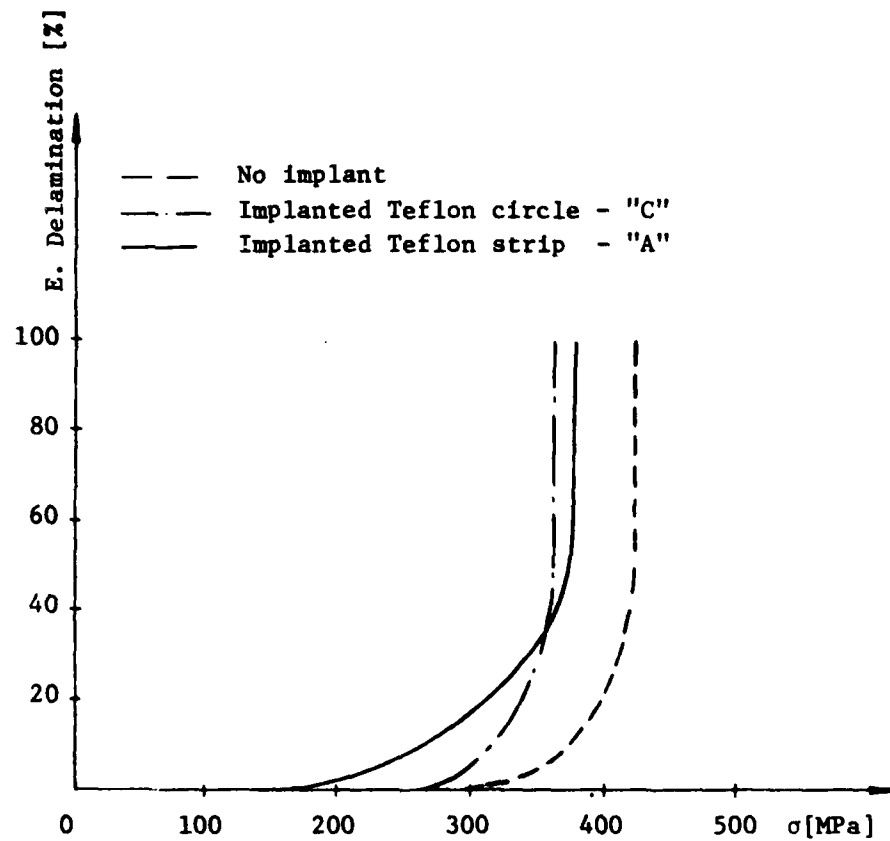
Figure 18. Delamination Growth vs Applied Load for the
$[0/90/0/90/45/-45/45/-45]_s$ Laminate Series
under Step-Compression

95
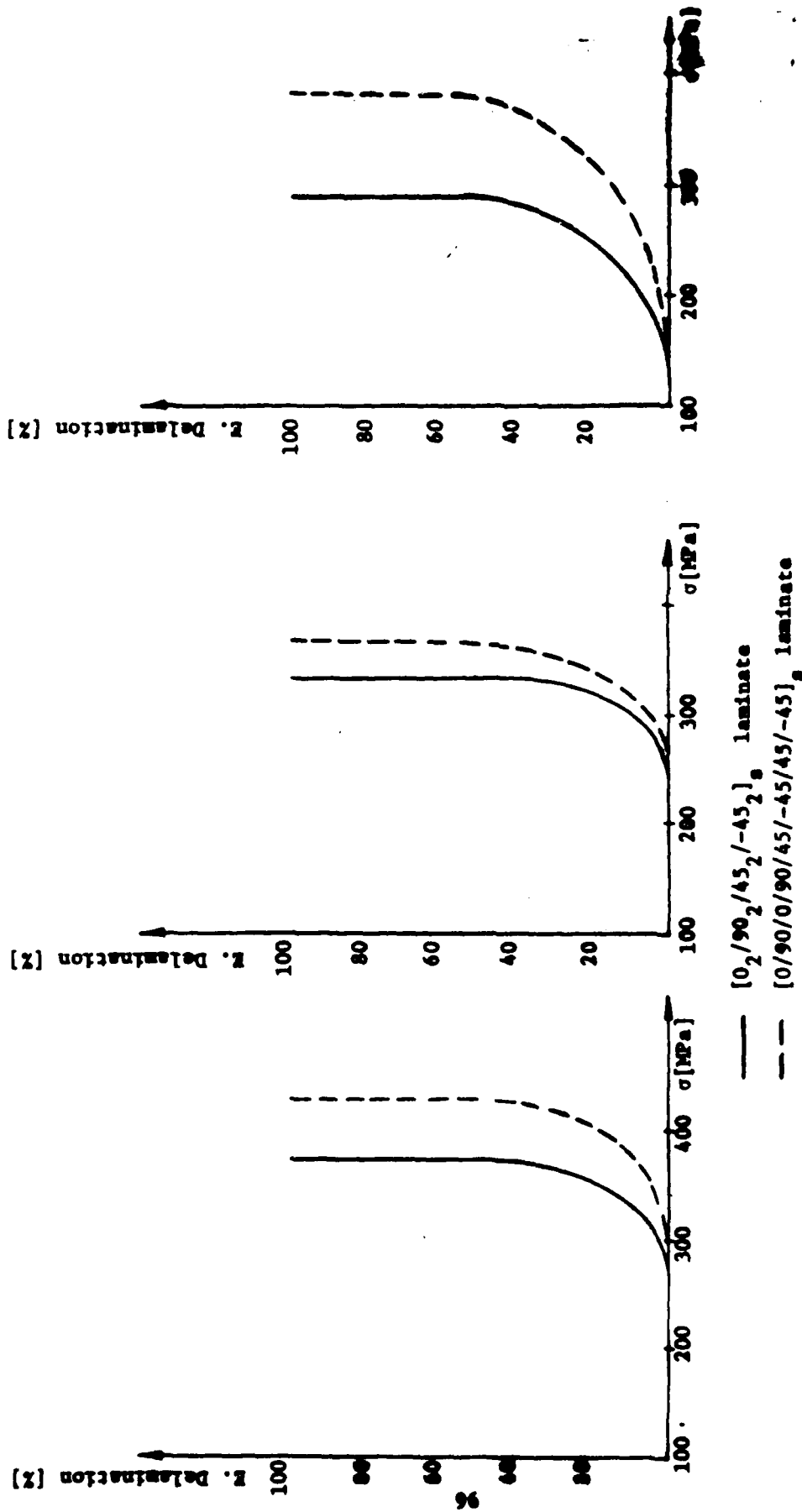
Figure 19. Edge Delamination Growth vs Applied Load for Laminates under Step-Compression

$[0_2/90_2/45_2/-45_2]_s$ laminate

$[0/90/0/90/45/-45/45/-45/-45]_s$ laminate
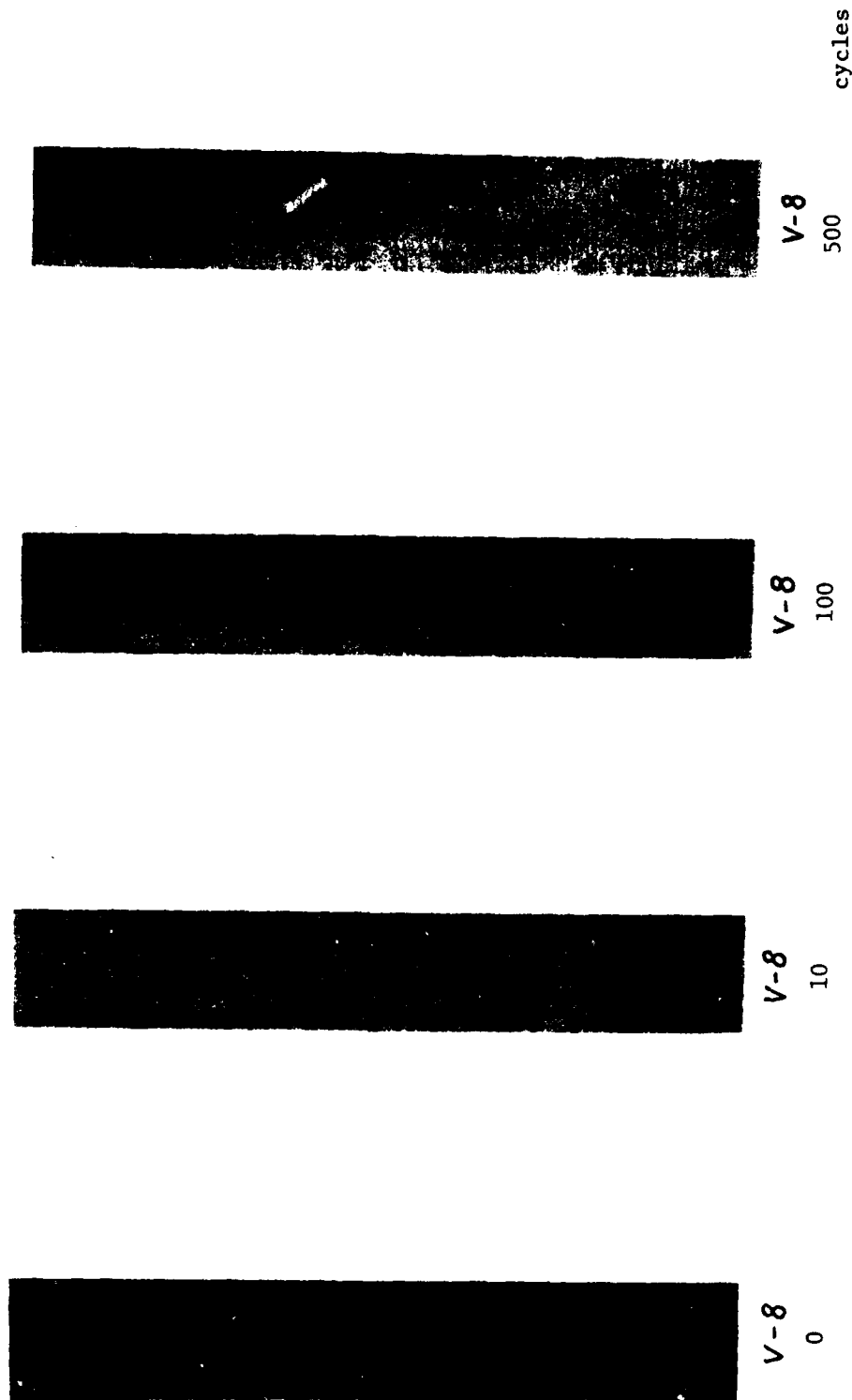
Figure 20. Life-Sequence X-radiographs for $[\pm45/0/90_2]_s$ Laminate under 189 MPa Tension Fatigue Loading.

V-8
30 000

V-8
10 000

V-8
5 000

V-8
1000

cycles

Figure 20 Continued

cycles

V-8
1 000 000

V-8
500 000

V-8
200 000

V-8
70 000
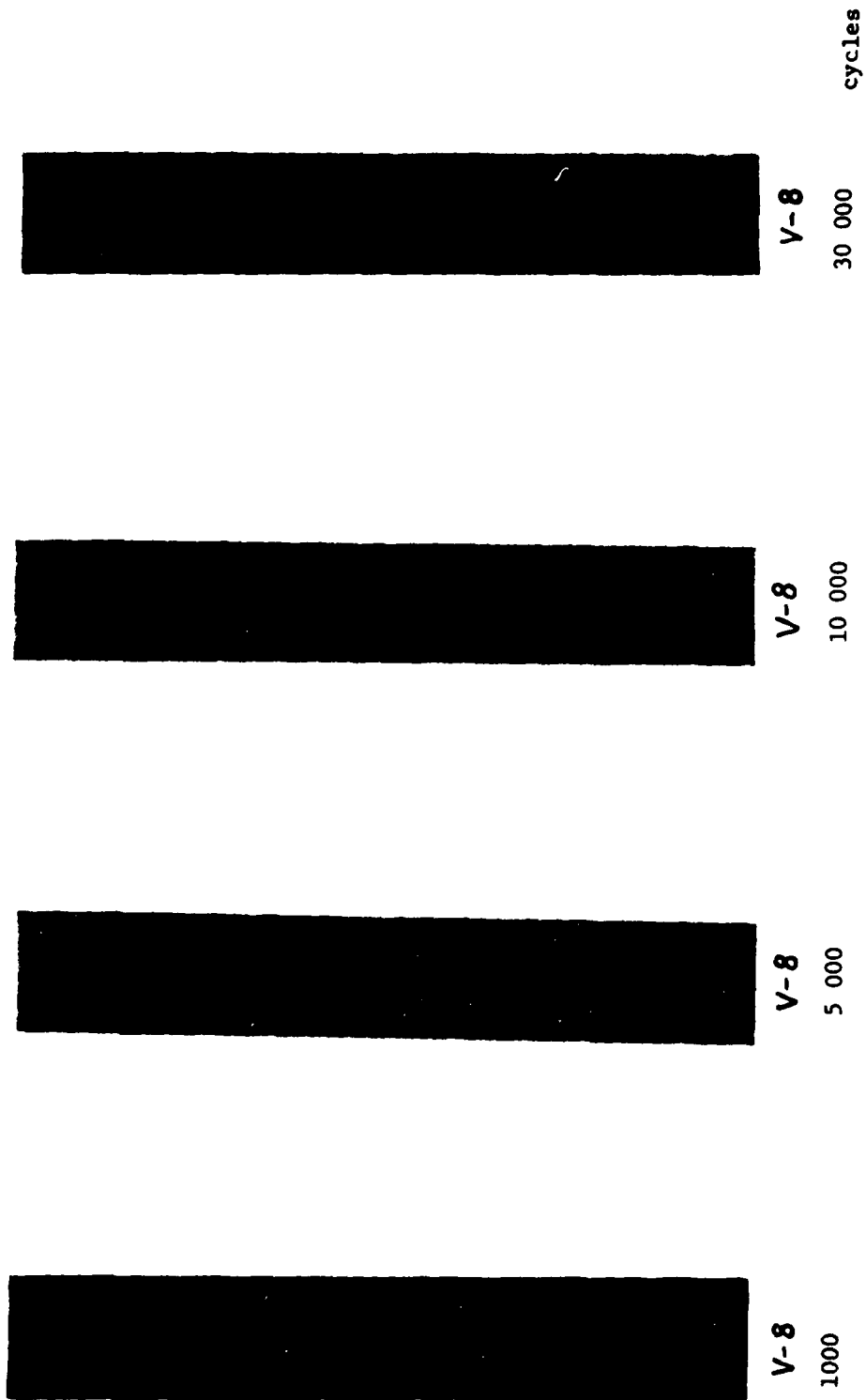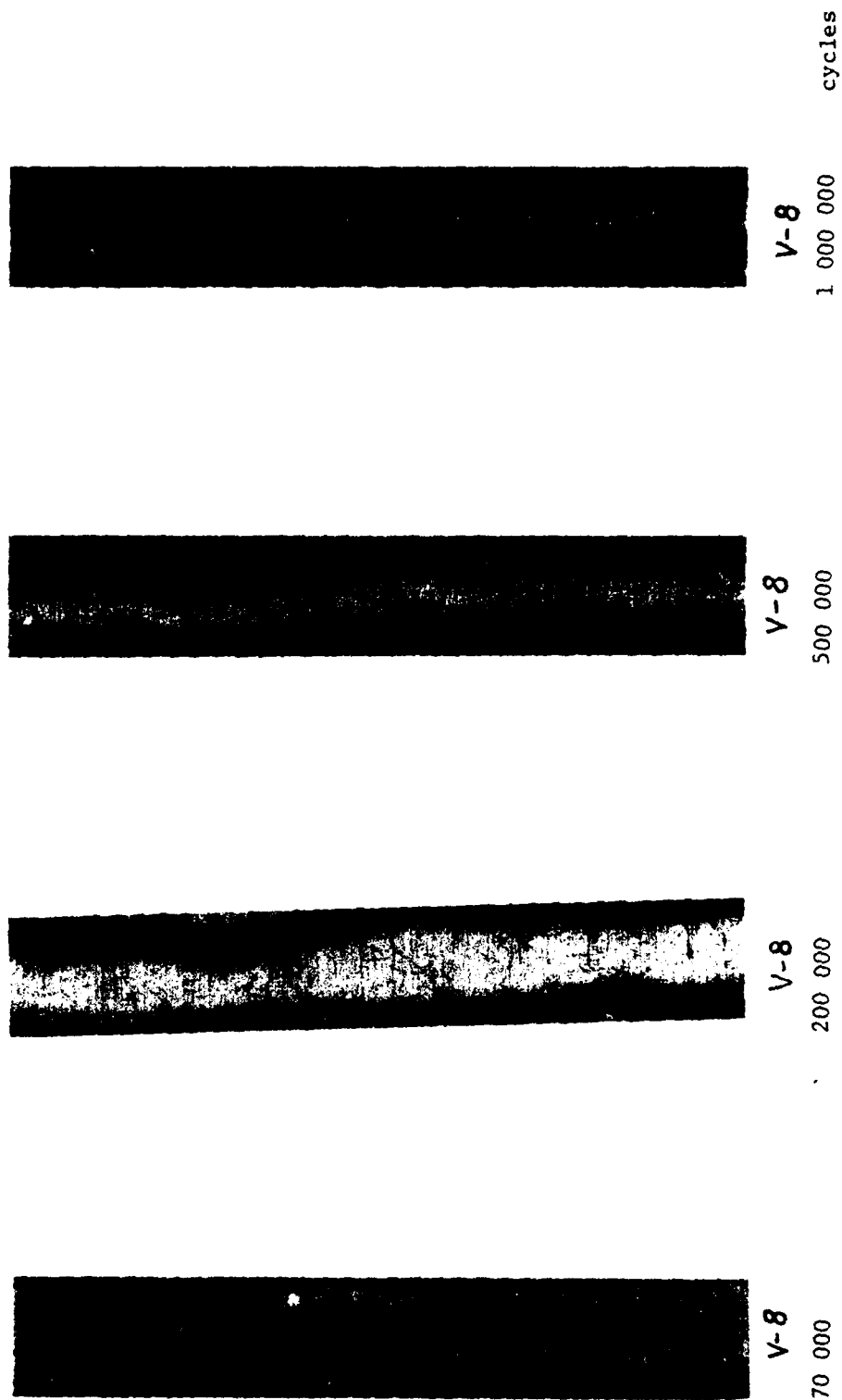
Figure 20 Continued
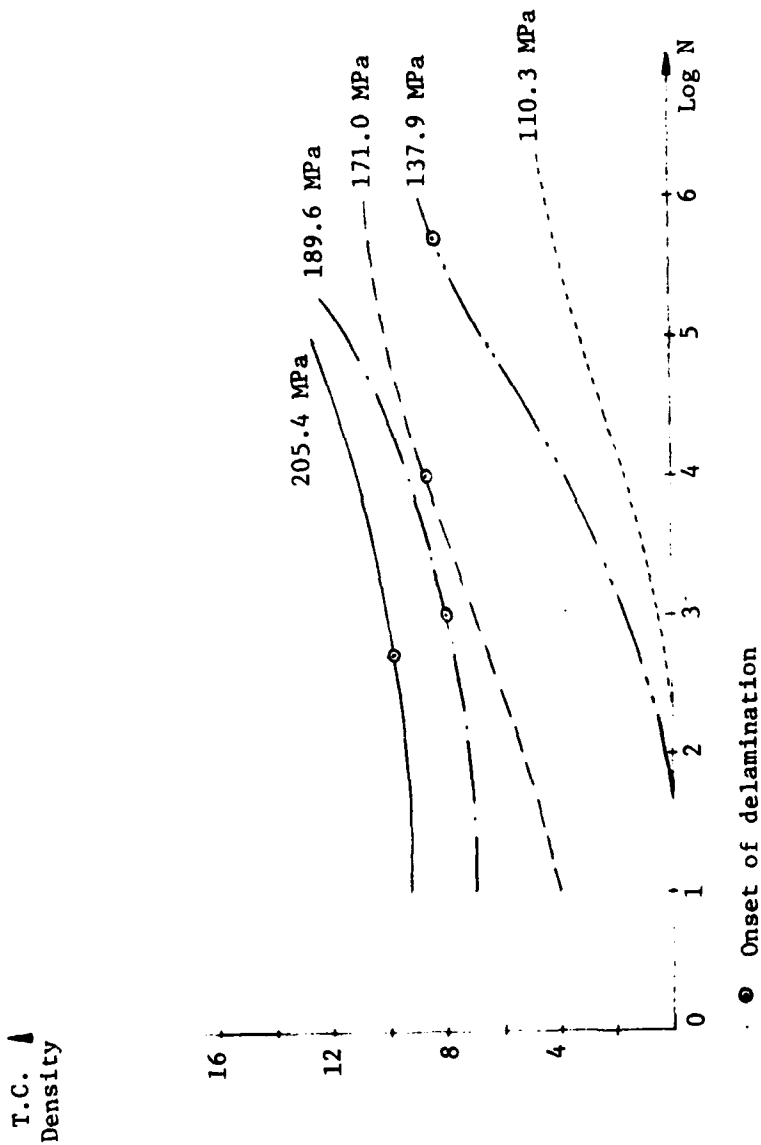
Figure 21. Transverse Crack Density Growth under Tension Fatigue Loads. $[\pm 45/0/90_2]_s$

100
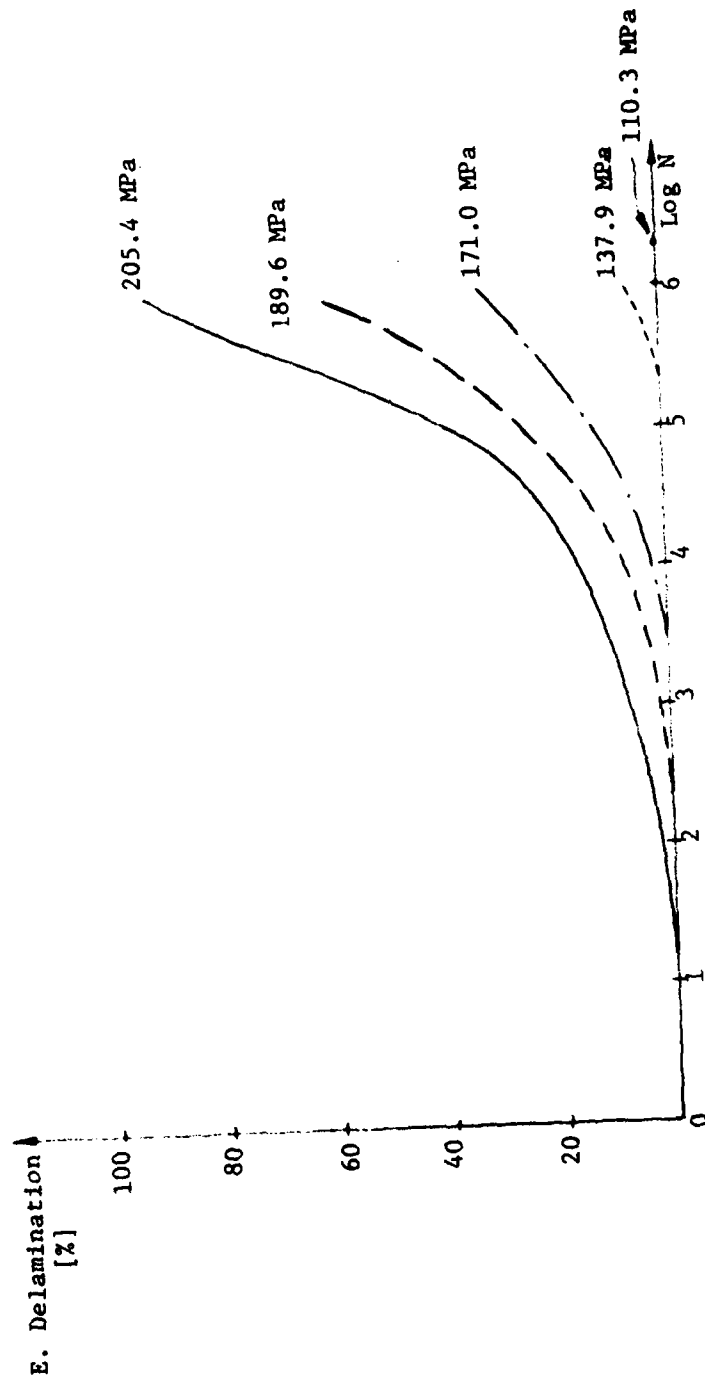
Figure 22. Edge Delamination Growth under Tension Fatigue Loads. $[\pm 45/0/90_2]_s$

$[45/-45/0/90_2]_s - A$

V-4A
0

V-4A
2

V-4A
10

V-4A
50

V-4A
200   cycles
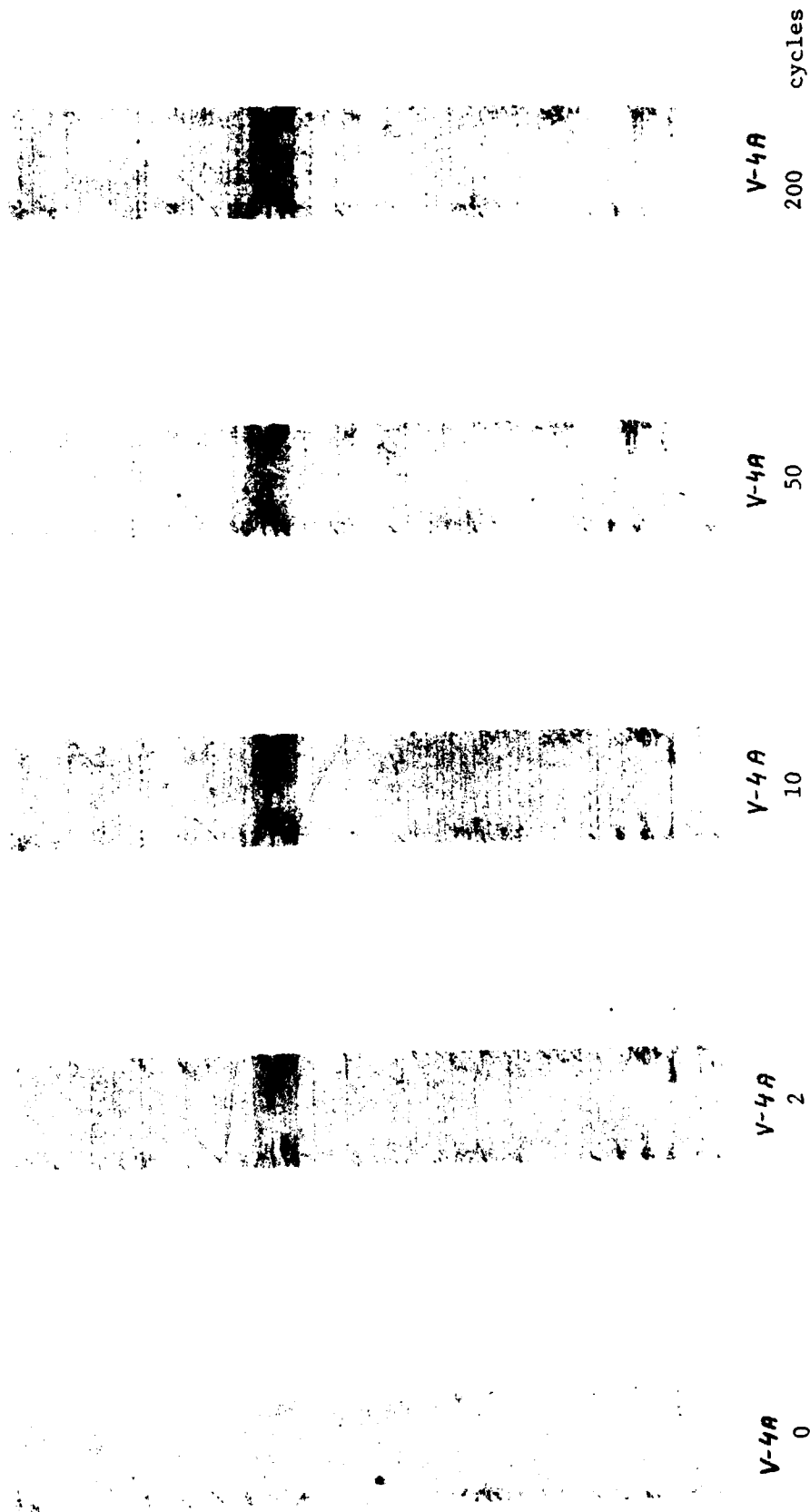
Figure 23. Life-Sequence X-radiographs for $[\underline{+}45/0/90_2]_s$ – type A Laminate under 187 MPa Tension Fatigue Loading.

V-4A   400 000   cycles

V-4A   50 000

V-4A   20 000

V-4A   5 000

V-4A   1 000

Figure 23 Continued.

V-8B
200 cycles

V-8B
50

V-8B
10

V-8B
2

V-8B
0
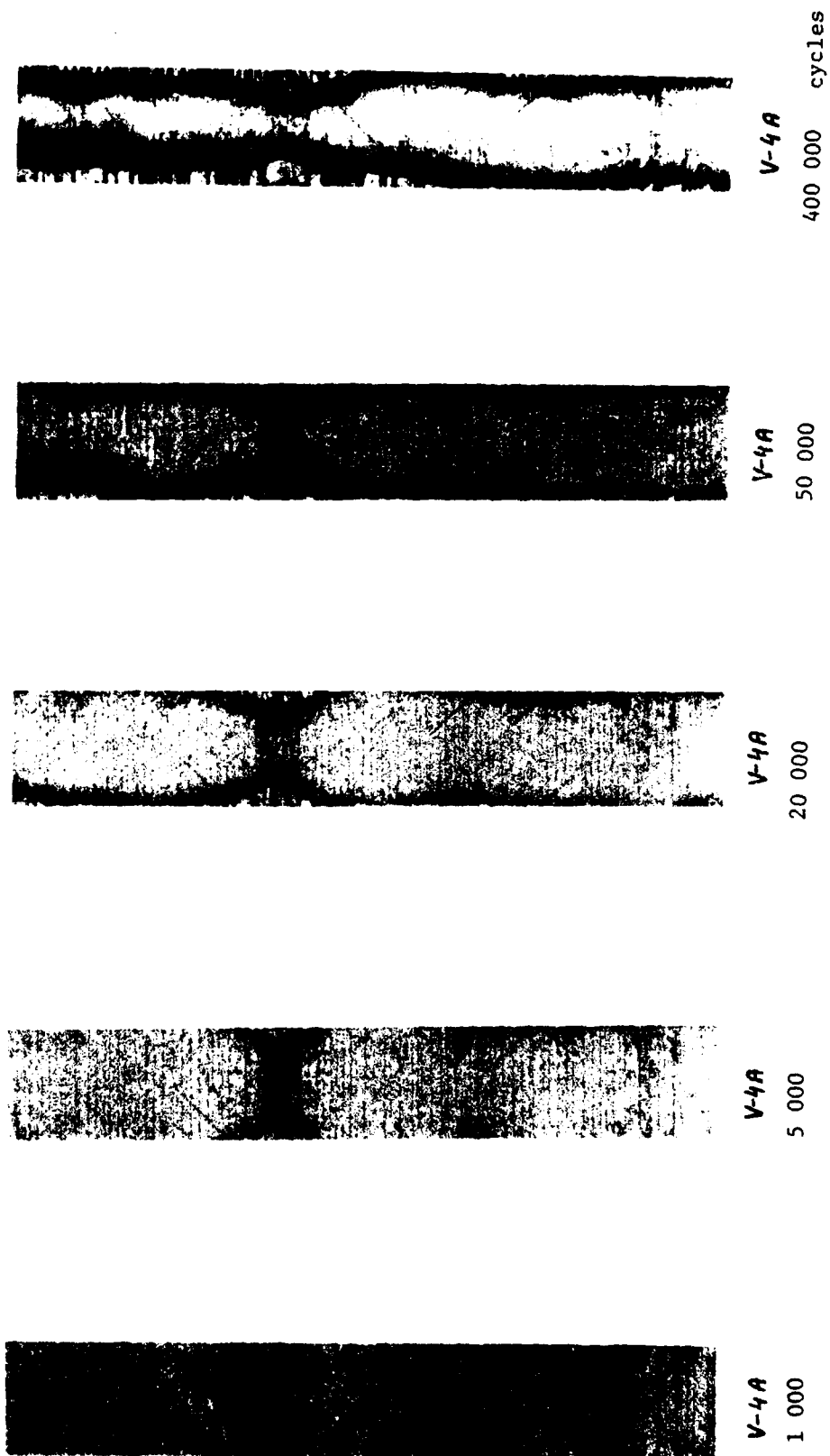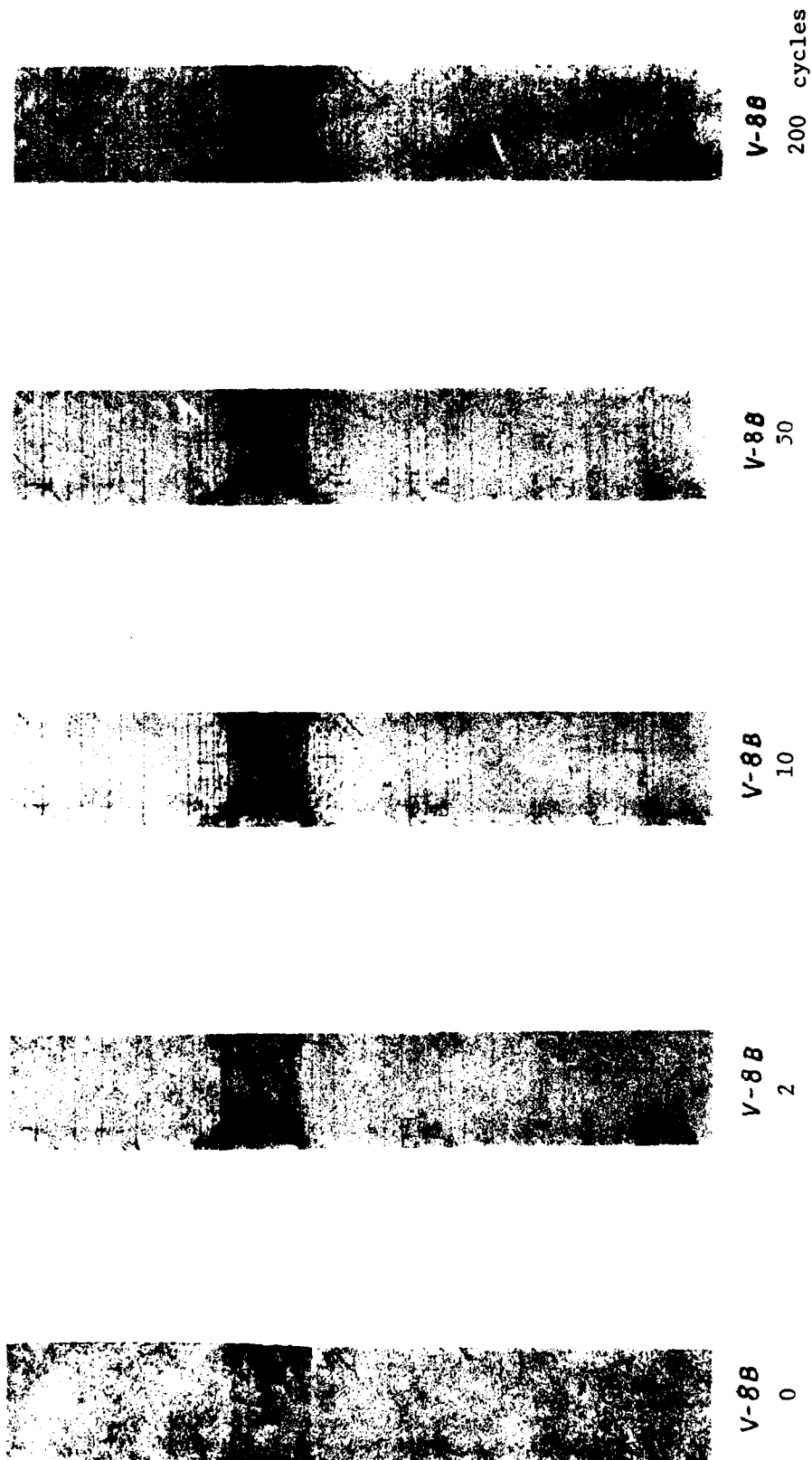
Figure 24. Life-Sequence X-radiographs for $[\pm 45/0/90_2]_s$ - type B Laminate under 189 MPa Tension Fatigue Loading

V-8B   100 000   cycles

V-8B   50 000

V-8B   20 000

V-8B   5 000

V-8B   1 000

Figure 24 Continued

E. Delamination
[%]

σ = 188.2 MPa

—— No implant
— — Implanted 6.3 mm Teflon strip – "A"
— · — Implanted 12.7 mm Teflon strip – "B"

Log N
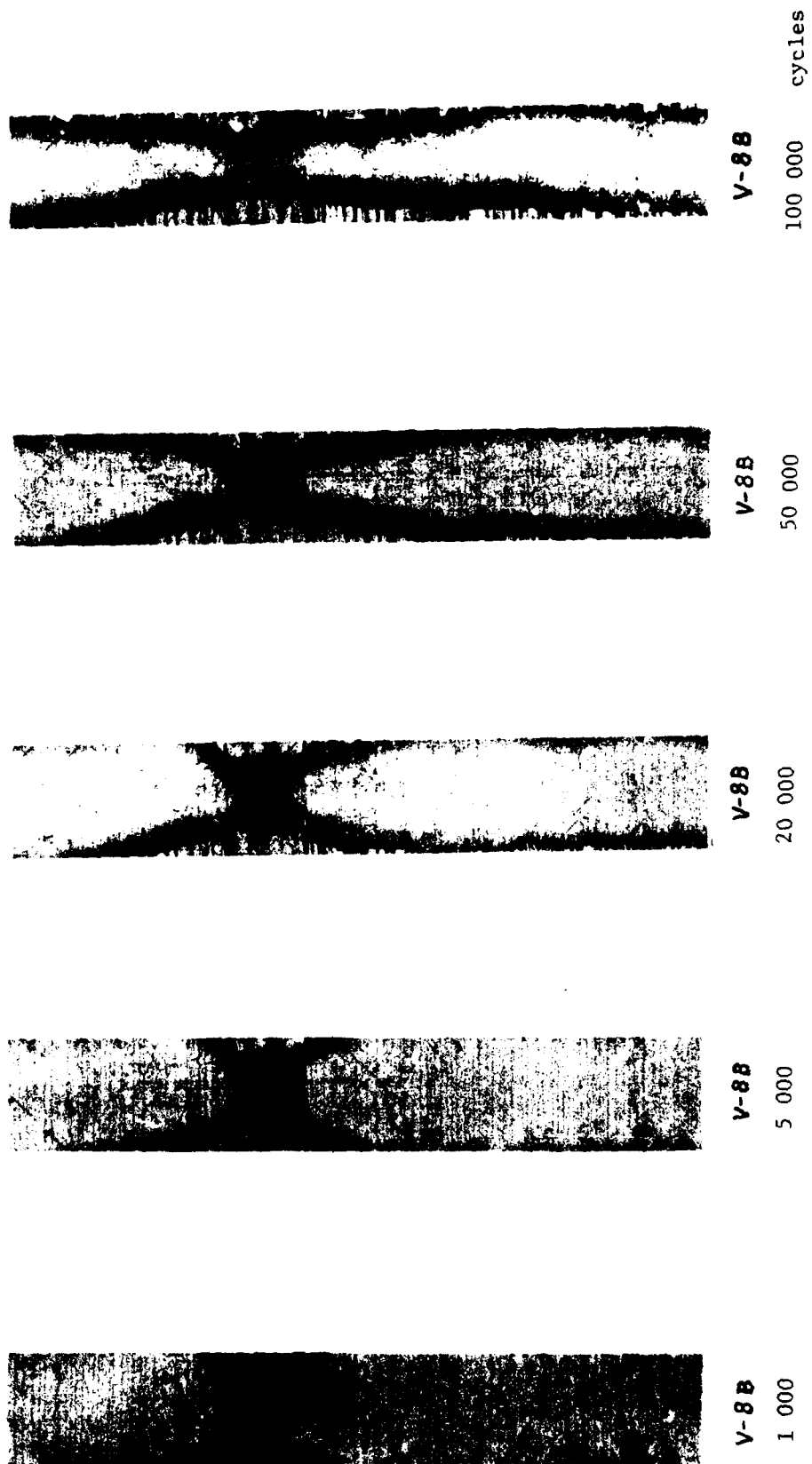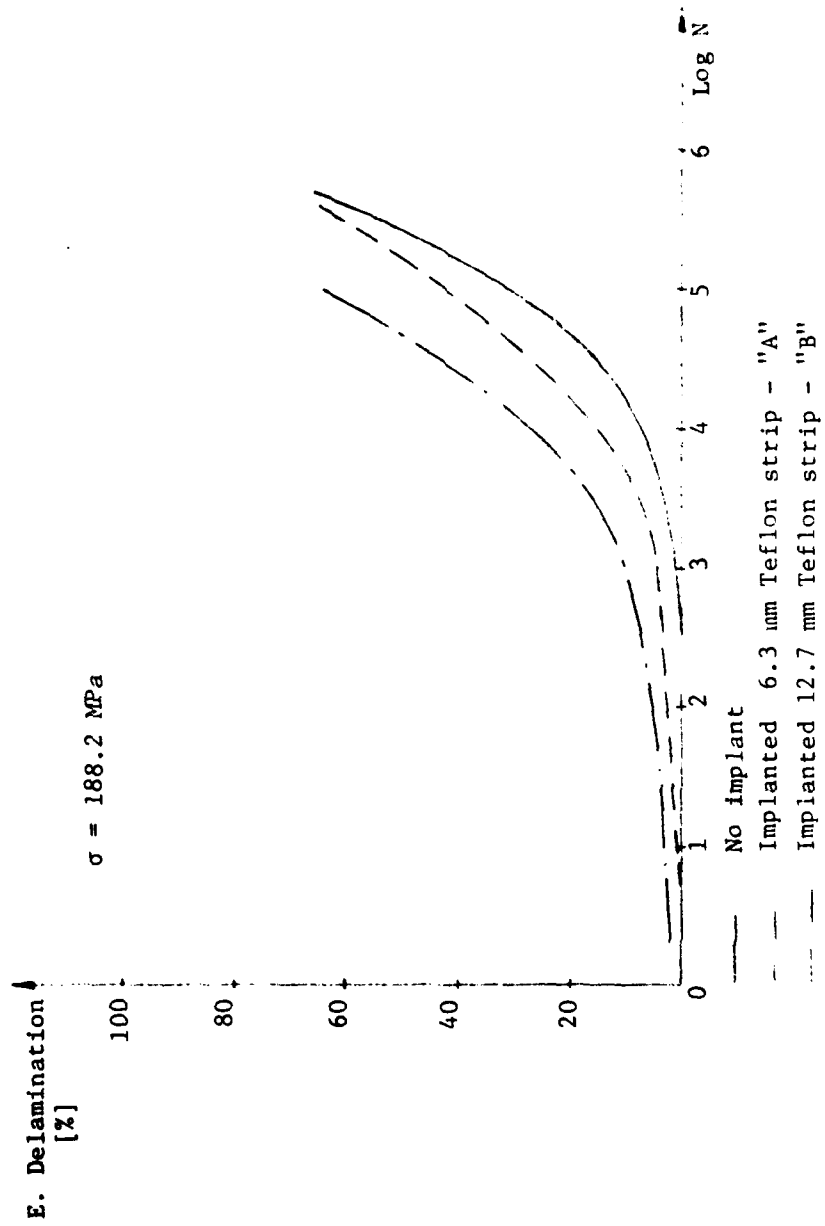
Figure 25. Effect of Implanted Interlaminar Flaw on Delamination Growth under Tension Fatigue Loading. $[\pm 45/0/90_2]_s$, type A and type B.

11-6 G
0

11-6 G
500
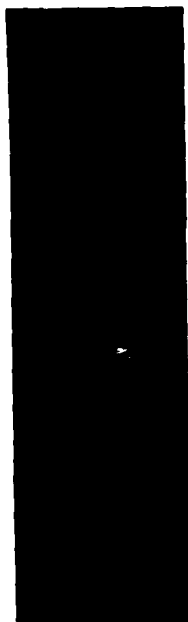
11-6 G
2 000   cycles

11-6 G
3 000

11-6 G
5 000

11-6 G
10 000   cycles

Figure 26.   Life-Sequence X-radiographs for $[0/90_2/45_2/-45_2]_s$
Laminate under 221 MPa Compression Fatigue Load.

107

11 - 6 G
20 000

11 - 6 G
50 000   cycles

11 - 6 G
100 000

11 - 6 G
130 703   cycles

Figure 26 Continued   108

Figure 27. Life-Sequence X-radiographs for $[0_2/90_2/45_2/-45_2]_s$-type A
Laminate under 221 MPa Compression Fatigue Load.

109

II-2A

2 110   cycles

Figure 27   Continued
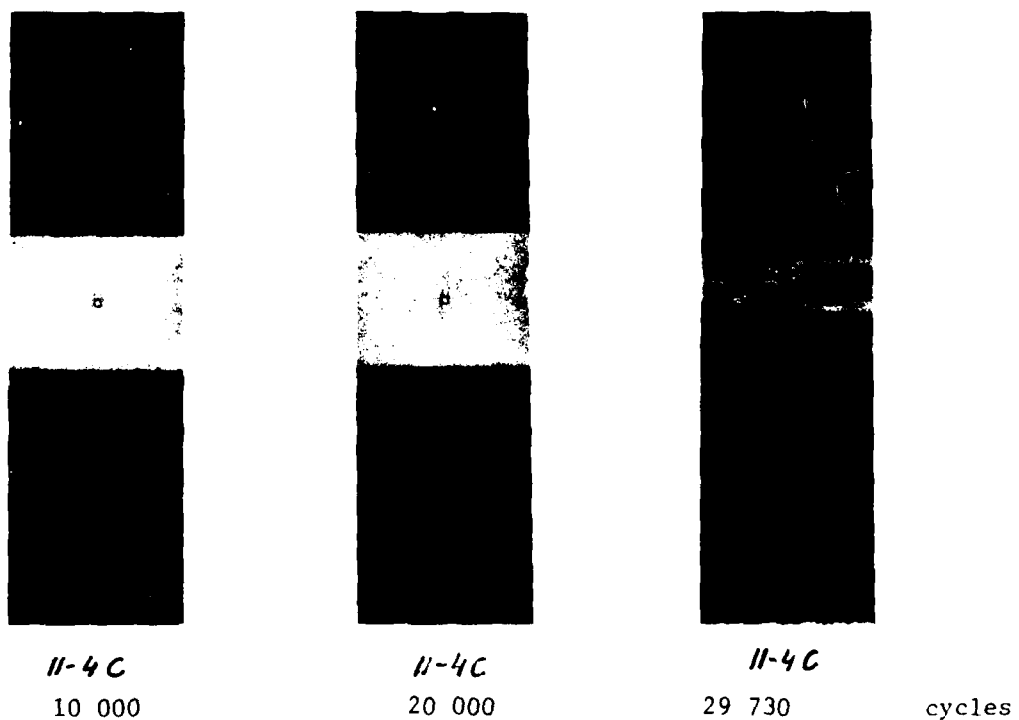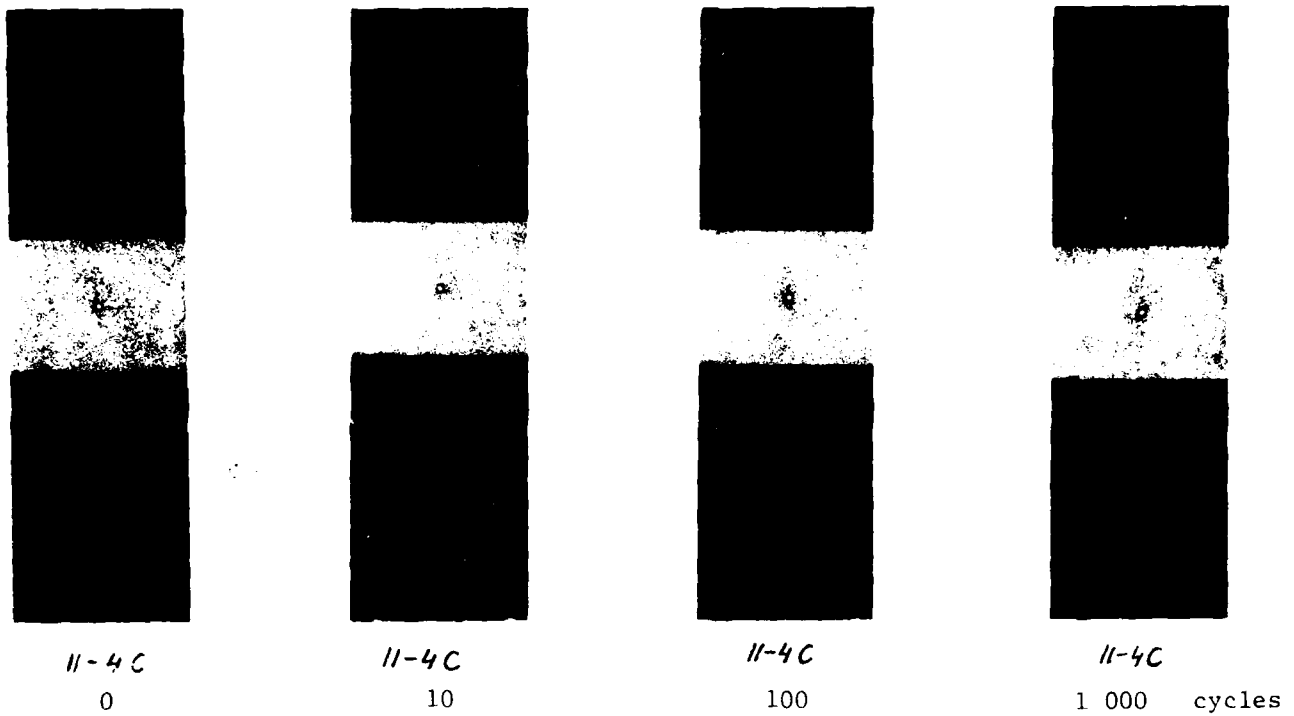
Figure 28. Life-Sequence X-radiographs for $[0_2/90_2/45_2/-45_2]_s$-type C
Laminate under 222 MPa Compression Fatigue Load.

111
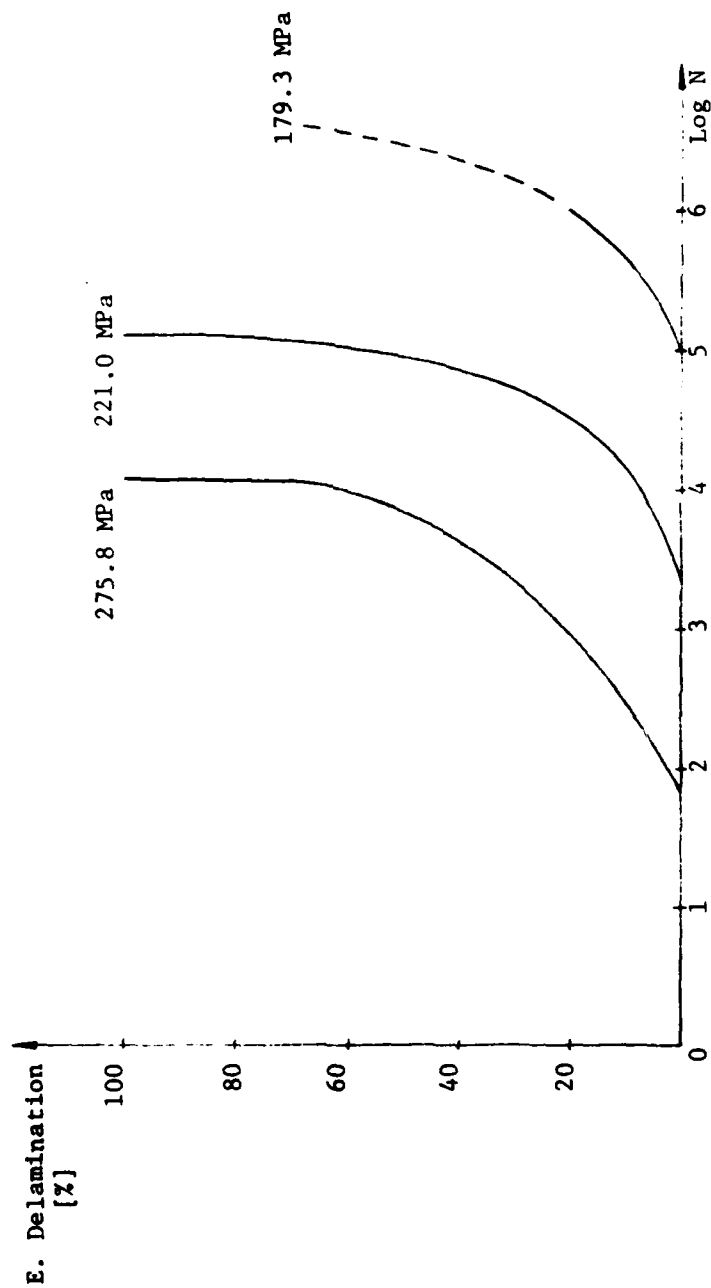
Figure 29. Edge Delamination Growth under Compression Fatigue $[0_2/90_2/45_2/-45_2]_s$
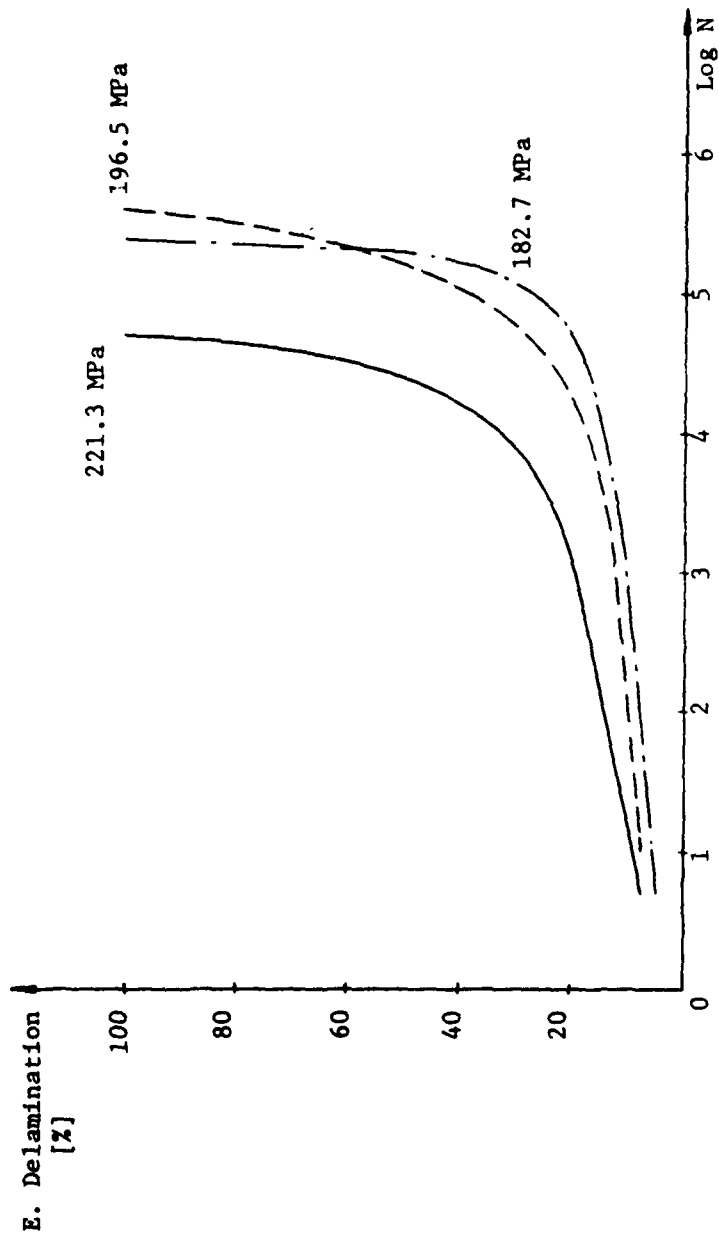
Figure 30. Edge Delamination Growth under Compression Fatigue $[0_2/90_2/45_2/-45_2]_s$ - type A
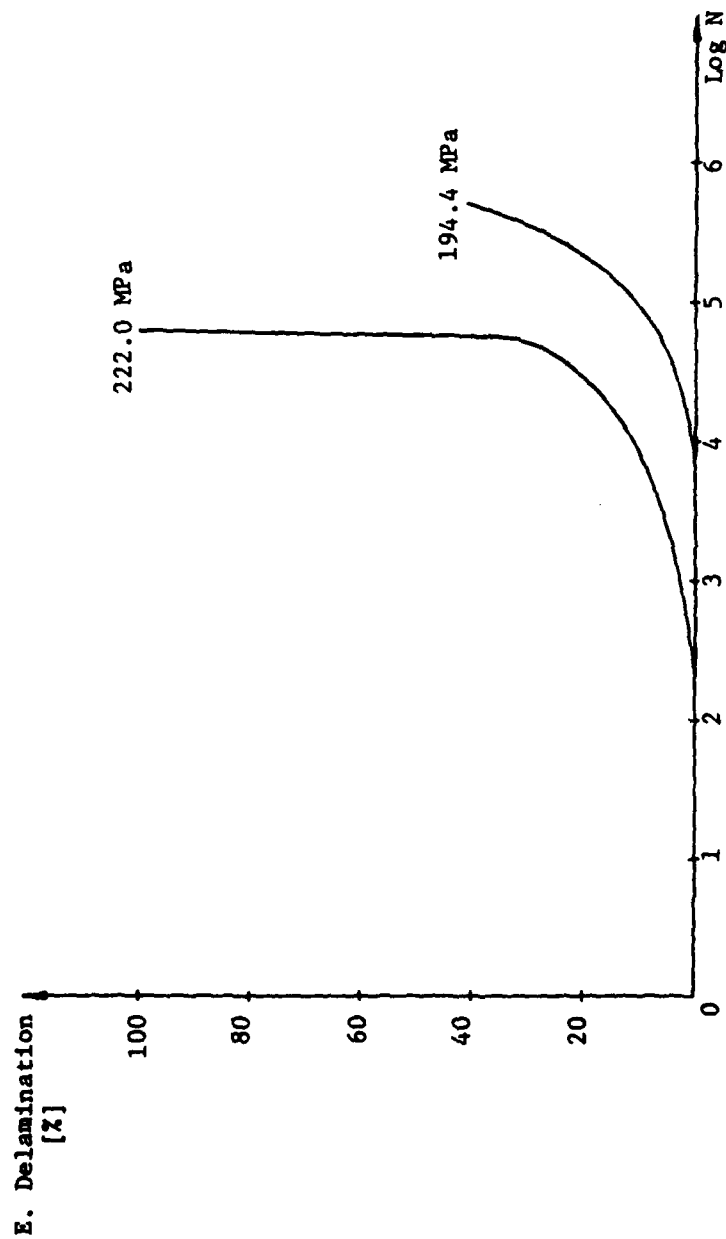
Figure 31. Edge Delamination Growth under Compression Fatigue $[0_2/90_2/45_2/-45_2]_s$ – type C.
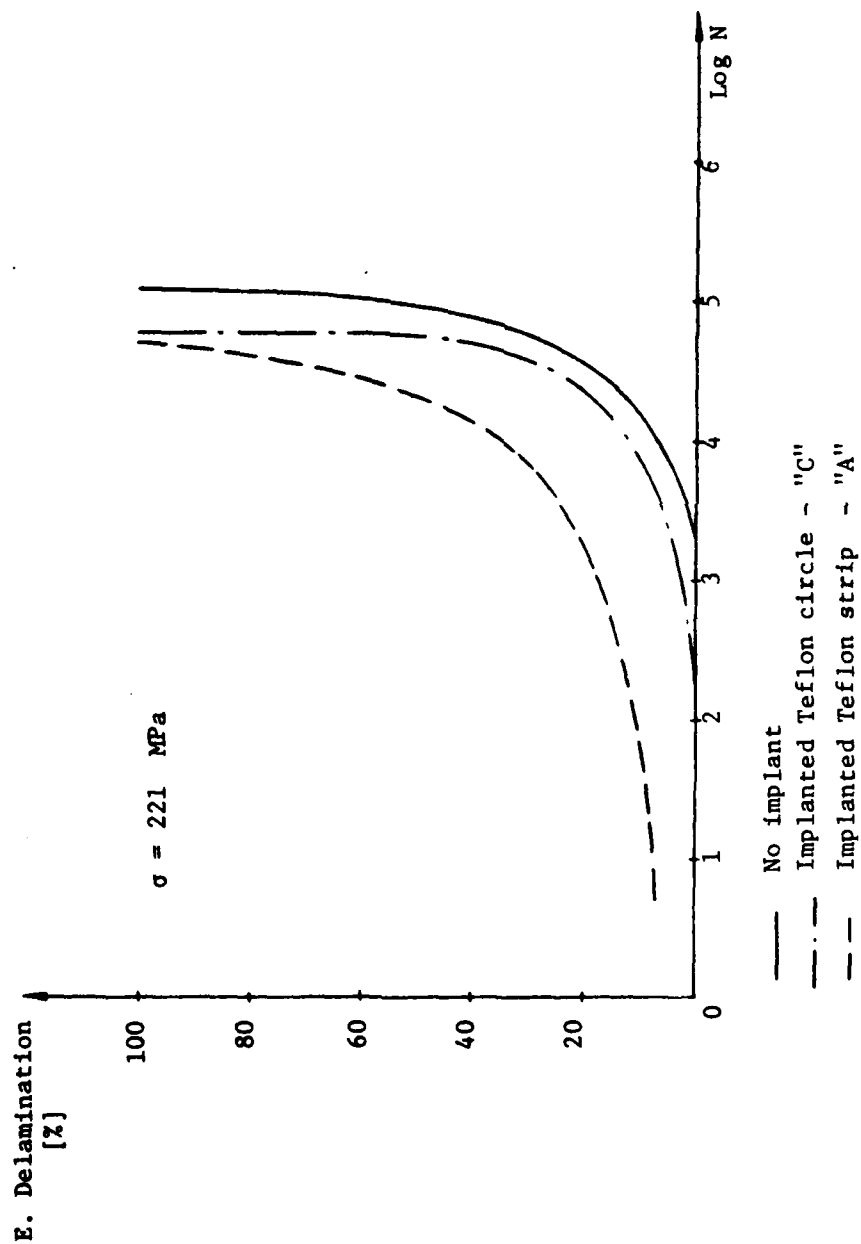
Figure 32. Effect of Implanted Interlaminar Flaw on Delamination Growth under Compression Fatigue Loading. $[0_2/90_2/45_2/-45_2]_s$, type A and type C.

$\overline{IV} - [0/90/0/90/45/-45/45/-45]_s$

| IV-5 | IV-5 | IV-5 | IV-5 |
| 0 | 500 | 1 000 | 2 000 cycles |
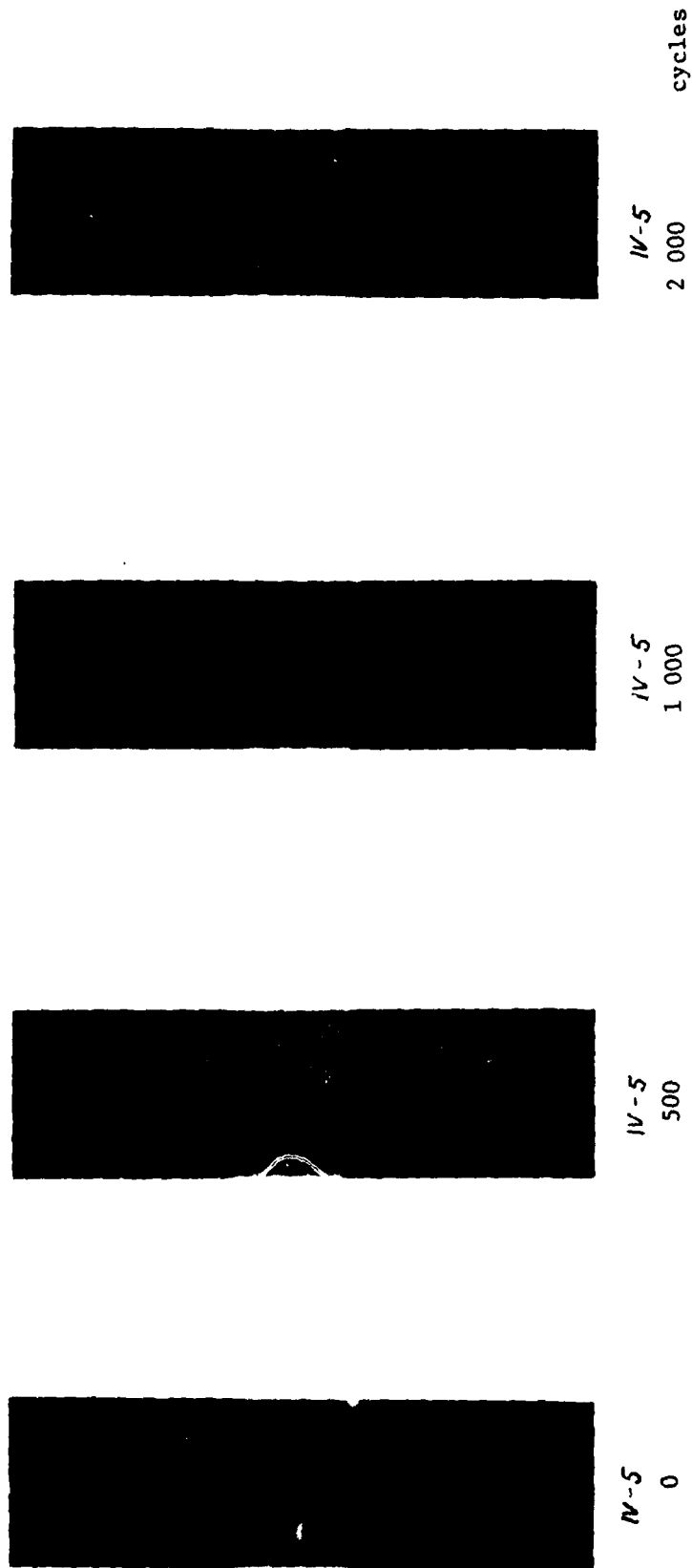
Figure 33. Life-Sequence X-radiographs for [0/90/0/90/45/-45/45/-45]$_s$ Laminate under 276 MPa Compression Fatigue Load.

116

IV-5
50 000   cycles

IV-5
20 000

IV-5
10 000

IV-5
5 000

Figure 33 Continued

117

IV-5
748 322
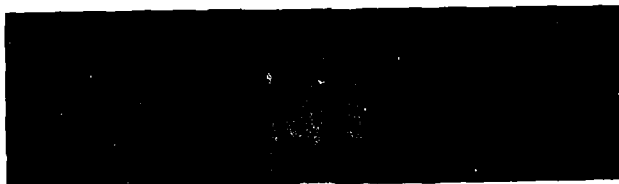
IV-5
500 000

IV-5
200 000

IV-5
100 000

cycles

Figure 33   Continued

IV-4A
0

IV-4A
10

IV-4A
1 000   cycles

IV-4A
10 000

IV-4A
10 000

IV-4A
40 000   cycles

Figure 34.   Life-Sequence X-radiographs for $[0/90/0/90/45/-45/45/-45]_s$-A
Laminate under 219 MPa Compression Fatigue Load.

119

IV-4A

100 000

IV-4A

300 000   cycles

Figure 34   Continued
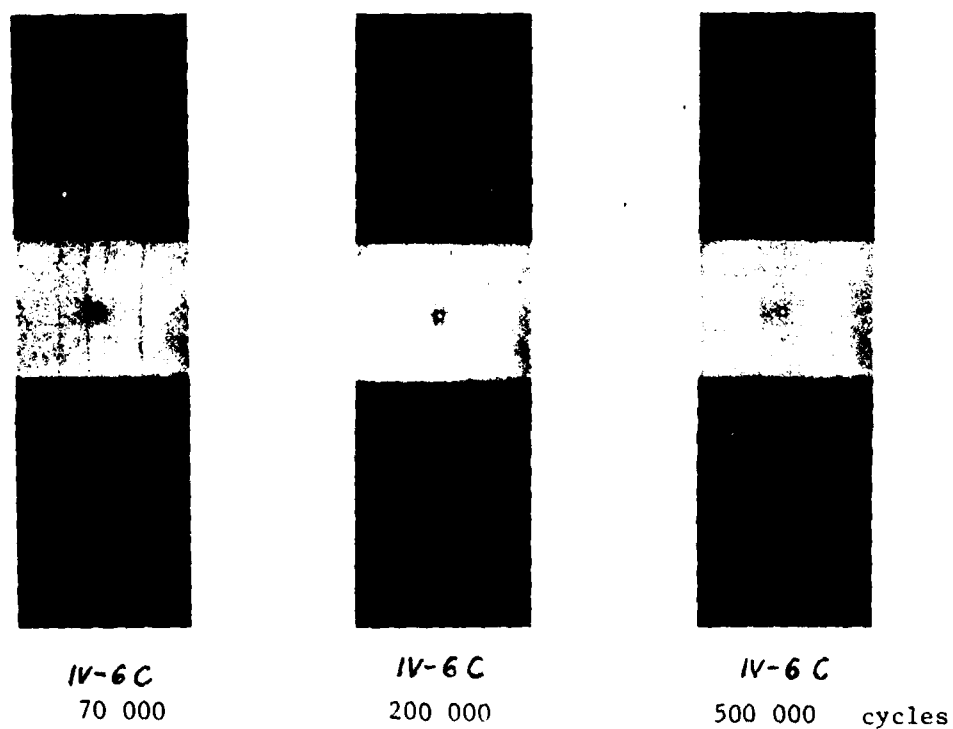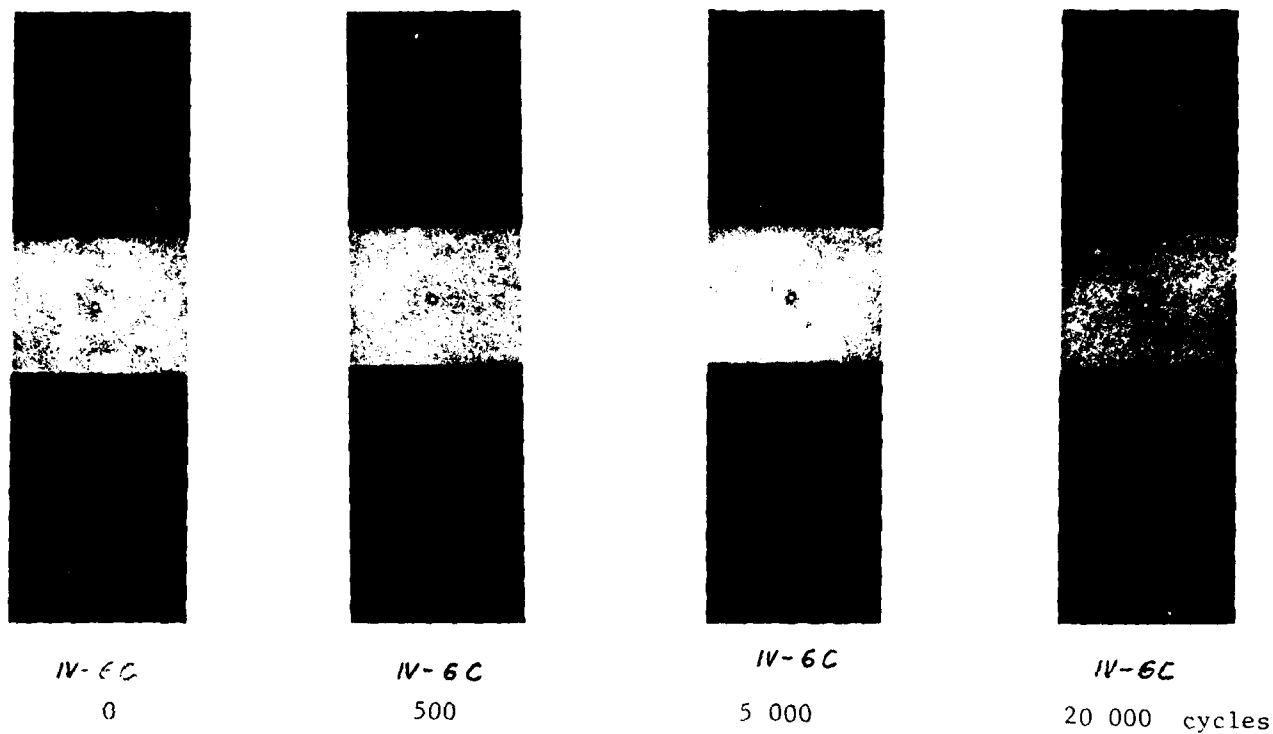
Figure 35. Life-Sequence X-radiographs for [0/90/0/90/45/-45/45/-45]$_s$- C
Laminate under 219 MPa Compression Fatigue Load.

121
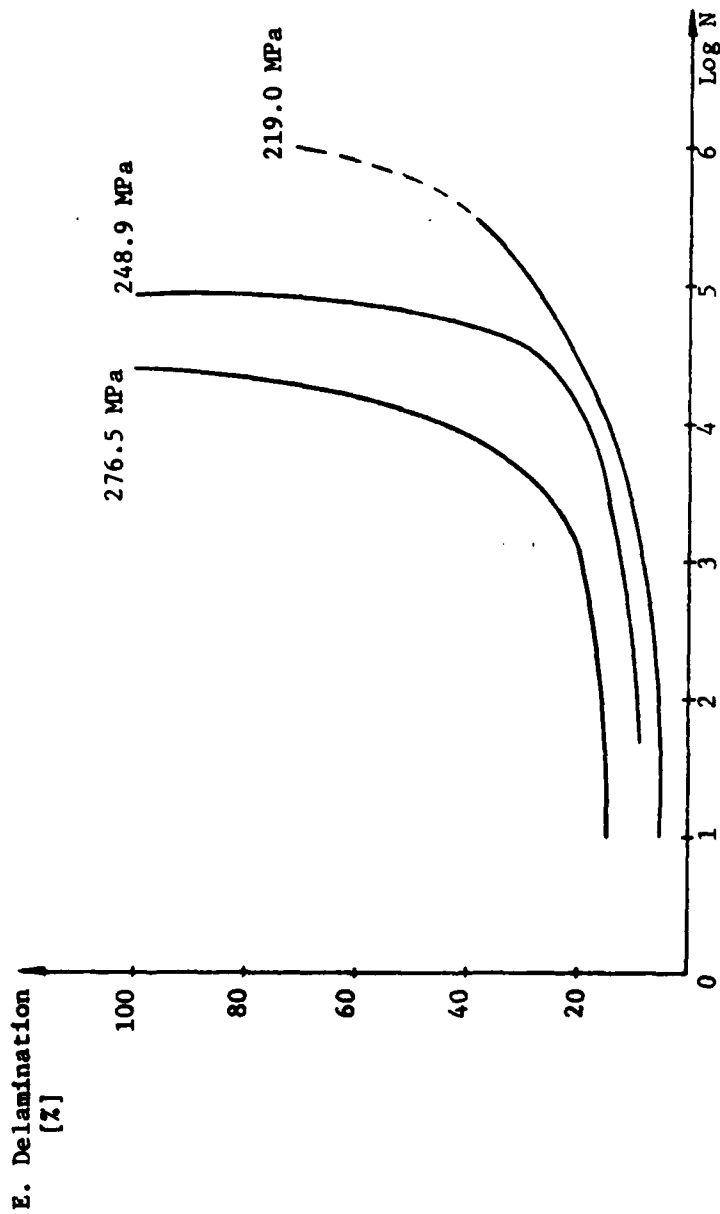
Figure 36. Edge Delamination Growth under Compression Fatigue Loading [0/90/0/90/45/-45/45/-45]$_s$ - type A.

E. Delamination [%]

$\sigma = 275.8$ MPa

—— $[0_2/90_2/45_2/-45_2]_s$ laminate

— — $[0/90/0/90/45/-45/45/-45]_s$ laminate
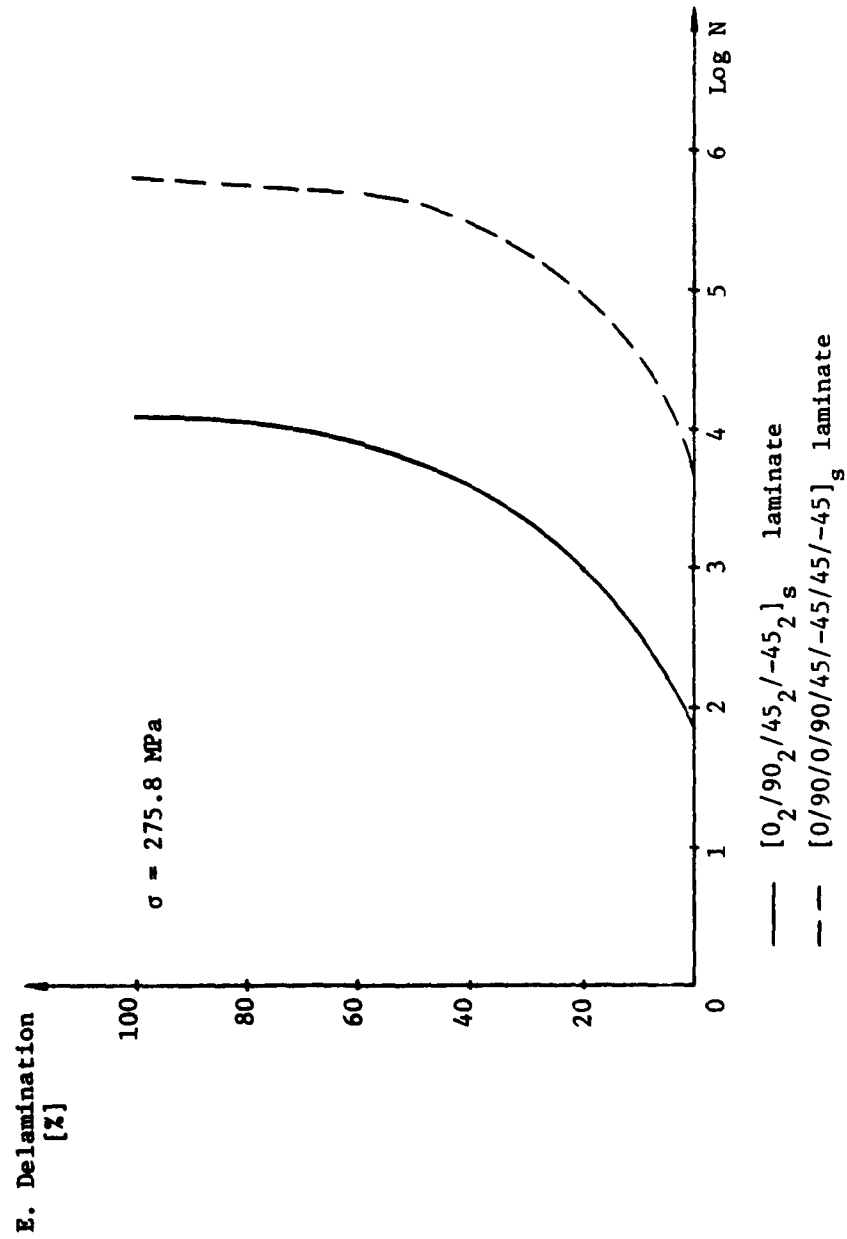
Figure 37. Effect of Ply Thickness on Delamination Growth under Compression Fatigue.

123
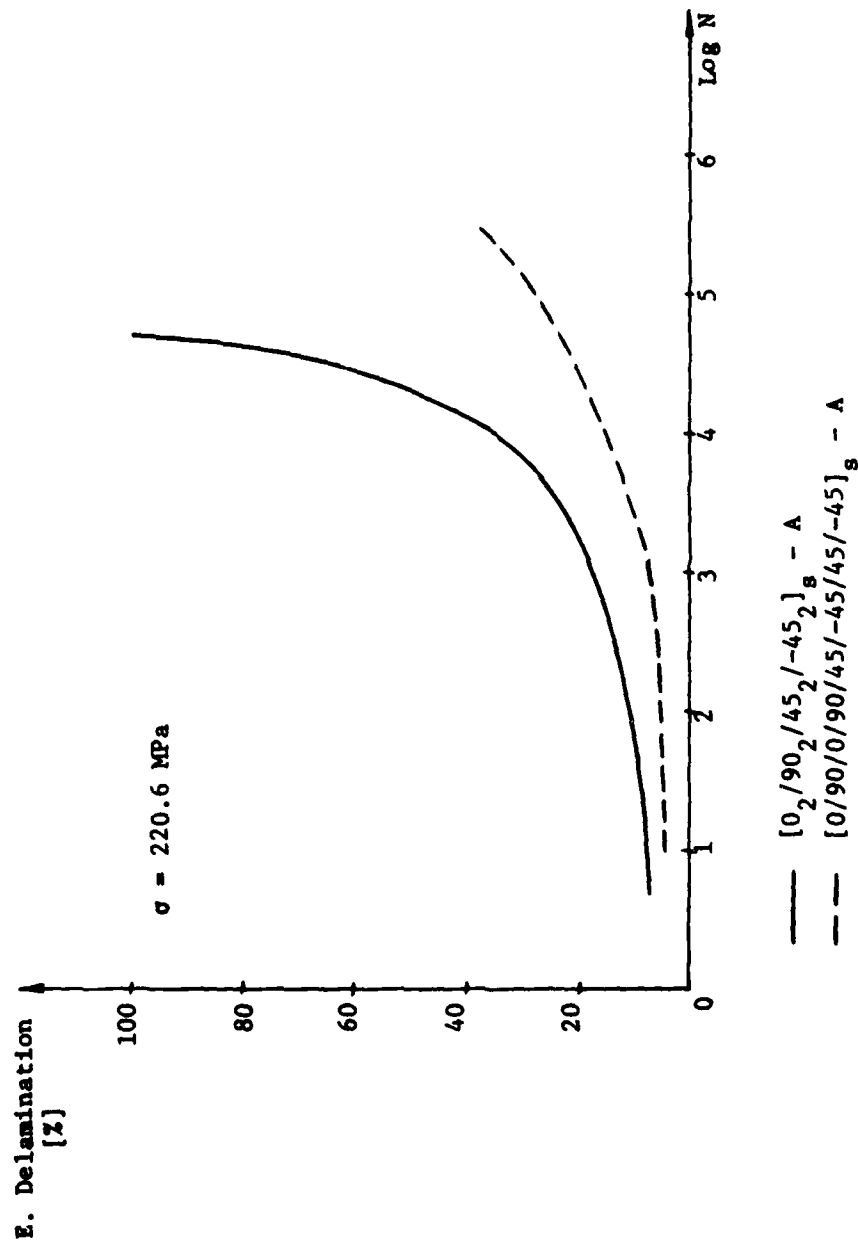
Figure 38. Effect of Ply Thickness on Delamination Growth under Compression Fatigue for type A Specimens
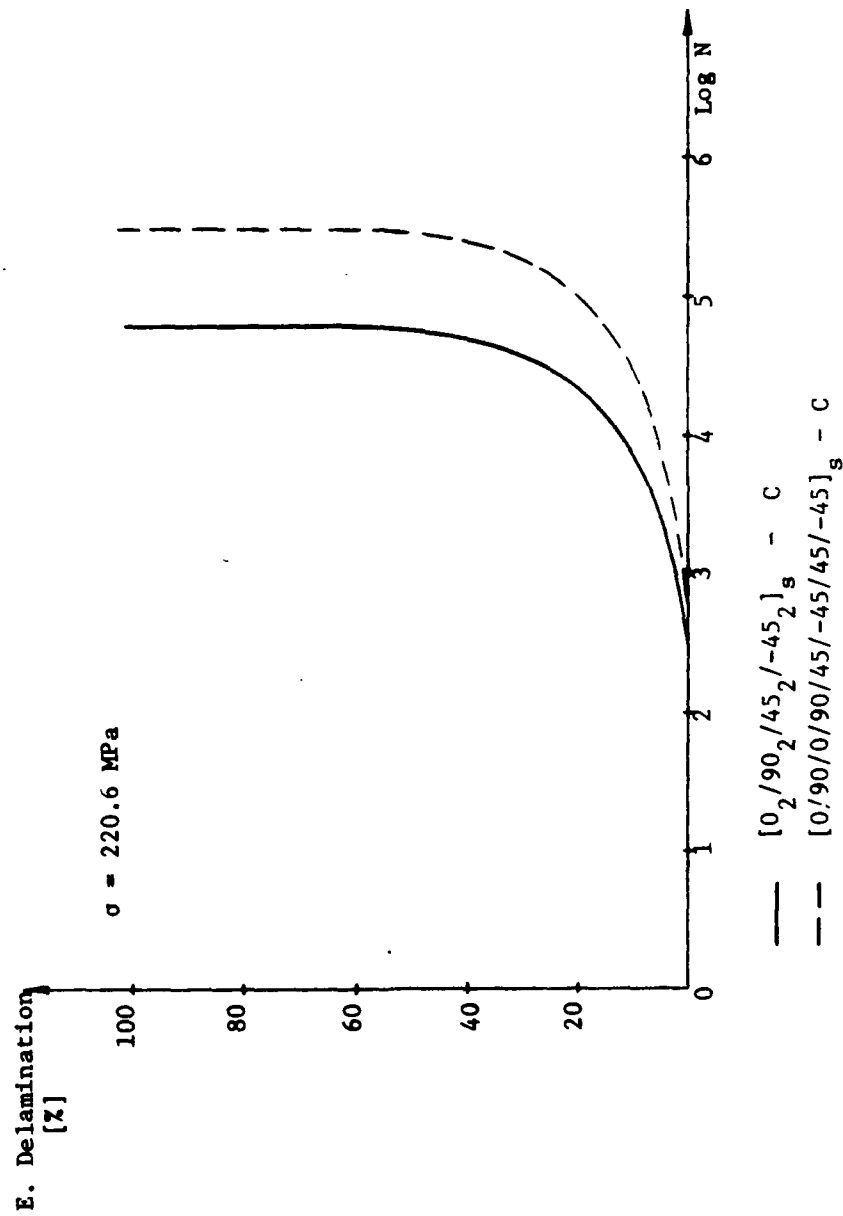
Figure 39. Effect of Ply Thickness on Delamination Growth under Compression Fatigue for type C specimens.

$\sigma = 220.6$ MPa

E. Delamination [%]

$[0_2/90_2/45_2/-45_2]_s - C$

$[0/90/0/45/-45/45/-45]_s - C$

Log N
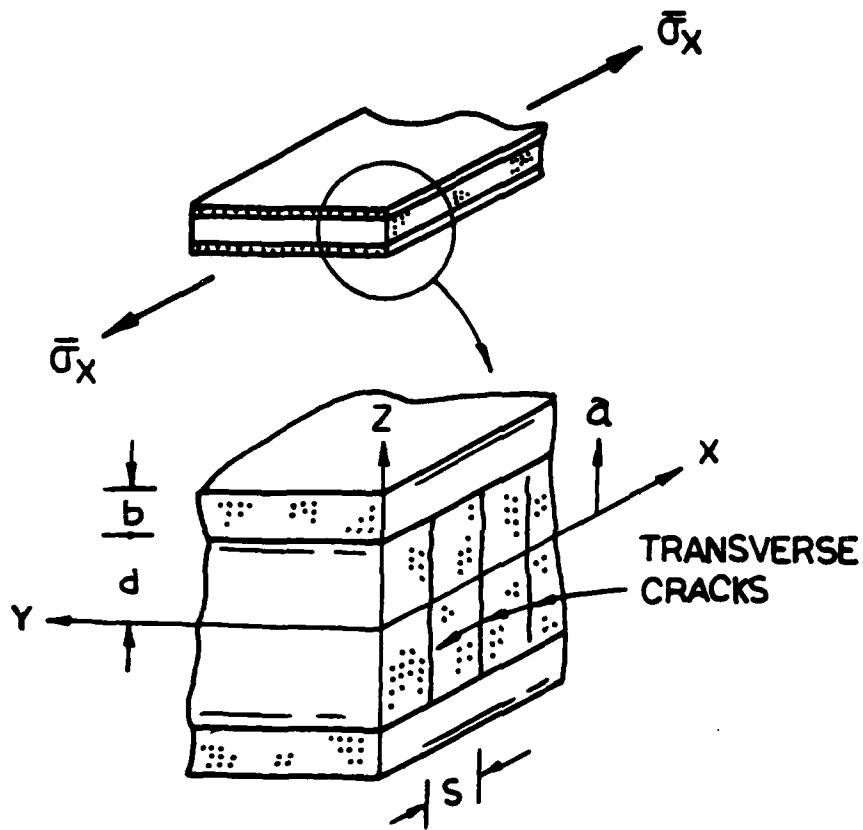
Figure 40. Schematics of 90°-Cracking
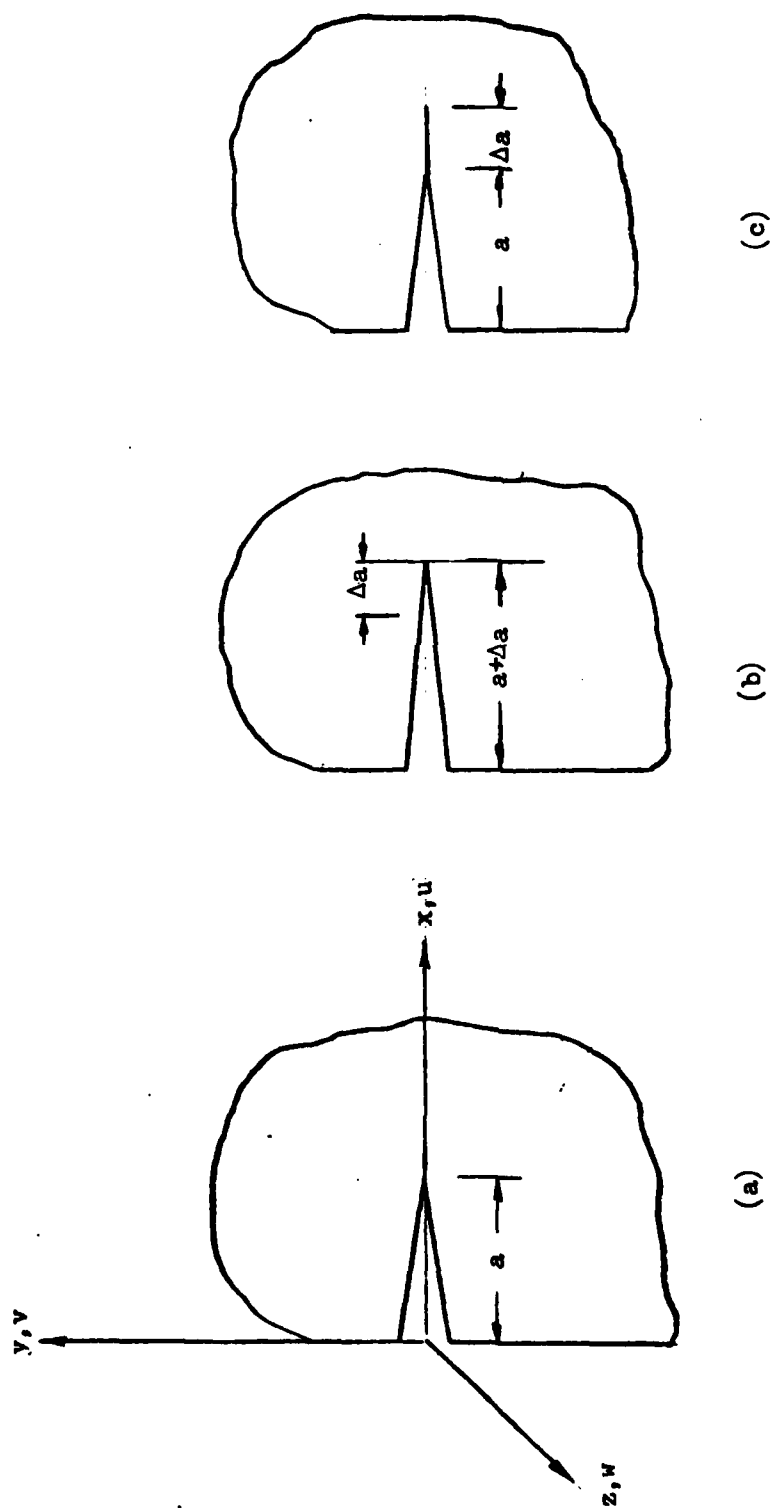
Figure 41. Schematic of Irwin's Crack-Closure Representation.
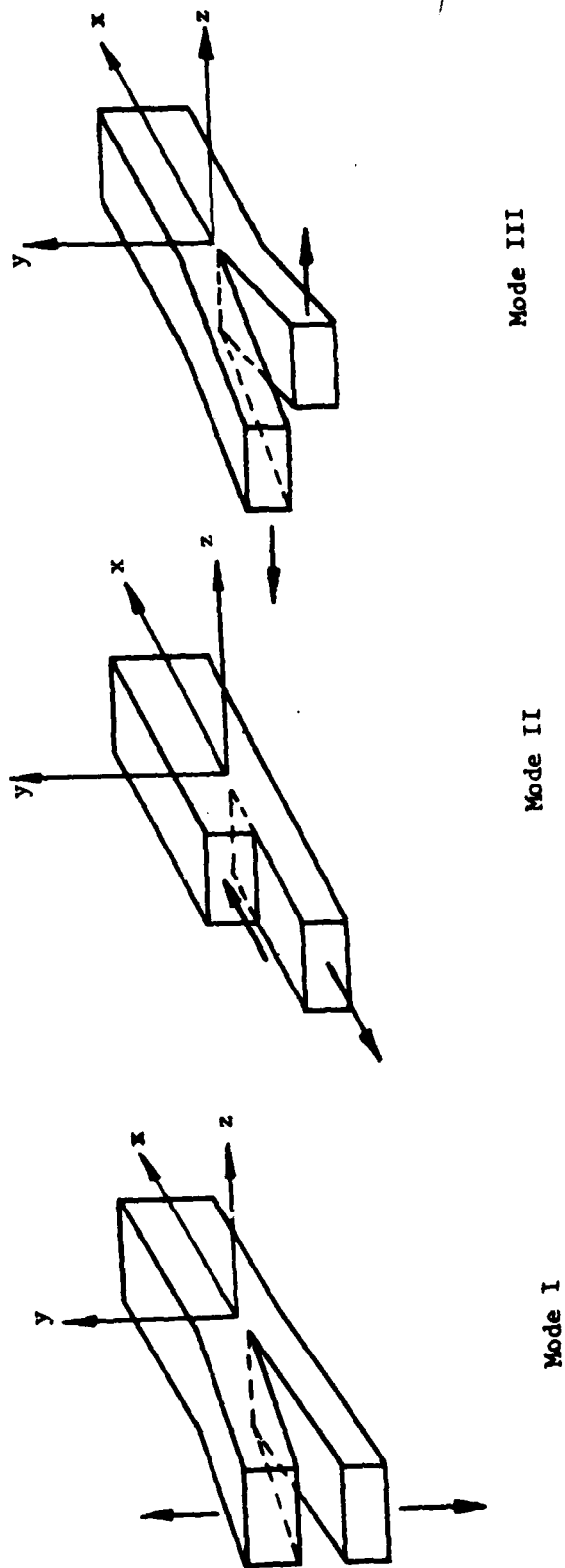
Figure 42.   The Three Crack Extension Modes.
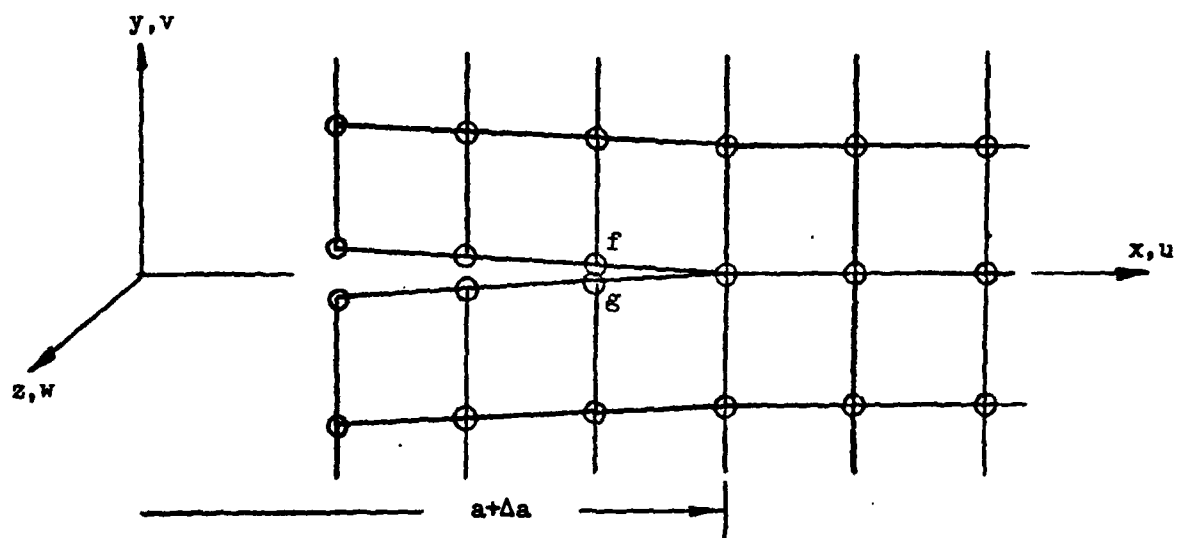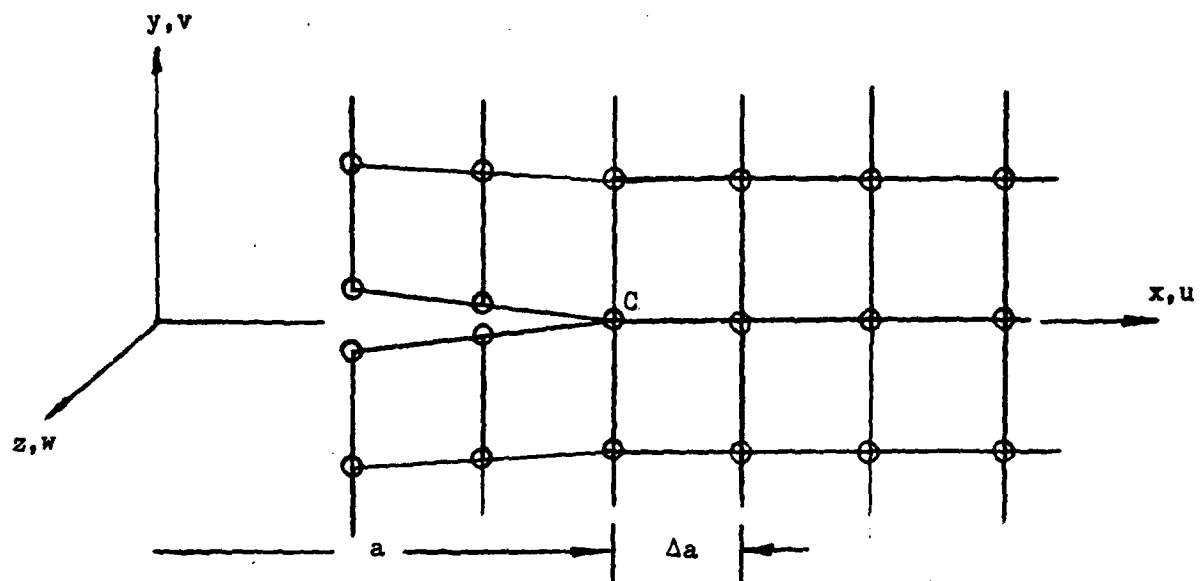
Figure 43. Finite Element Scheme of Irwin's Crack-Closure
Representation.
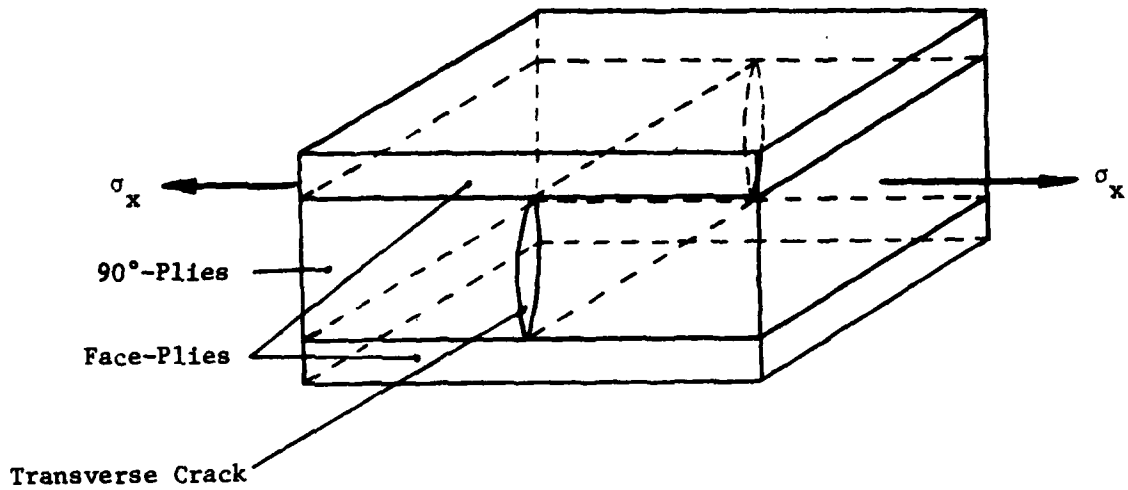
(a)   Single Transverse Crack Geometry
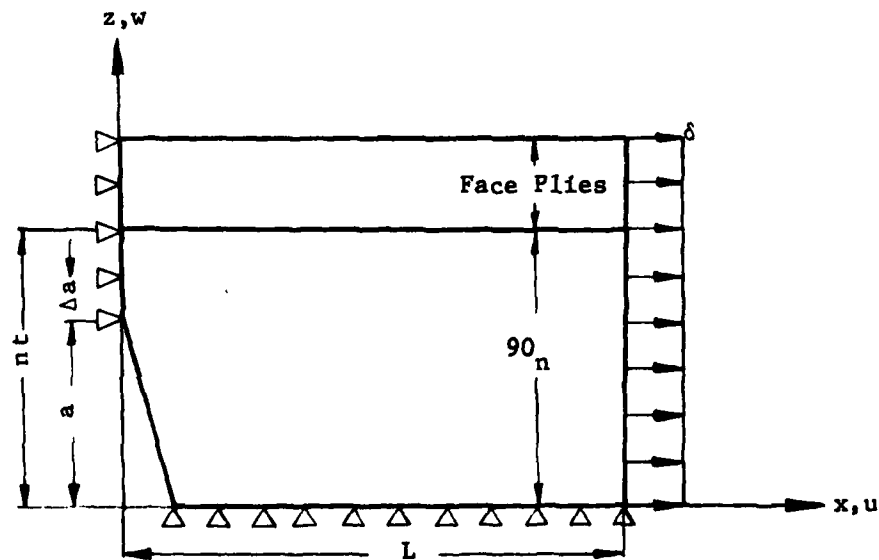
(b) Single Transverse Crack Finite Element Model

Figure 44.   Finite Element Representation of A Transverse Crack.

130
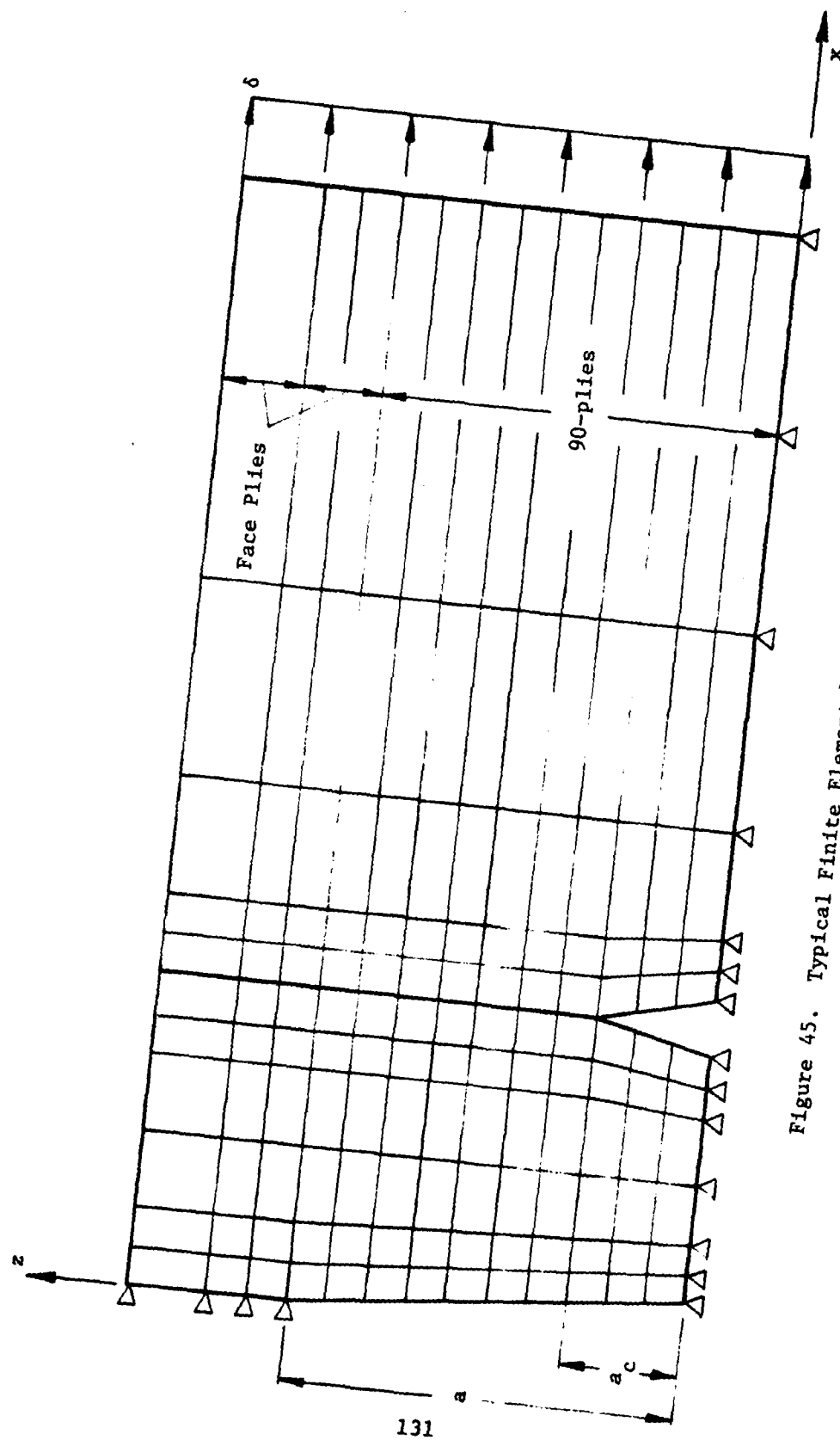
Figure 45. Typical Finite Element Mesh for Transverse Cracks.
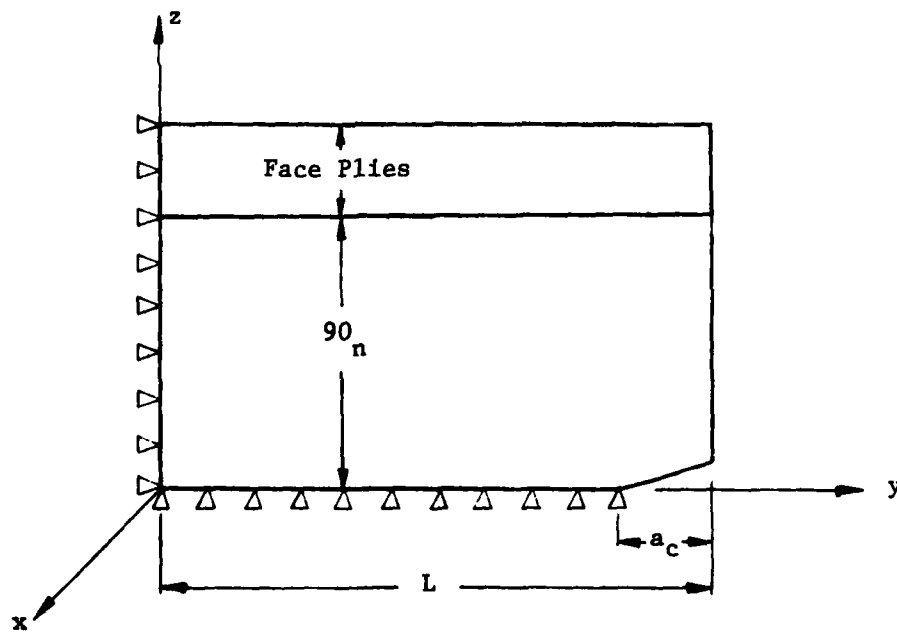
131
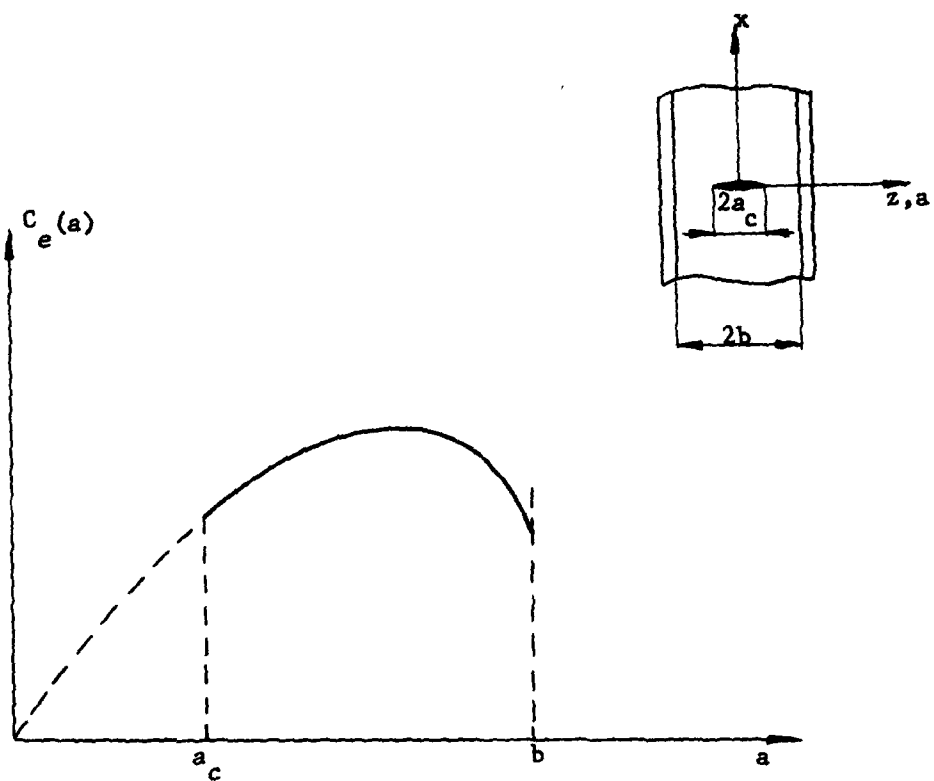
Figure 46. Typical $C_e(a)$ Curve for Transverse Crack
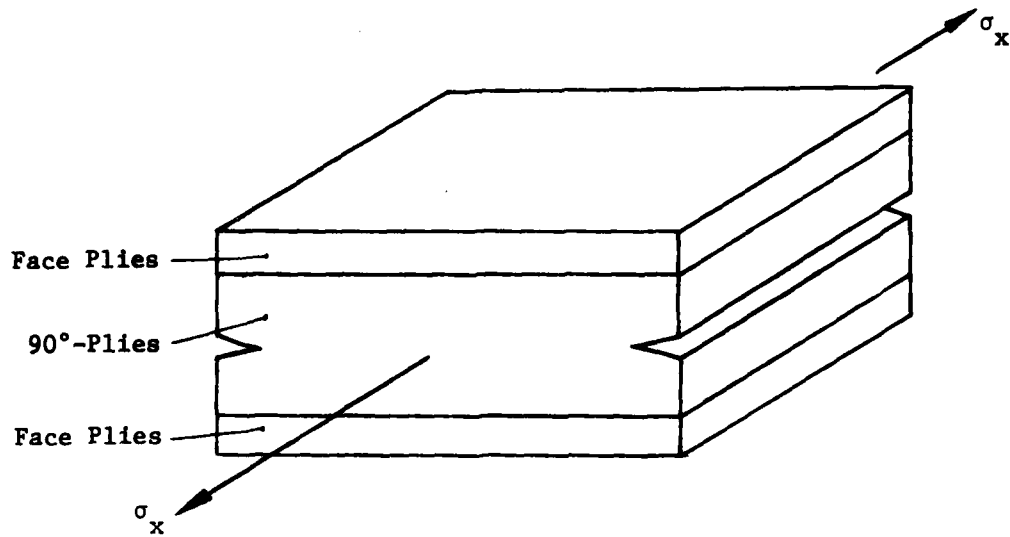
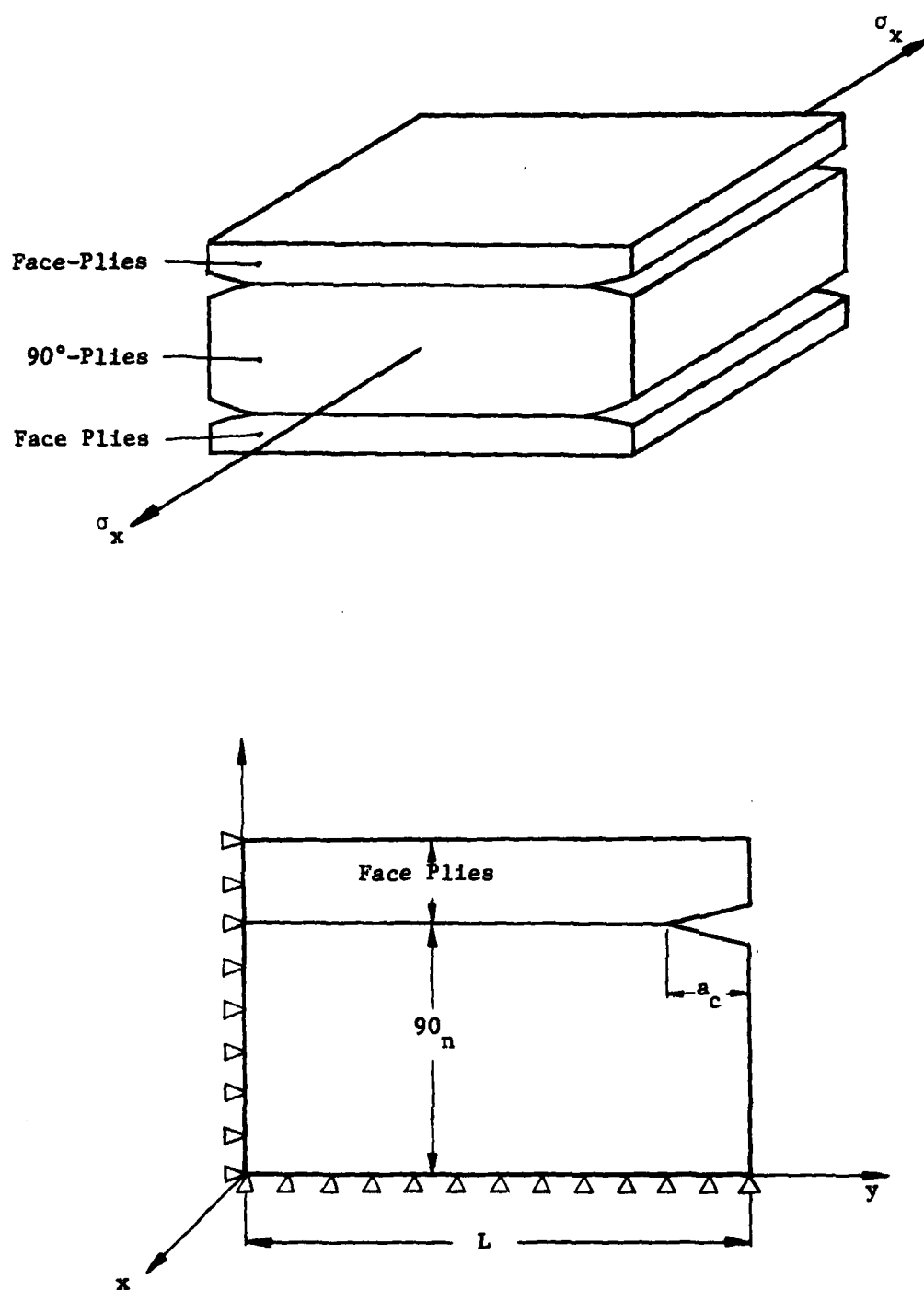Figure 47. Finite Element Model for Mid-plane Free-Edge Delamination

133

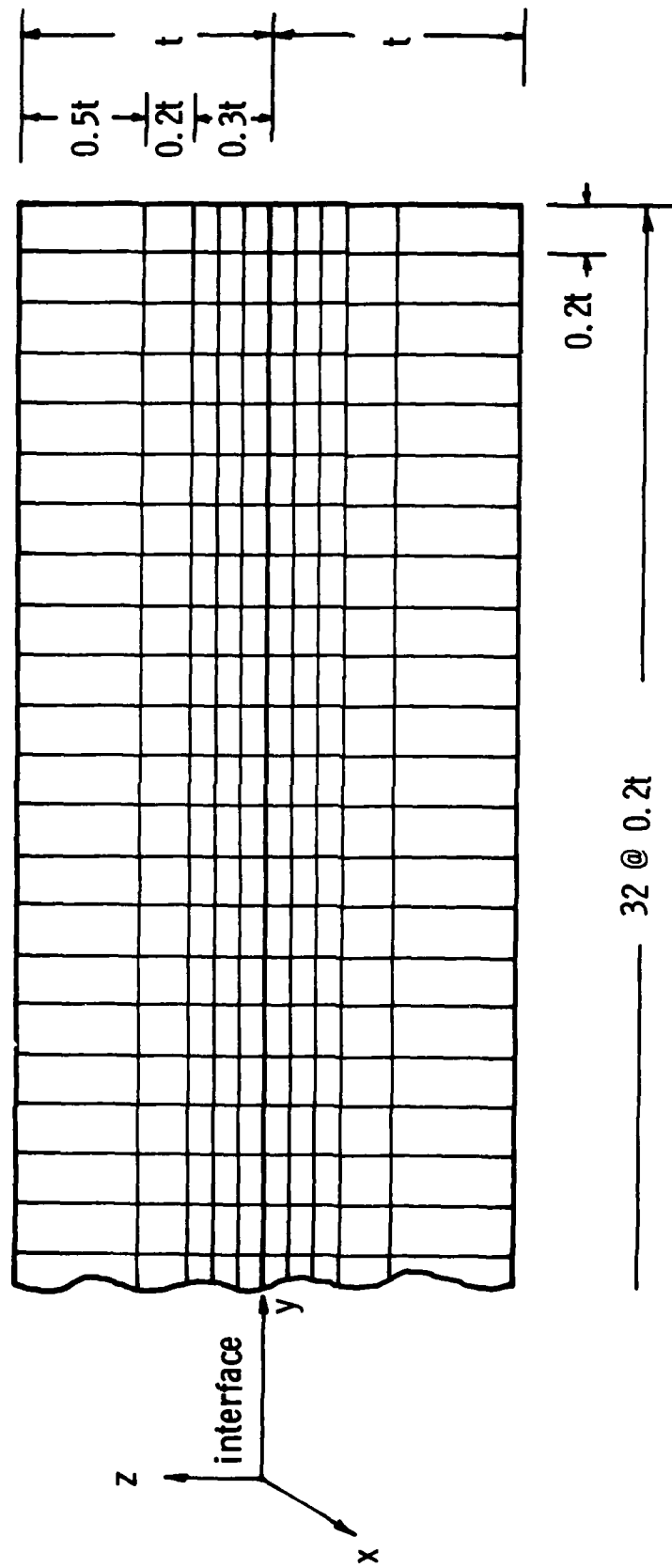Figure 48. Finite Element Model for Interface Free-Edge Delamination

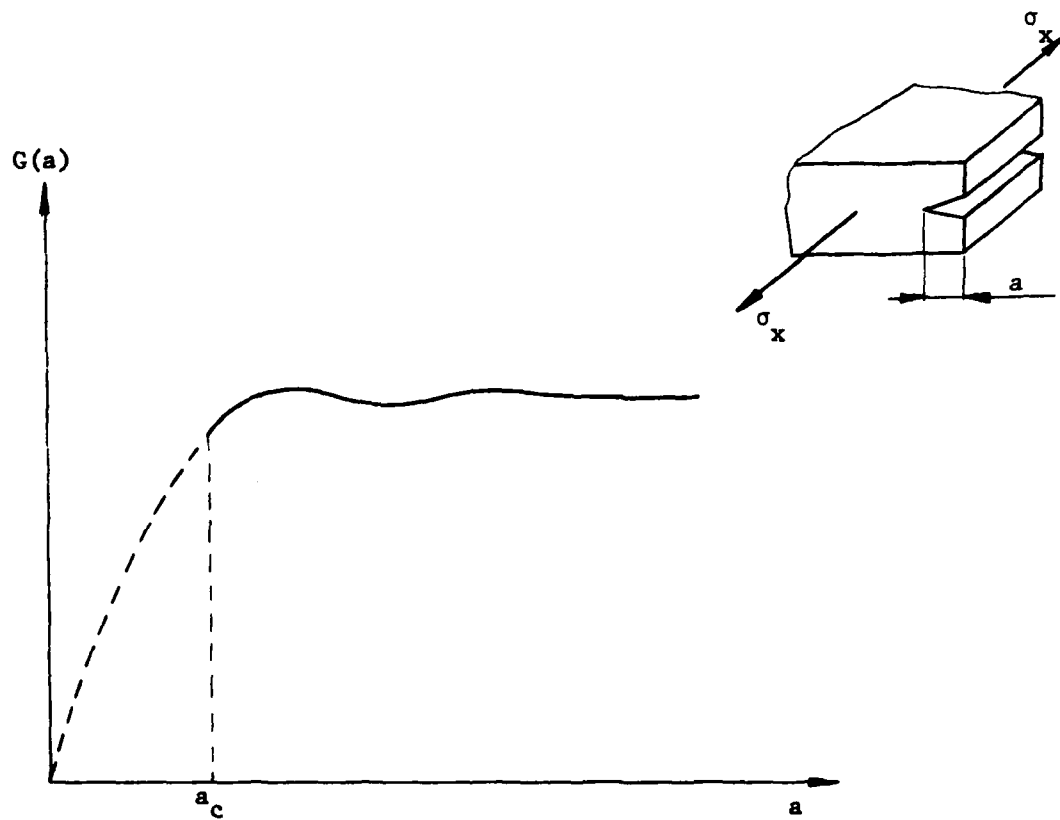Figure 49. Typical Finite Element Mesh for Free Edge Delamination

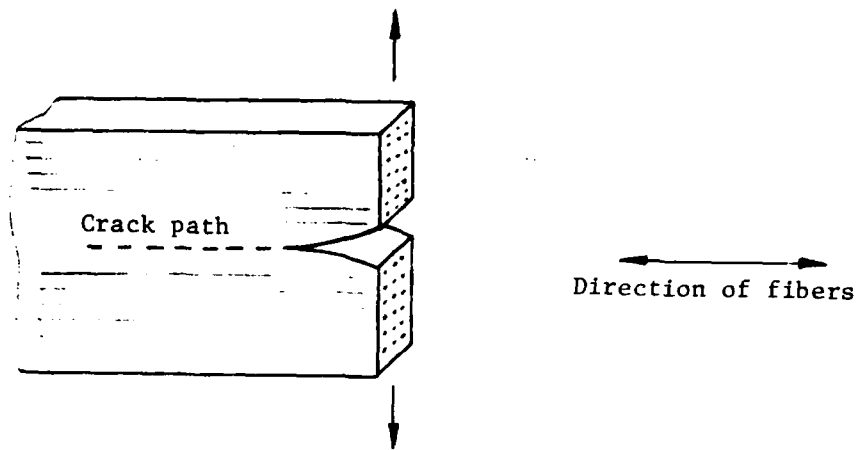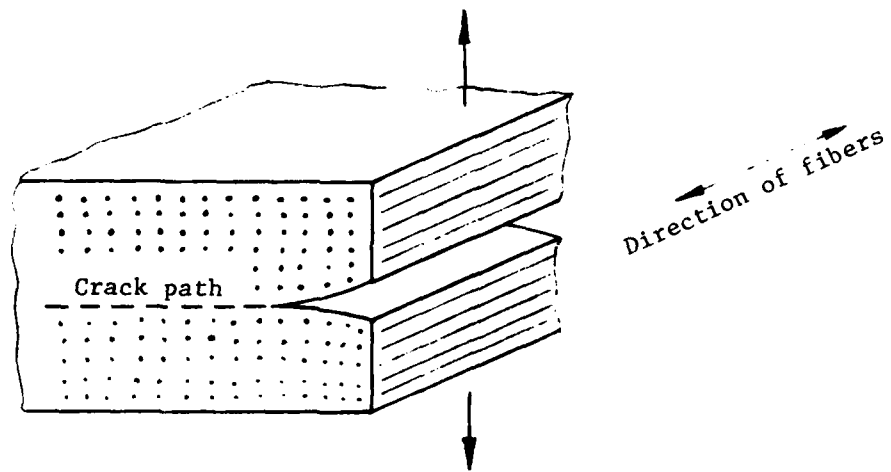Figure 50. Typical G(a) for Edge Delamination.

(a) 0°/0° Delamination Action

(b) Transverse Cracking Action

Figure 51. Schematics of Two Different Cracking Actions in Unidirectional Laminate.
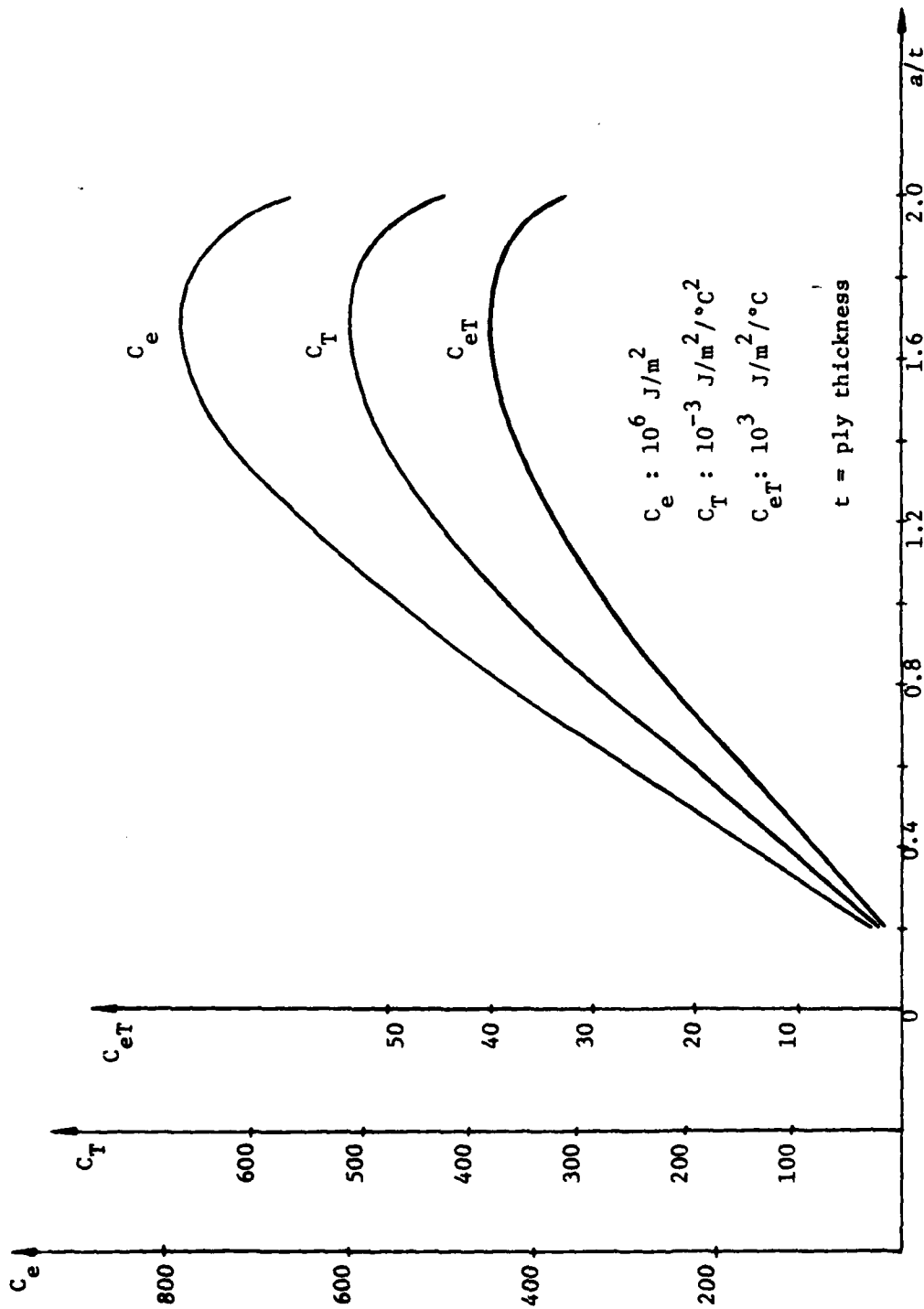
137

Figure 52. Transverse Cracking Coefficient Functions for $[\pm 45/0/90_2]_s$ Laminate under Uniaxial Tension and Uniform Thermal Loading
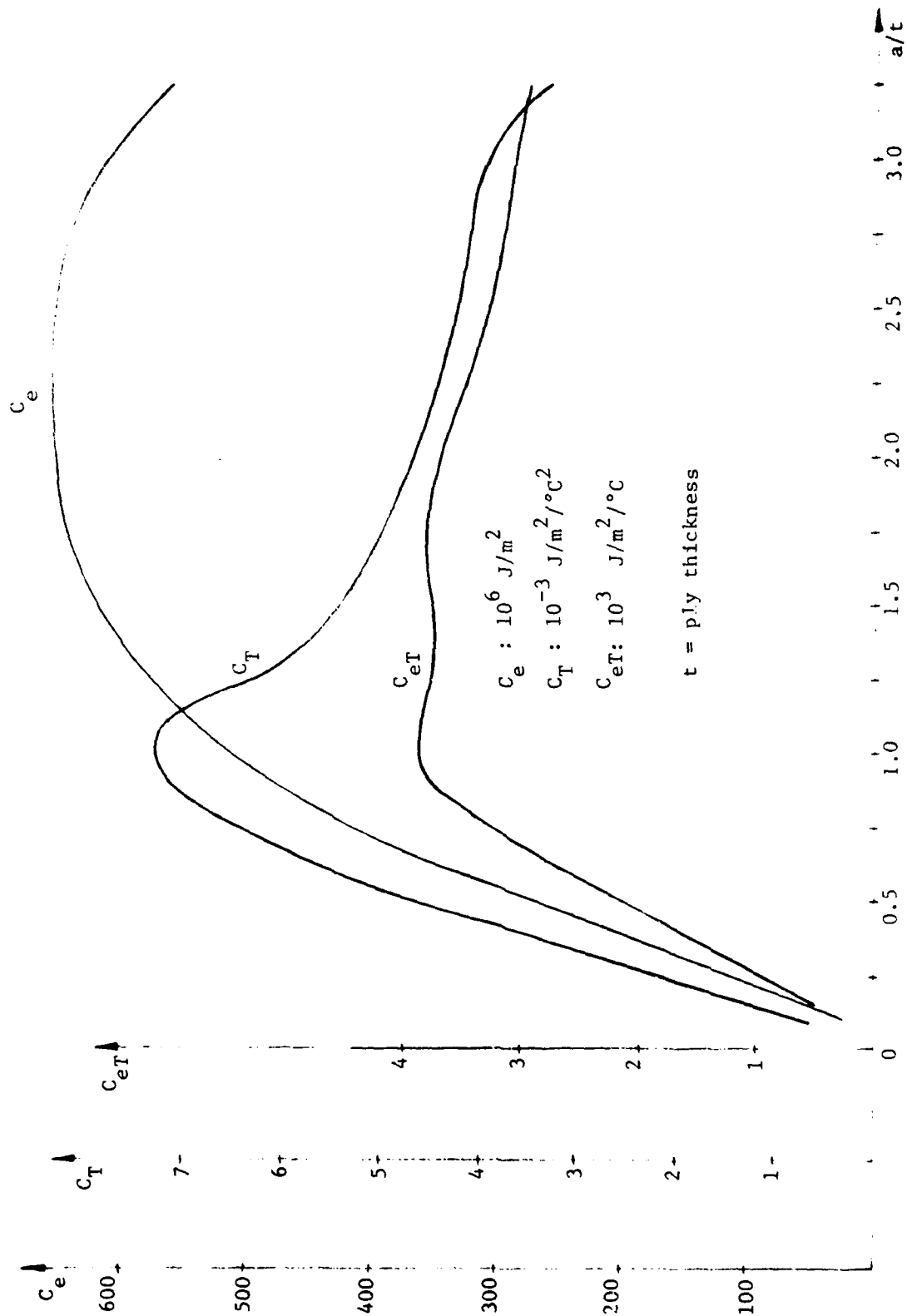
138

Figure 53. Mid-plane (mode I) Delamination Coefficient Functions for $[\pm 45/\rho/90_2]_s$ Laminate under Uniaxial Tension and Uniform Thermal Loading.

C_e : 10^6 J/m^2

C_T : 10^{-3} $J/m^2/°C^2$

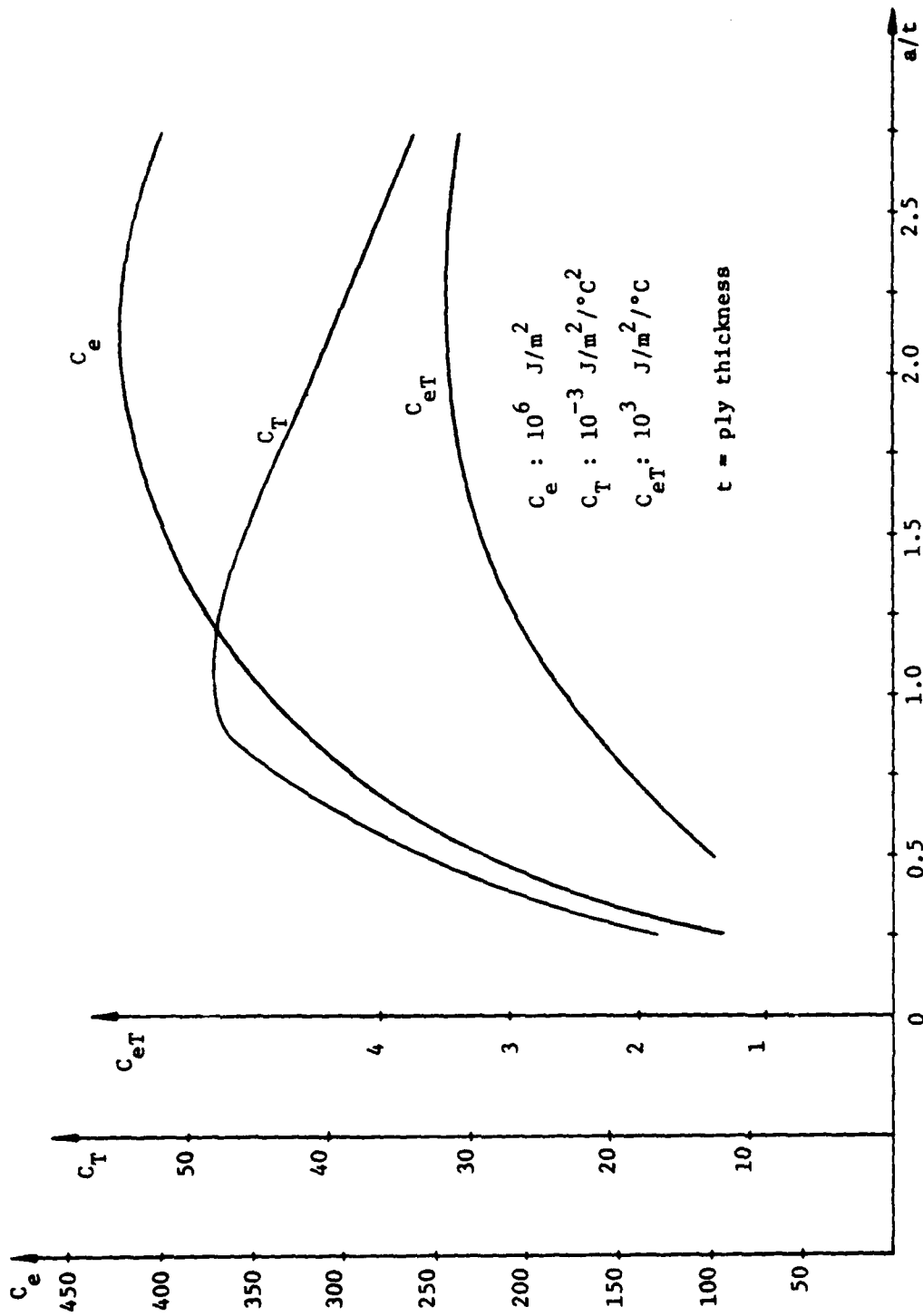C_{eT}: 10^3 $J/m^2/°C$

t = ply thickness

Figure 54. Off-Mid-plane (0/90) Delamination Coefficient Functions for $[\pm 45/0/90_2]_s$ Laminate under Uniaxial Tension and Uniform Thermal Loading.

Figure 55.   Transverse Cracking Coefficient Functions for $[0_2/90_2/45_2/-45_2]_s$
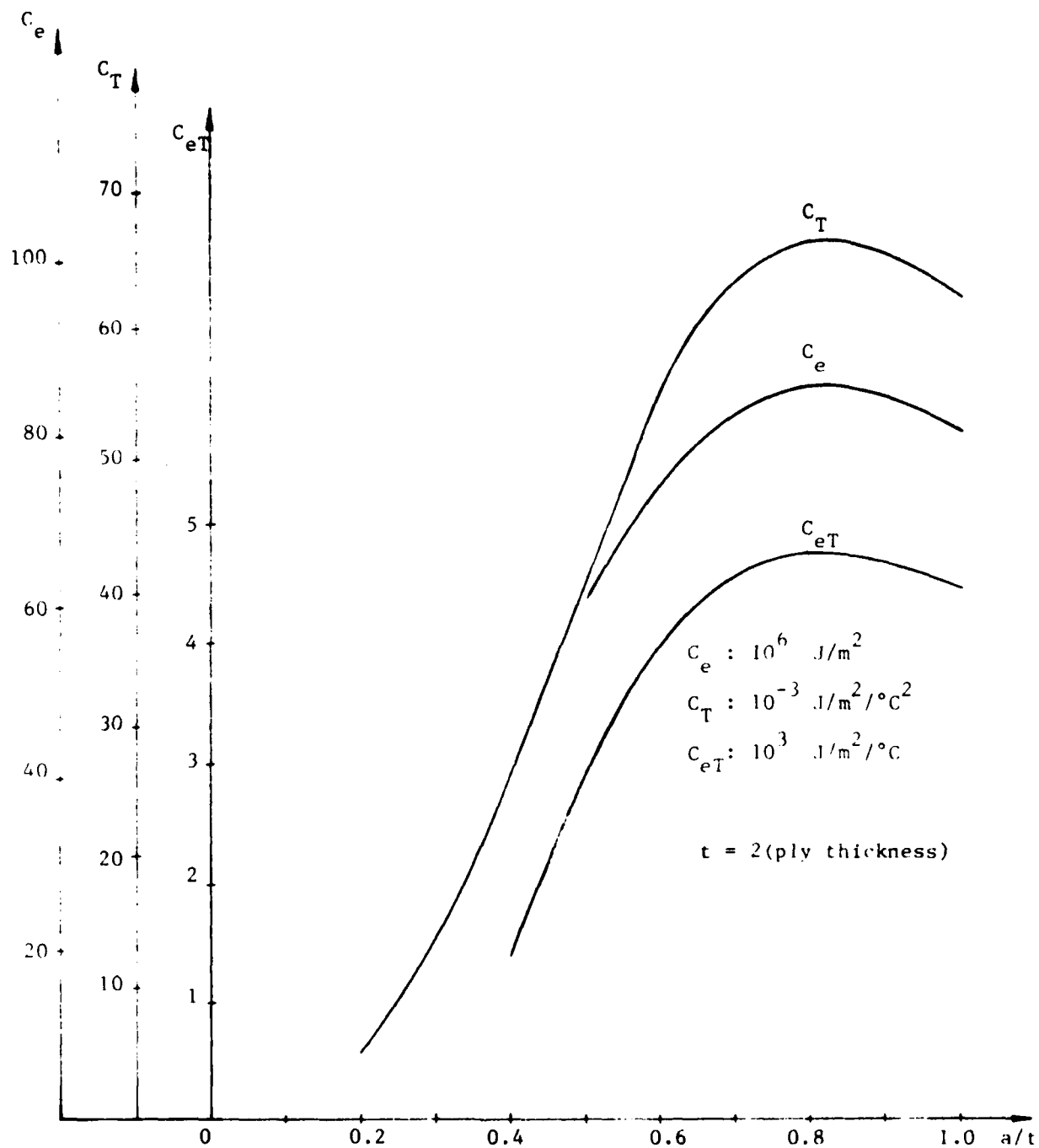Laminate under Uniaxial Tension and Uniform Thermal Loading.

Figure 56. Transverse Cracking Coefficient Functions for $[90_2/0_2/-45_2/45_2]_s$
Laminate under Uniaxial Tension and Uniform Thermal Loading.
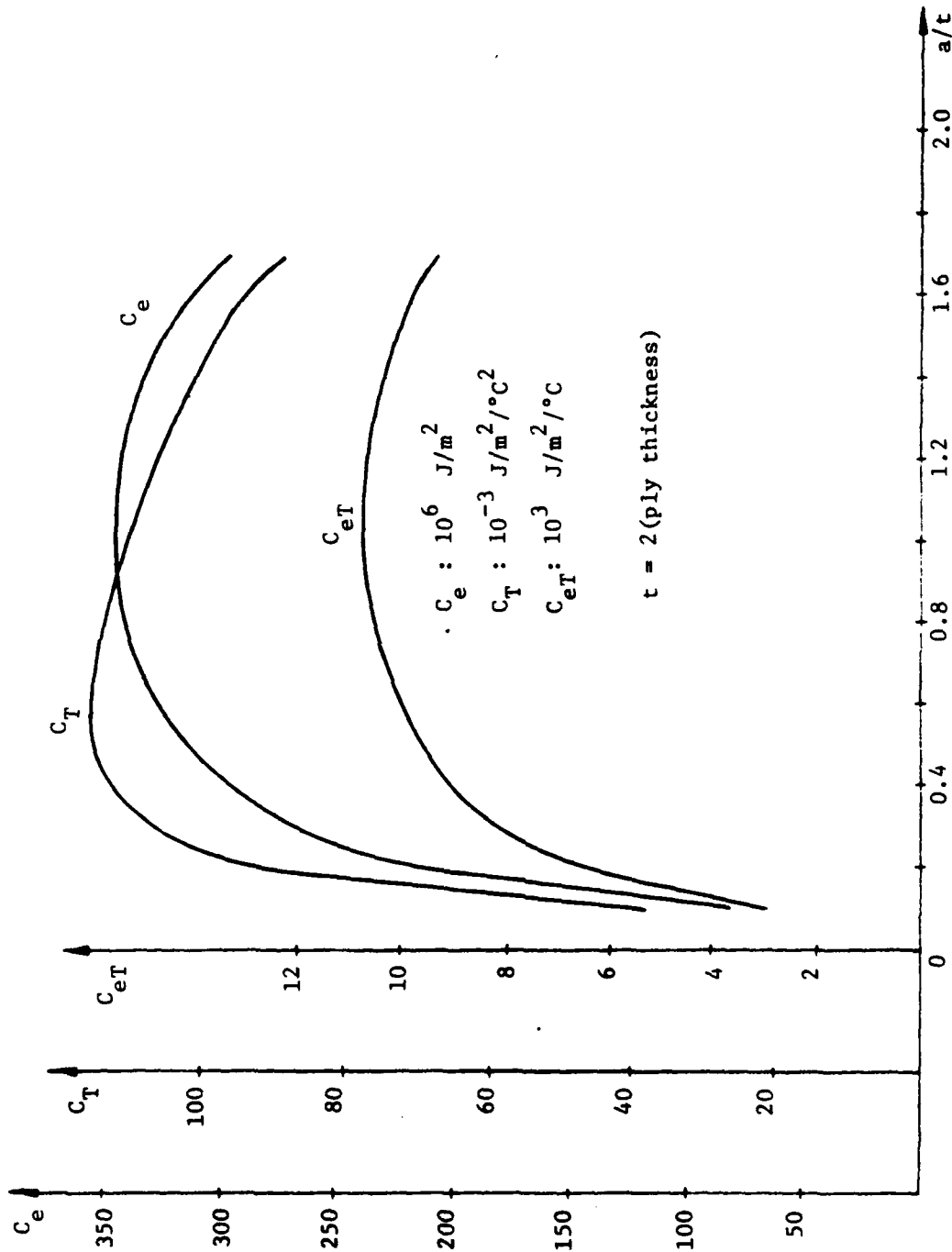
Figure 57. Off-Mid-plane Delamination (45/-45) Coefficient Functions for $[0_2/90_2/45_2/-45_2]_s$ Laminate under Uniaxial Compression and Uniform Thermal Loading.

143
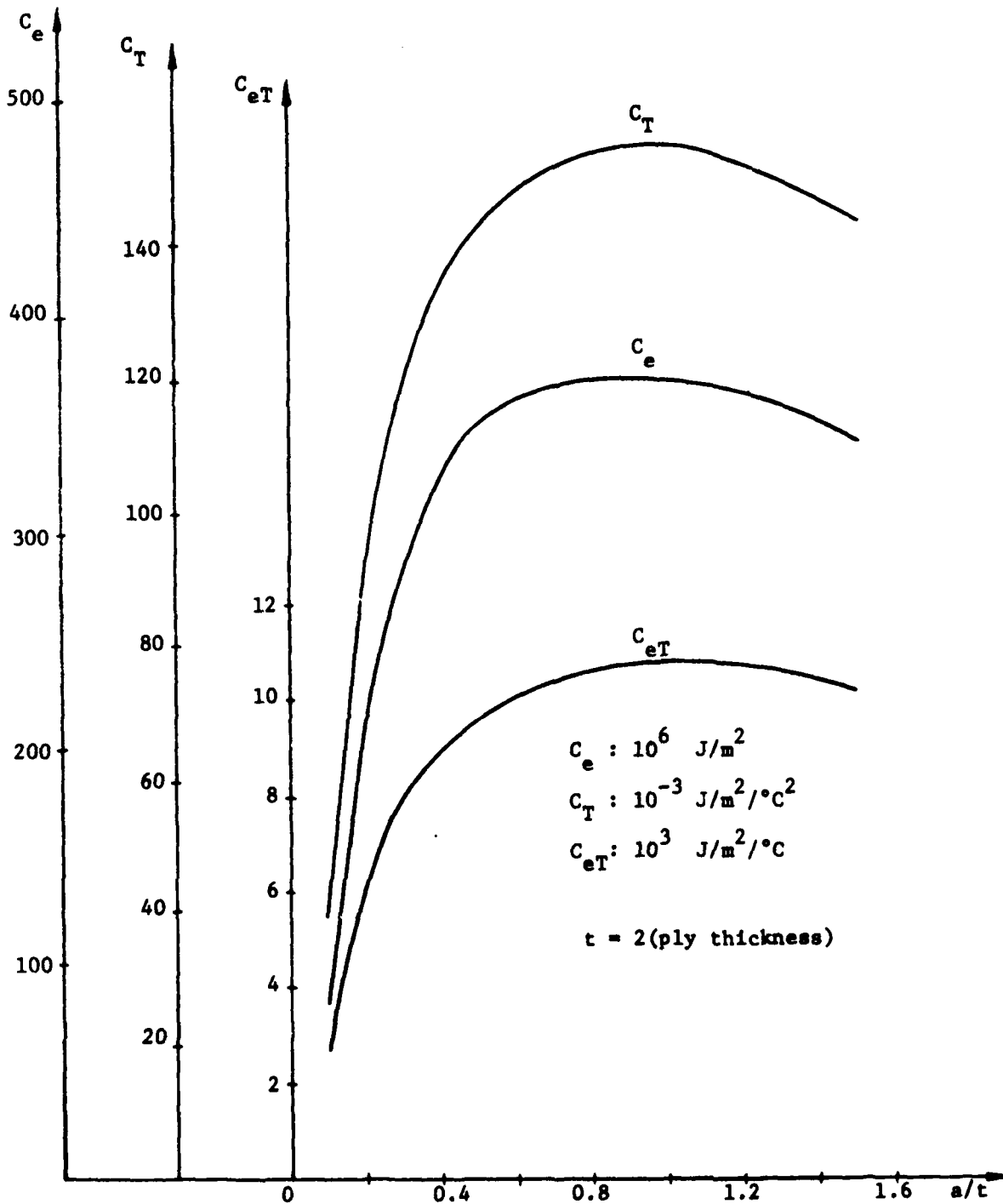
Figure 58. Off-Mid-plane Delamination (-45/45) Coefficient Functions
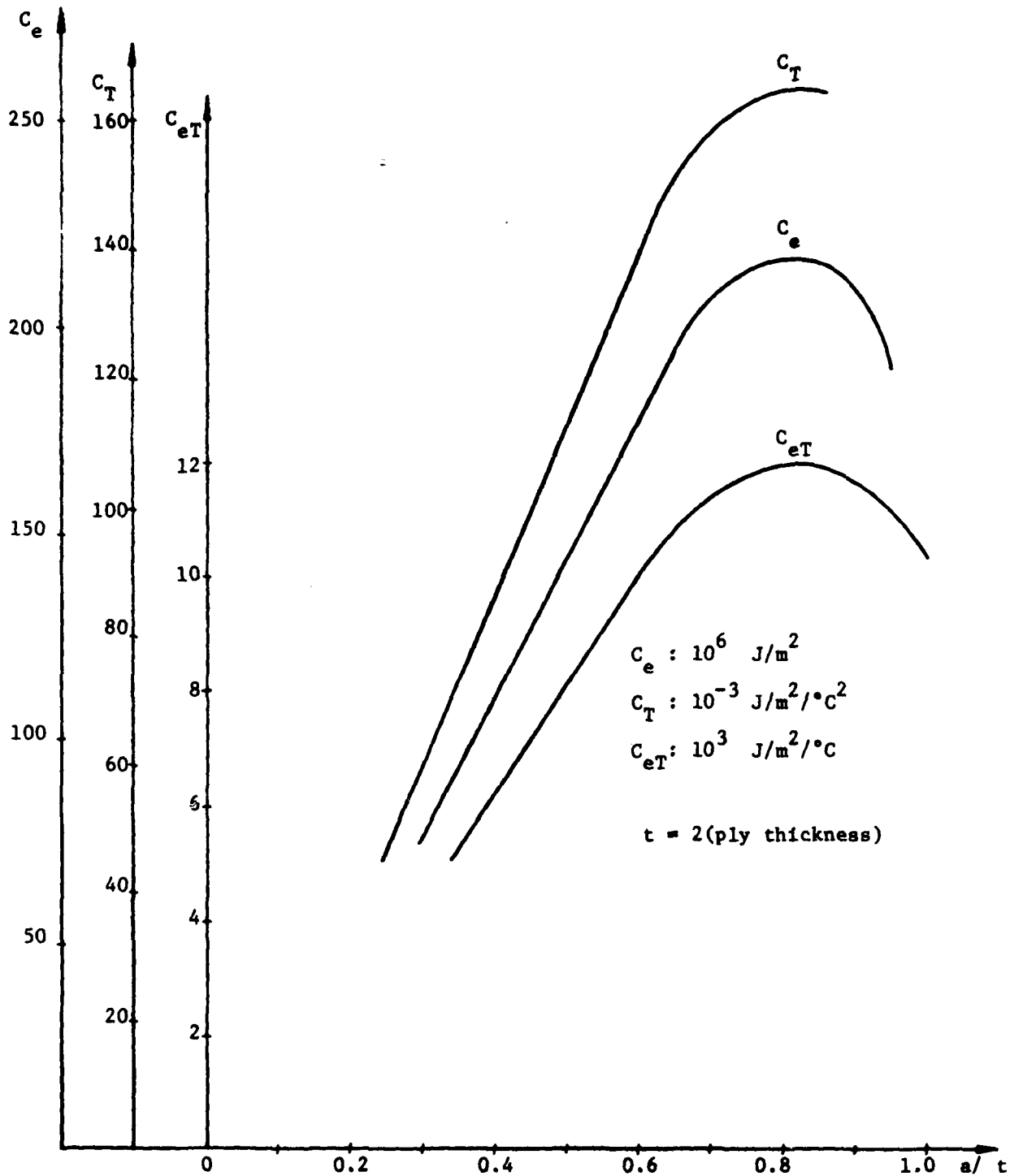for $[90_2/0_2/-45_2/45_2]_s$ Laminate under Uniaxial Compression
and Uniform Thermal Loading.

144
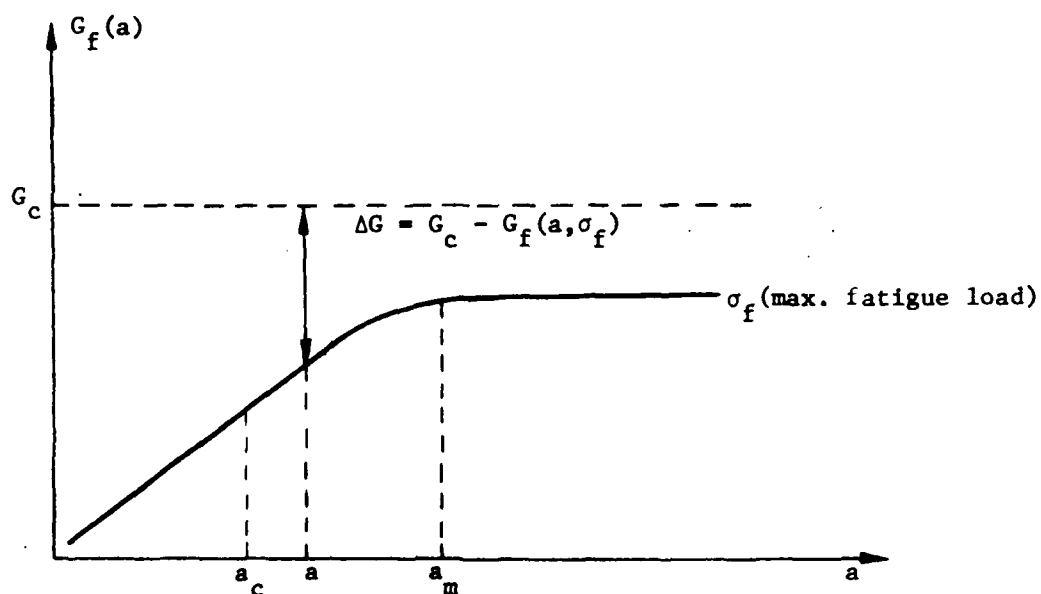
Figure 59. Schematics of the Strain Energy Release Rate Reserve,
for Laminate Undergoing Free Edge Delamination.
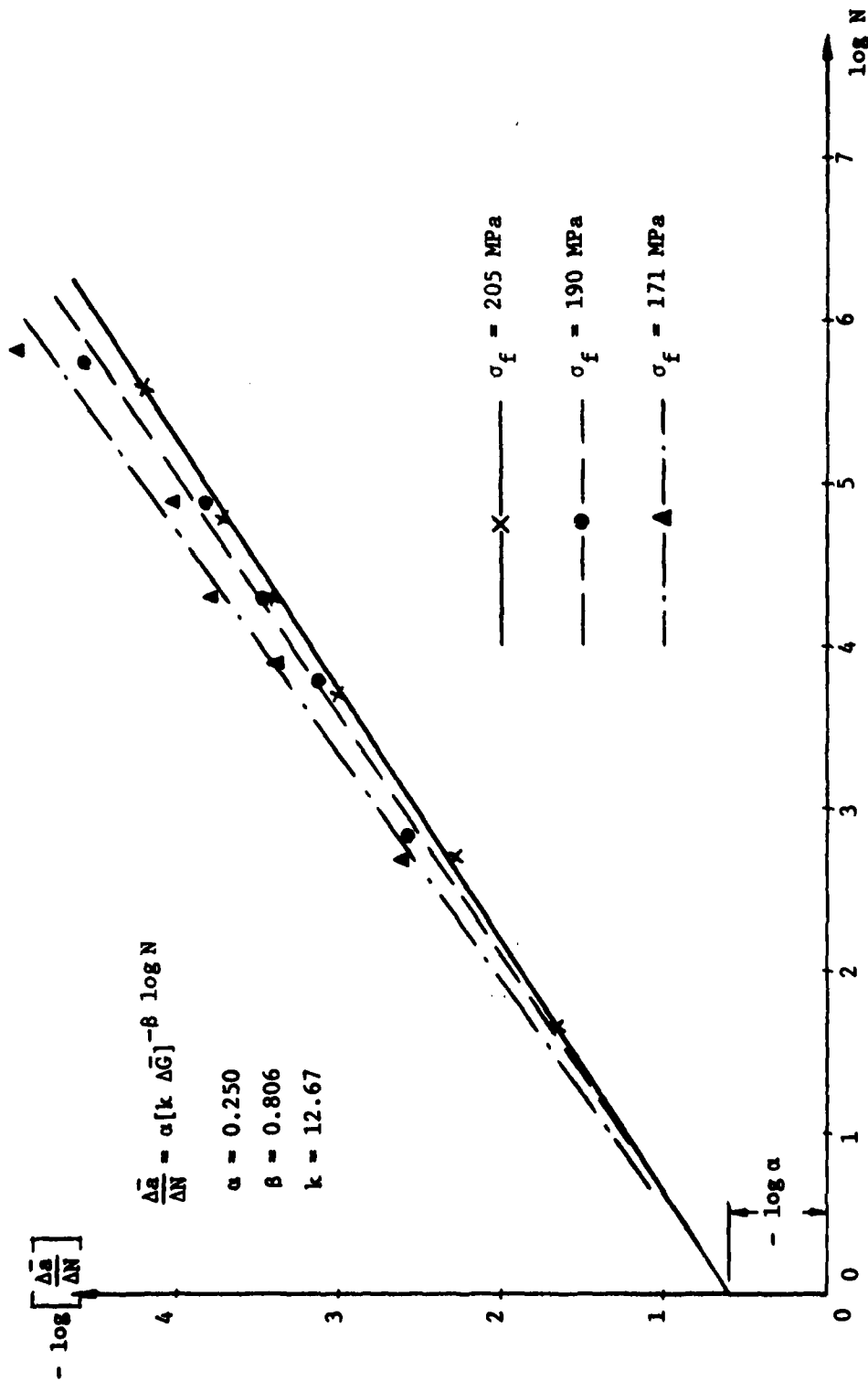
Figure 60. Data Reduction for α, β and k in the Fatigue Damage Growth Model for $[\pm 45/0/90_2]_s$ Laminates under Tension Fatigue.
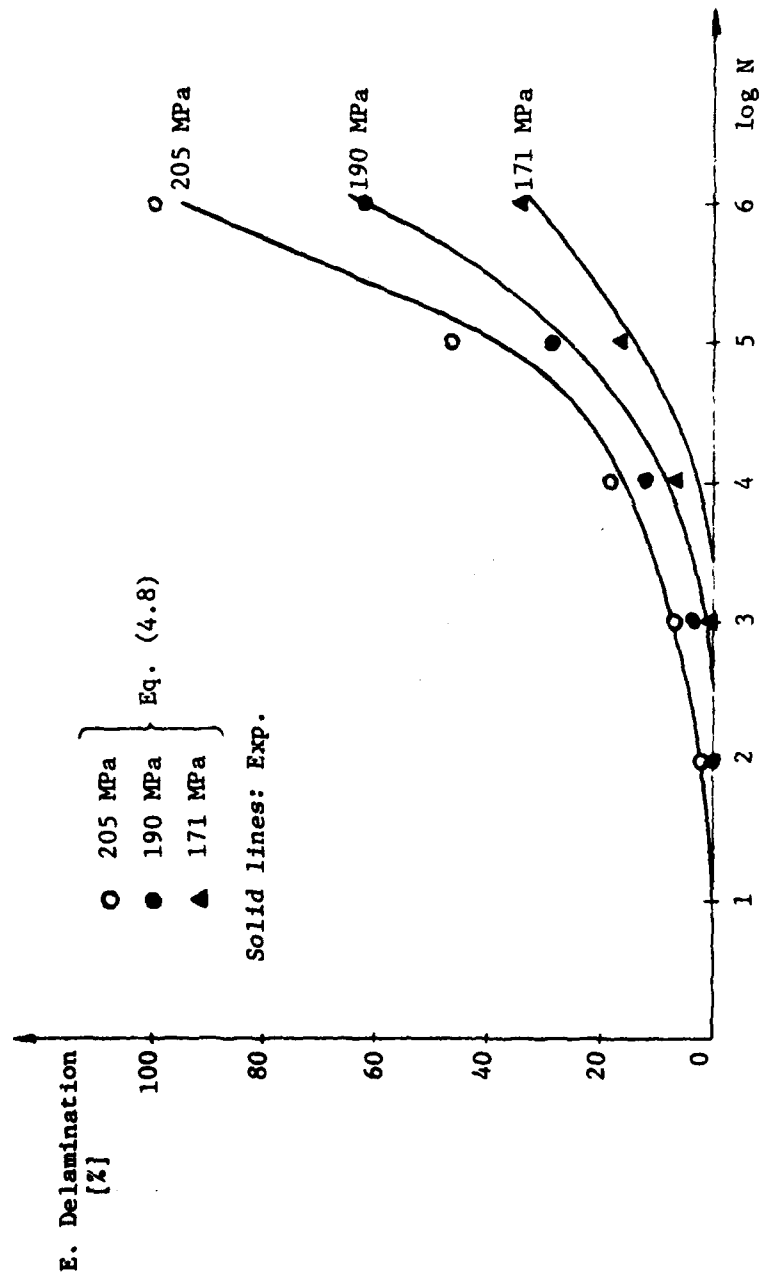
Figure 61. Comparison of the Edge Delamination Growth Model with Experiment for $[\pm45/0/90_2]_s$ Laminate under Tension Fatigue.
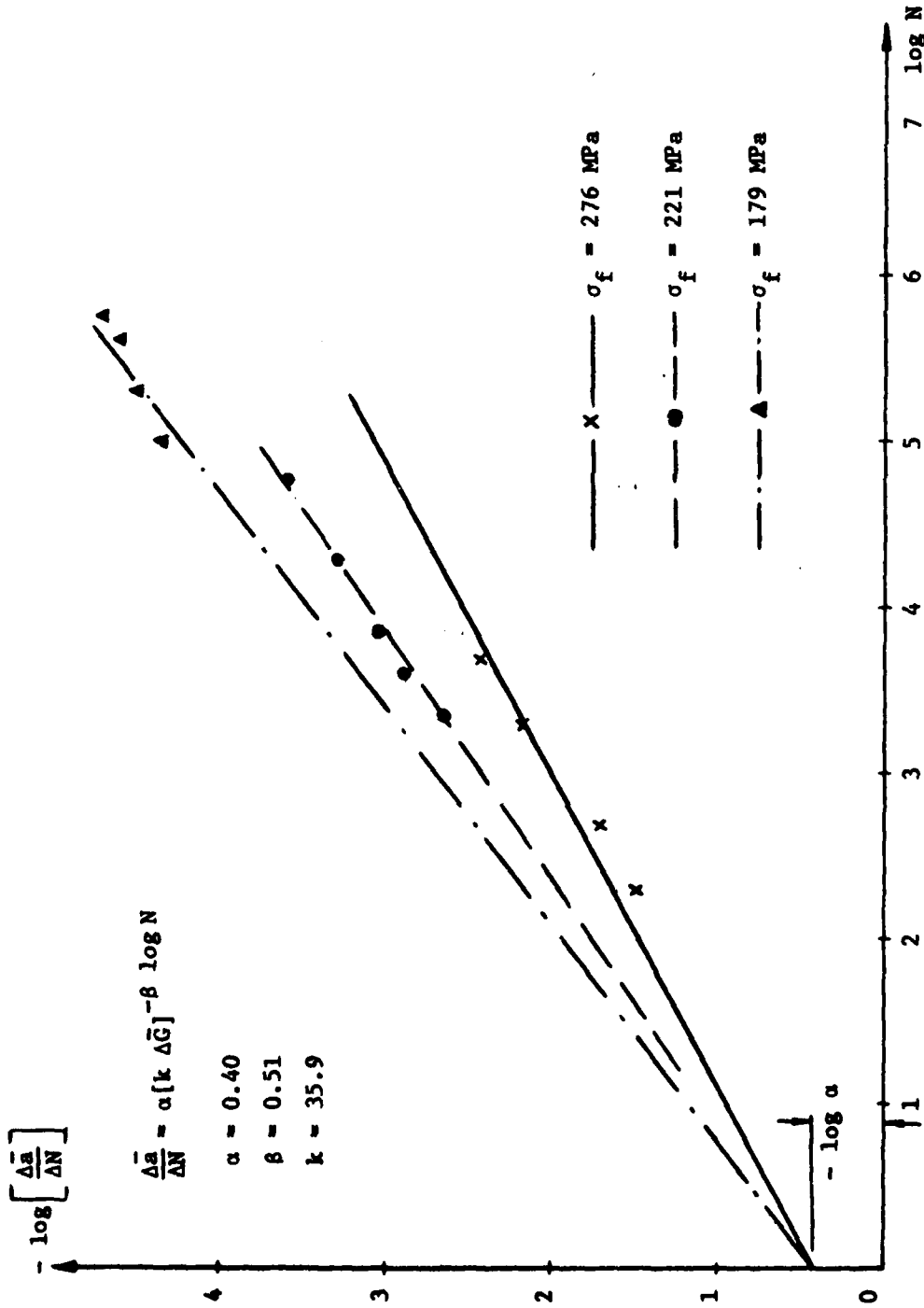
Figure 62. Data Reduction for α, β and k in the Fatigue Damage Growth Model for $[0_2/90_2/45_2/-45_2]_s$ Laminate under Compression Fatigue.

$$\frac{\Delta\bar{a}}{\Delta N} = \alpha[k\,\Delta\bar{G}]^{-\beta}\log N$$

$\alpha = 0.40$

$\beta = 0.51$

$k = 35.9$

$\sigma_f = 276$ MPa

$\sigma_f = 221$ MPa

$\sigma_f = 179$ MPa

$-\log\left[\dfrac{\Delta\bar{a}}{\Delta N}\right]$

$-\log\alpha$

log N
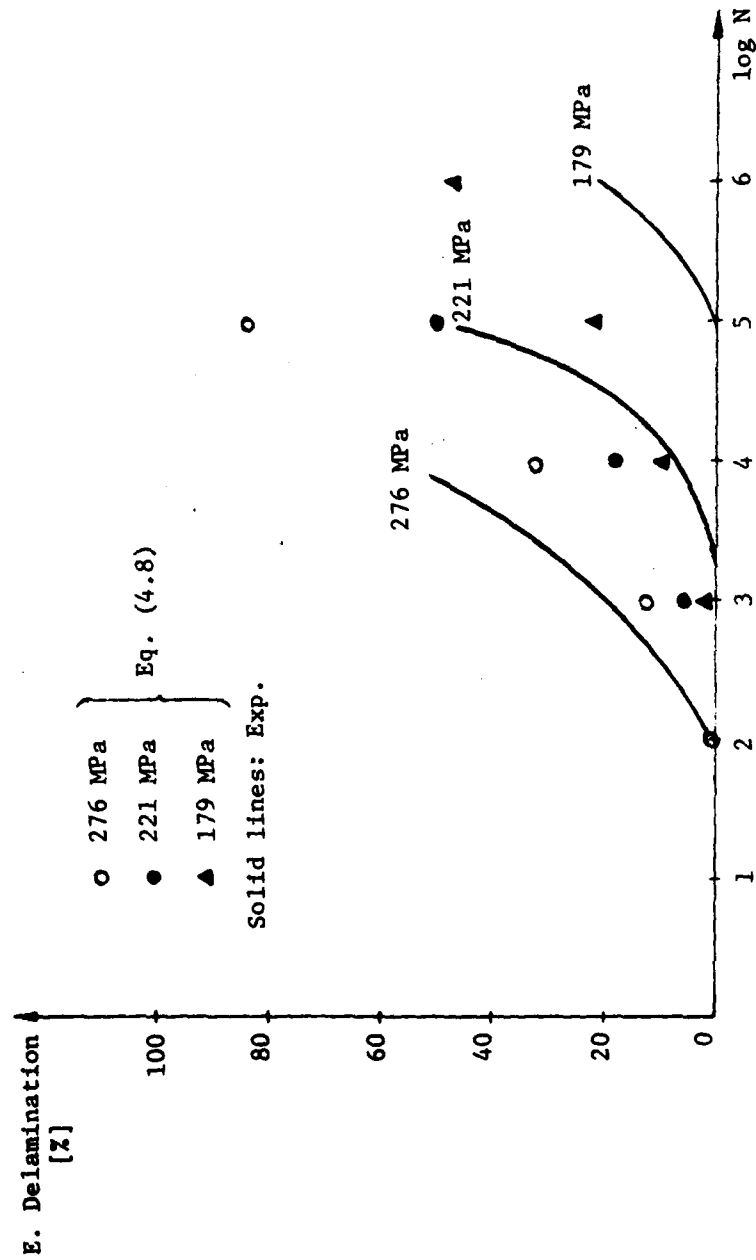
Figure 63. Comparison of the Edge Delamination Growth Model with Experiment for $[0_2/90_2/45_2/-45_2]_s$ Laminate under Compression Fatigue.

149
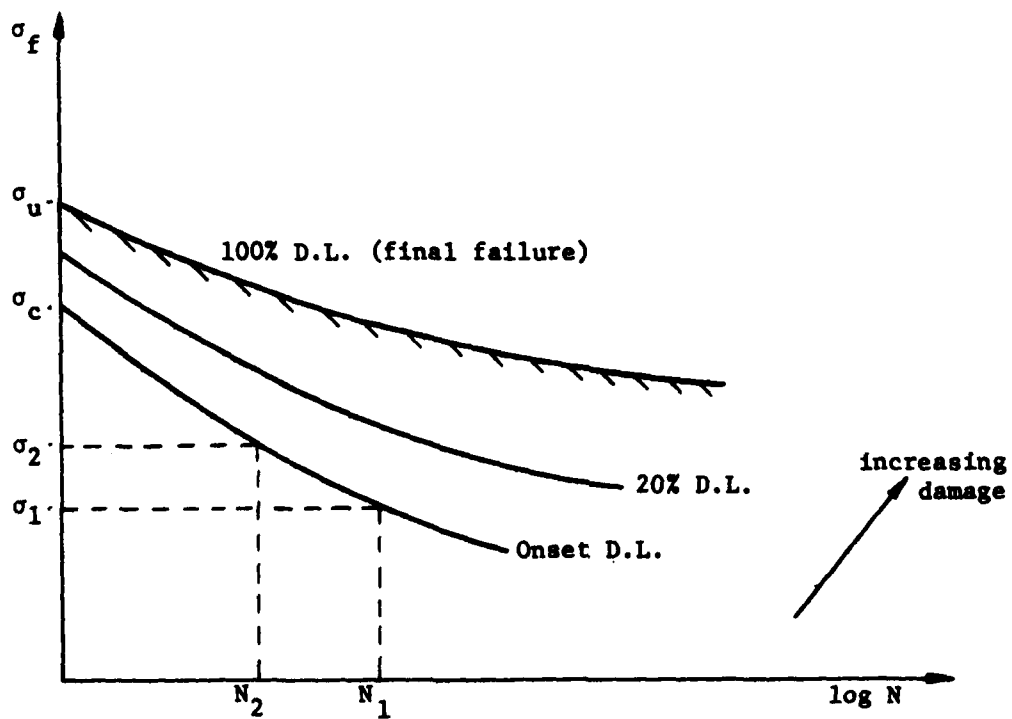
Figure 64. Schematics for the Concept of Constant Damage Curves
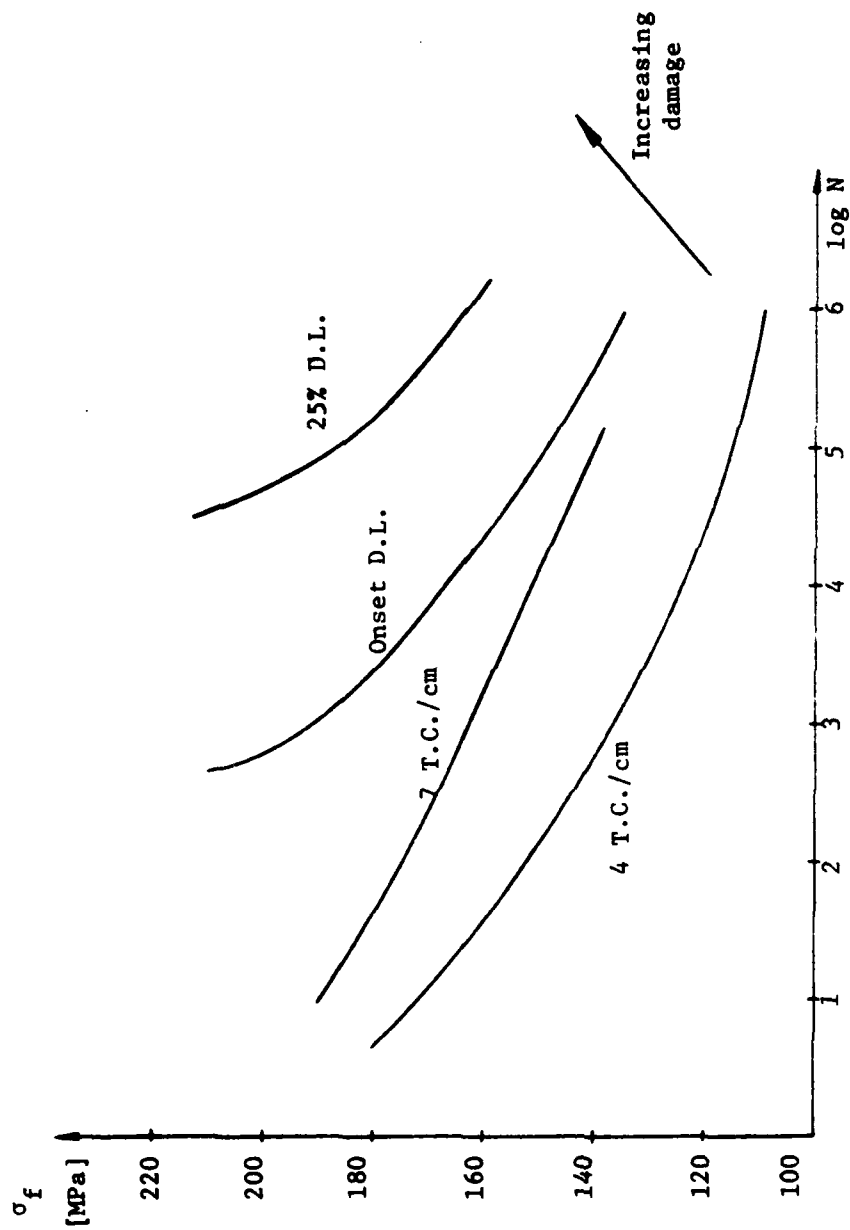
Figure 65. Constant Damage Curves Obtained from Tests on $[\pm45/0/90_2]_s$ Laminates under Tension Fatigue.

151
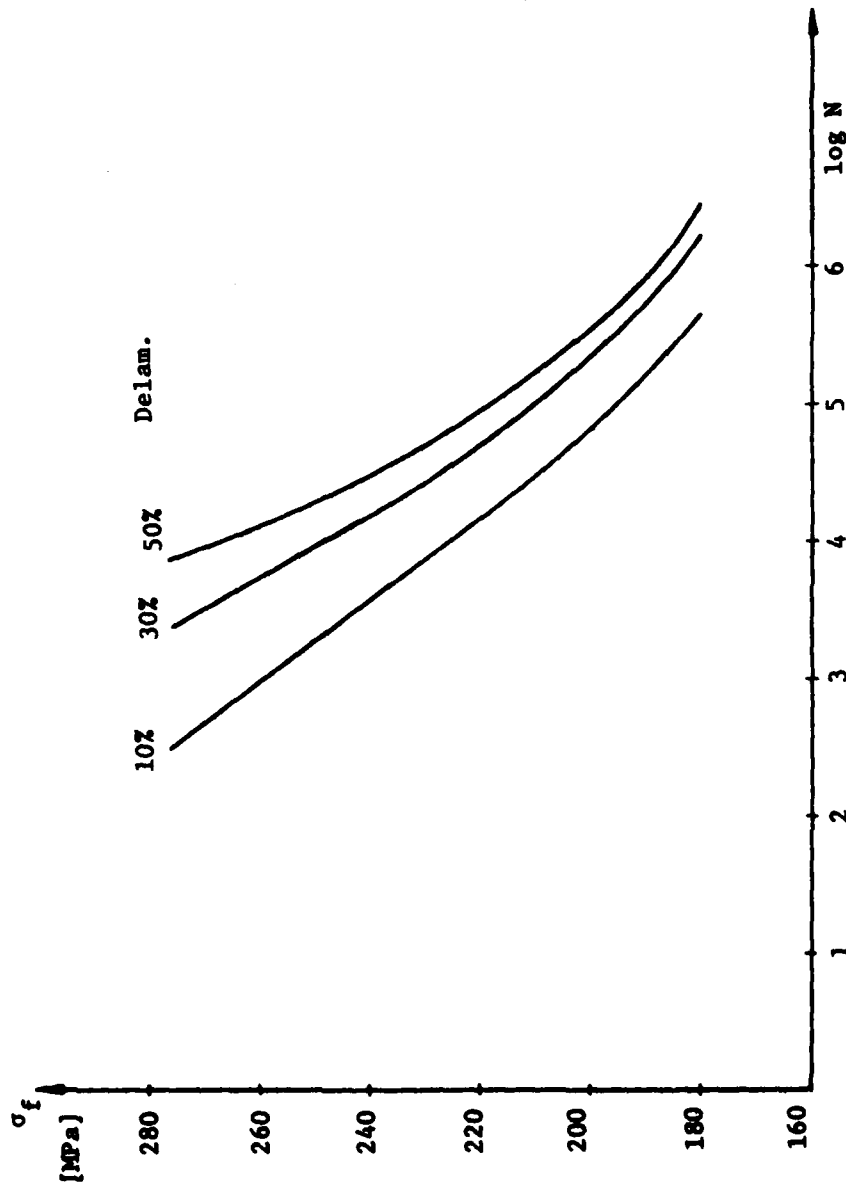
Figure 66. Constant Damage Curves Obtained from Tests on
$[0_2/90_2/45_2/-45_2]_s$ Laminates under Compression Fatigue.
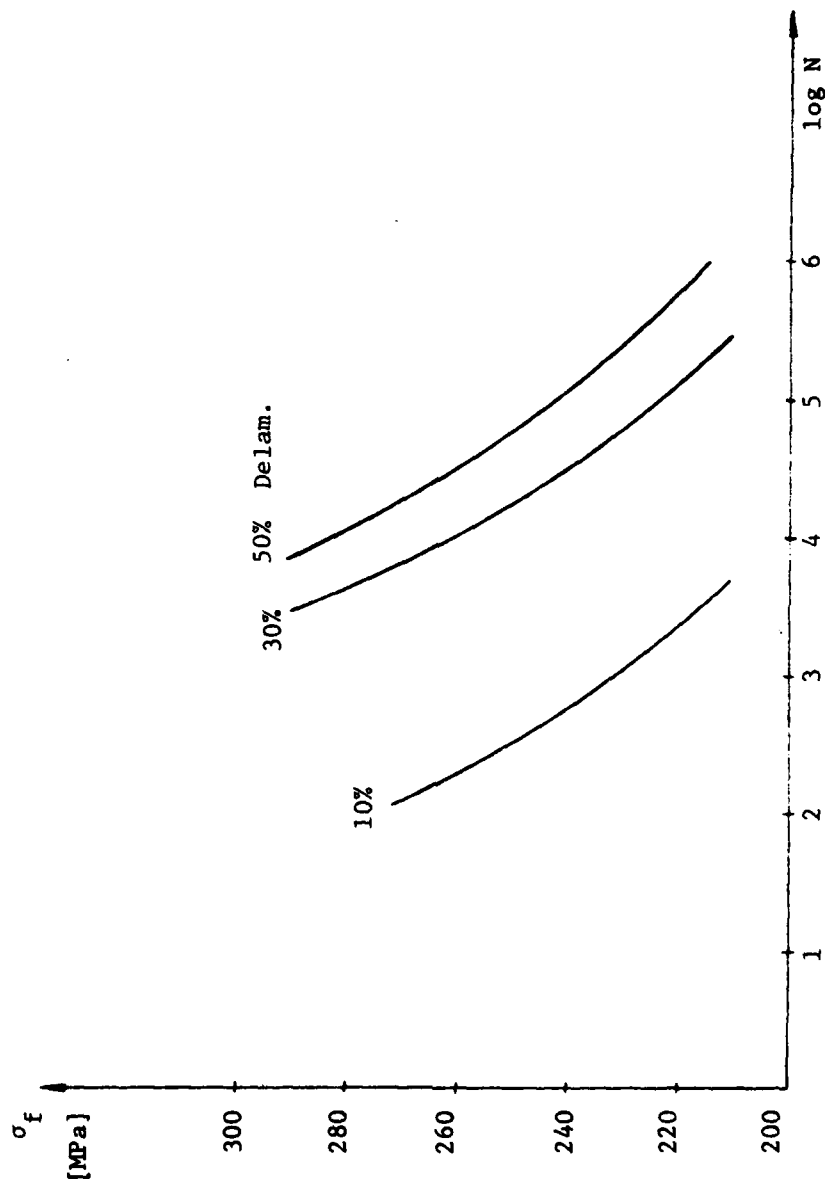
Figure 67. Constant Damage Curves Obtained from Tests on
[0/90/0/90/45/-45/45/-45]$_s$ -A Laminates under Compression Fatigue.
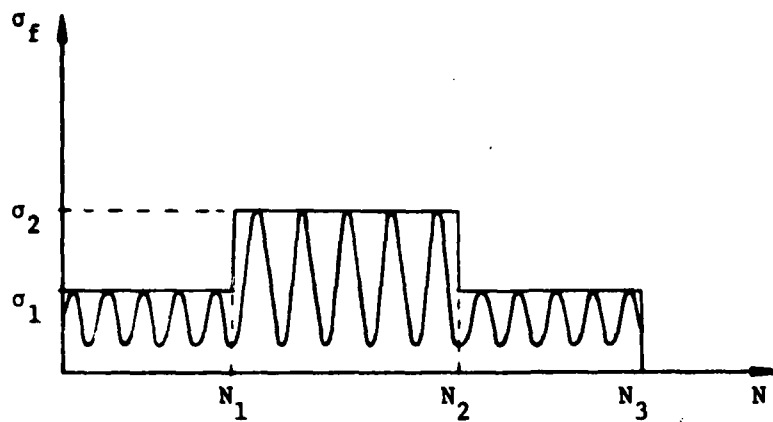
(a) Schematic of A Spectrum Loading History
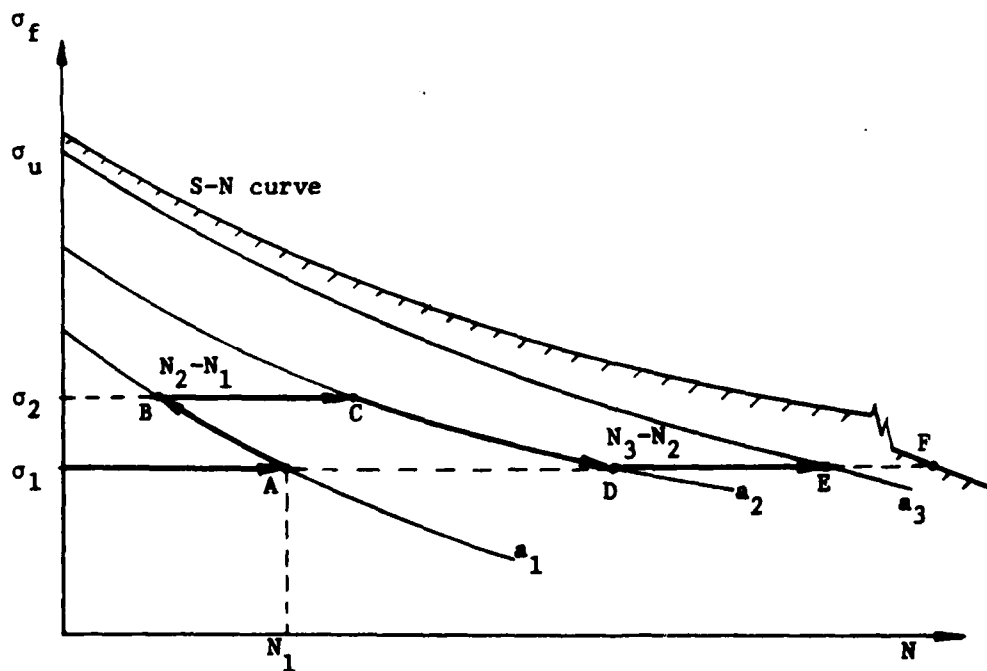
(b) Damage Growth Path in the Load-Life Plane

Figure 68. Cumulative Damage Based on the Concept of Constant Damage State.

154

Non-Government Agencies (continued)

No. of
Copies

University of Wyoming, Laramie, WY 82071 (Attn: Dr. D. Adams). 1
Villanova University, Villanova, PA 19085
(Attn: Dr. P. V. McLaughlin) 1
Virginia Polytechnic Institute, Blacksburg, VA 24061
(Attn: Dr. K. Reifsnider). 1
Vought Corporation, Dallas, TX 75265
(Attn: Mr. O. E. Dhonau/2-53442) 1
(Attn: Dr. J. Renton). 1

Non-Government Agencies (continued)

	No. of Copies
McDonnell Douglas Corporation, St. Louis, MO 63166	
(Attn: Mr. J. Schier).	1
(Attn: Mr. C. Stenberg).	1
(Attn: Mr. R. Garrett)	1
McDonnell Douglas Corporation, Long Beach, CA 90846	
(Attn: G. Lehman).	1
(Attn: D. Smillie)	1
Minnesota Mining and Manufacturing Company, St. Paul, MN 55104	
(Attn: Mr. W. Davis)	1
Northrop Aircraft Corporation, One Northrop Avenue, Hawthorne,	
CA 90250 (Attn: Mr. L. Jeans).	1
(Attn: Mr. D. Stansbarger)	1
(Attn: Mr. R. C. Isemann).	1
(Attn: Mr. R. M. Verette).	1
(Attn: Mr. B. Butler).	1
Owens Corning Fiberglass, Granville, OH 43023	
(Attn: Mr. D. Mettes).	1
Prototype Development Associates, Inc., 1560 Brookhollow Drive,	
Santa Ana, CA 92705 (Attn: E. L. Stanton).	1
Rockwell International, Columbus, OH 43216	
(Attn: Mr. F. Kaufman)	1
(Attn: Mr. M. Schweiger)	1
Rockwell International, Los Angeles, CA 90009	
(Attn: Dr. Lackman).	1
Rockwell International, Tulsa, OK 74151	
(Attn: Mr. E. Sanders)	1
(Attn: Mr. J. H. Powell)	1
Rohr Corporation, Riverside, CA 92503	
(Attn: Dr. F. Riel).	1
(Attn: Mr. R. Elkin)	1
School of Engineering and Applied Science, Materials Research Laboratory, Washington University, Campus Box 1087, St. Louis, MO 63130 (Attn: T. Hahn).	1
Sikorsky Aircraft, Stratford, CT 06622	
(Attn: Mr. J. Ray)	1
Teledyne Ryan Aeronautical Company, San Diego, CA 92138	
(Attn: Mr. R. Long).	1
Union Carbide Corporation, Cleveland, OH 44101	
(Attn: Dr. H. F. Volk)	1
University of Dayton Research Institute, 300 College Park Ave., Dayton, OH 45469 (Attn: Dr. J. Gallagher).	1
University of Delaware, Mechanics & Aerospace Eng. Dept., Evans Hall, Newark, DE 19711 (Attn: Dr. R. B. Pipes)	1
University of Oklahoma, Norman, OK 93069	
(Attn: Dr. C. W. Bert, School of AMNE)	1

Non-Government Agencies (continued)

<div align="right">
No. of
<u>Copies</u>
</div>

Effects Technology, Inc., 5383 Hollister Avenue, P. O.
Box 30400, Santa Barbara, CA 93111 (Attn: Robert Globus). . . .   1
E. I. DuPont Company, Wilmington, DE 19898
(Attn: Dr. J. Pigoiacampi).   1
Fairchild Republic Company, Farmingdale, L.I., NY 11735
(Attn: Mr. Frank Costa)   1
Georgia Institute of Technology, Atlanta, GA
(Attn: Prof. W. H. Horton).   1
General Dynamics/Convair, San Diego, CA 92138
(Attn: Mr. D. R. Dunbar).   1
(Attn: Mr. W. G. Scheck).   1
General Dynamics, Fort Worth, TX 76101
(Attn: Mr. J. A. Fant).   1
(Attn: Mr. E. Petruska)   1
(Attn: Dr. D. Wilkins (Composite Structures Eng. Dept.)   1
General Electric Company, Phila., PA 19101
(Attn: Dr. C. Zweben)   1
(Attn: Mr. A. Garber)   1
Great Lakes Carbon Corporation, NY, New York 10017
(Attn: Mr. W. R. Benn, Mgr., Market Development).   1
Grumman Aerospace Corporation, South Oyster Bay Rd., Bethpage,
Long Island, NY 11714
(Attn: Mr. R. Hadcock).   1
(Attn: Mr. S. Dastin)   1
Hercules Aerospace Div., P. O. Box 210, Cumberland, MD 21502
(Attn: Mr. D. Hug).   1
H. I. Thompson Fiber Glass Company, Gardena, CA 90240
(Attn: Mr. N. Myers).   1
ITT Research Institute, Chicago, IL 60616
(Attn: Mr. K. Hofar).   1
J. P. Stevens & Co., Inc., New York, NY 10036
(Attn: Mr. H. I. Shulock)   1
Kaman Aircraft Corporation, Bloomfield, CT 06002
(Attn: Technical Library)   1
Lehigh University, Bethlehem, PA 18015
(Attn: Dr. G. C. Sih)   1
Lockheed-California Co., Burbank, CA 91520
(Attn: Mr. E. K. Walker).   1
(Attn: Mr. Vaughn).   1
(Attn: Mr. A. James).   1
Lockheed-California Co., Rye Canyon Research Lab,
Burbank, CA 91520 (Attn: Mr. Don E. Pettit)   1
Lockheed-Georgia Company, Marietta, GA 30063
(Attn: Technical Information Dept., Dept. 72-34, Zone 26) . . .   1
Martin Company, Baltimore, MD 21220
(Attn: Mr. J. E. Pawken).   1
Materials Sciences Corporation, Spring House, PA 19477   1

Government Activities (continued)

	No. of Copies
NOL, White Oak, MD 20910 (Attn: Mr. F. R. Barnet)	1
NRL, Washington, D.C. 20375 (Attn: Dr. I. Wolock)	1
ONR, Washington, D.C. 20362 (Attn: Dr. N. Perrone)	1
PLASTEC, Picatinny Arsenal, Dover, NJ 07801 (Attn: Mr. H. Pebly)	1
(Attn: Librarian, Bldg. 176, SARPA-FR-M-D)	1
U. S. Army Materials Research Center (DRXMR-TM), Watertown, MA 02172 (Attn: Dr. E. Lenoe)	1
(Attn: Mr. D. Oplinger)	1
U. S. Army Research Office, Durham, NC 27701	1
U. S. Army R&T Lab (AVRADCOM), Ames Research Center, Moffett Field, CA 94035 (Attn: Mr. F. Immen, DAVDL-AS-M.S. 207-5, Dr. R. Foye)	2

Non-Government Agencies

Avco, Aero Structures Division, Nashville, TN 37210	1
Battelle Columbus Laboratories, Metals and Ceramics Information Center, 505 King Avenue, Columbus, OH 43201	1
Bell Aerospace Company, Buffalo, NY 14240 (Attn: Zone I-85, Mr. F. M. Anthony)	1
Bell Helicopter Company, Fort Worth, TX 76101 (Attn: Mr. G. Reis Alsmiller, Jr.)	1
Bendix Products Aerospace Division, South Bend, IN 46619 (Attn: Mr. R. V. Cervelli)	1
Boeing Company, P. O. Box 3707, Seattle, WA 98124 (Attn: Mr. R. E. Horton, MS 9K-23)	1
(Attn: Dr. R. June)	1
Boeing Company, Vertol Division, P. O. Box 16858, Philadelphia, PA 19142 (Attn: Mr. R. L. Pinckney)	1
(Attn: Mr. D. Hoffstedt)	1
(Attn: Mr. L. Marchinski)	1
Boeing Company, Wichita, KS 67210 (Attn: R. D. Hoaglanb - M. S. -K32-95)	1
Cabot Corporation, Billerica Research Center, Billerica, MA 01821	1
Compositek Engineering Corporation, 6925-1 Aragon Circle, Buena Park, CA 90620 (Attn: J. V. Noyes)	1
Drexel University, Phila., PA 19104 (Attn: Dr. P. C. Chou)	1
(Attn: Dr. A. S. D. Wang)	1

DATE
ILME